SOME NEW STUDIES IN THE TECHNIQUES OF ANALYTICAL ATOMIC SPECTROSCOPY

B.L. Sharp, B.Sc.

Imperial College, London

A THESIS SUBMITTED FOR THE DEGREE OF DOCTOR OF PHILOSOPHY

ABSTRACT

A microwave excited, atmospheric pressure, argon plasma was investigated as a source for emission spectrometry. The electron temperature of the plasma was measured and the results employed to demonstrate that the bulk of the free electrons were in local thermodynamic equilibrium with the excited states of the argon carrier gas. The measured equilibrium temperature was 5680 K which was sufficient to enable the plasma to excite atomic states over eleven electron volts above the ground state.

A plasma emission system was constructed, sampling being achieved by use of a platinum loop atomiser. The device proved extremely sensitive for a range of elements yielding detection limits down to $2.0.10^{-13}$ g for Cd. The analytical precision was acceptable and preliminary studies indicated that interferences were not serious.

Radiation signals obtained from the emission system were transient in nature and required integration for optimum precision of measurement. Initially capacitative integration was employed but later this was replaced by a photon counting system. The results obtained with photon counting were excellent and therefore a general investigation of the technique was undertaken. Photon counter design was studied, a new system constructed and theoretical work carried out to determine optimum system parameters.

The application of the technique to atomic emission, atomic fluorescence and atomic absorption was investigated for both transient and continuous radiation signals. Experimental results suggested that in certain conditions long period integration might yield improved limits of detection. Theoretical signal to noise ratio expressions were therefore developed in order to explain these results and to define more clearly how the various noise components affect the precision of measurement.

ACKNOWLEDGEMENTS

The author is indebted to the following persons for their valuable assistance. To Dr. R.M. Dagnall for his supervision, help and guidance at all times throughout this work; to all members of the Analytical Group for useful discussions and to Mr. A. Cummings for his help with determining plasma temperature by the relative line method.

Thanks are also due to Mr. D. Alger for his advice and assistance and to the S.R.C. who provided a maintenance grant and funds for equipment.

Finally, special thanks are due to my wife, Chris, for her encouragement during the last three years, and for typing the manuscript.

CONTENTS

		Page
Abstract		2
Acknowledgements		3
Chapter I		9
1.1.	HISTORY OF SPECTROSCOPY.	10
1.2.	STATEMENT OF INTENT.	12
1.3.	THE PROPERTIES REQUIRED OF AN EXCITATION SOURCE IN ATOMIC EMISSION SPECTROMETRY.	13
1.4.	ELECTRODELESS PLASMAS AS SOURCES OF SPECTRAL EXCITATION.	17
1.5.	THE ANALYTICAL CURVE IN ATOMIC EMISSION SPECTROMETRY.	18
1.6.	SOURCE AND ATOMISER REQUIREMENTS IN AA AND AF.	20
1.6.1.	Atomiser Requirements in AA and AF.	20
1.6.2.	Source Requirements in AA.	21
1.6.3.	Source Requirements in AF.	22
1.7.	THE ANALYTICAL CURVE IN AA.	23
1.7.1.	Line Source.	24
1.7.2.	Continuum Source.	24
1.8.	THE ANALYTICAL CURVE IN AF.	25
1.8.1.	Line Source.	25
1.8.2.	Continuum Source.	25
Chapter II		26
2.1.	INTRODUCTION.	27
2.2.	DETERMINATION OF THE ELECTRON TEMPERATURE BY THE RELATIVE INTENSITY OF SPECTRAL LINES METHOD.	29
2.2.1.	Theory.	29
2.2.2.	The Plasma.	33

		Page
2.2.3.	Optical Considerations.	35
2.2.4.	The Photographic Recording Method.	37
2.3.	DETERMINATION OF THE ELECTRON TEMPERATURE BY THE RELATIVE LINE-CONTINUUM METHOD.	47
2.3.1.	Theory.	47
2.3.2.	Experimental.	51
2.3.3.	Results.	52
2.4.	DETERMINATION OF THE ELECTRON TEMPERATURE BY THE DOUBLE PROBE METHOD.	55
2.4.1.	Theory of electron temperature measurement.	58
2.5.	DETERMINATION OF THE NEUTRAL ARGON TEMPERATURE.	62
2.6.	THE EFFECT OF ADDING NITROGEN TO THE PLASMA.	66
2.7.	EQUILIBRIUM OF THE PLASMA.	69
2.7.1.	Theory.	69
2.7.2.	Experimental Evidence.	70
2.8.	PLASMA MECHANISM.	73
2.8.1.	The Ionisation Recombination Equilibrium.	73
2.8.2.	The Ionisation Process.	74
2.8.3.	Penning Ionisation.	79
2.8.4.	Ionisation of Impurities.	80
2.8.5.	The Excitation Mechanism.	80
2.8.6.	The Excitation of Foreign Species.	81
Chapter III		83
3.1.	INTRODUCTION.	84
3.2.	THE EXPERIMENTAL SYSTEM.	87
3.2.1.	The d.c. Amplifier/Integrator.	87
3.2.2.	The Plasma Cell.	91
3.2.3.	The Plasma.	92

		Page
3.2.4.	The Sampling Loops.	93
3.3.	OPTIMISATION OF THE OPERATING CONDITIONS.	94
3.3.1.	Argon Flow Rate.	94
3.3.2.	Microwave Power.	96
3.3.3.	The Occurrence of Intensity Antinodes in the Plasma	98
3.4.	THE ANALYTICAL WORKING CURVE FOR CADMIUM.	98
3.5.	APPLICATION TO OTHER ELEMENTS.	100
3.6.	INTERFERENCES.	101
3.6.1.	Special Interference.	101
3.6.2.	Chemical Interference.	102
3.7.	OBSERVATIONS ON THE PLATINUM LOOP SAMPLING DEVICE.	103
3.7.1.	The Occurrence of Multiple Vapourisation Peaks.	103
3.7.2.	Signal Enhancement by Analyte Adsorption on the Platinum Surface.	108
3.8.	CONCLUSIONS.	109
Chapter IV		114
4.1.	INTRODUCTION.	115
4.2.	THE INTEGRAL TECHNIQUE OF SIGNAL MEASUREMENT.	116
4.3.	THE PRINCIPLES OF PHOTON COUNTING.	118
4.3.1.	The Photomultiplier Tube.	118
4.3.2.	Photomultiplier Dark Current.	122
4.3.3.	Pulse Pile-up in Photon Counting.	124
4.4.	A PRACTICAL PHOTON COUNTING SYSTEM.	129
4.4.1.	Design Considerations.	129
4.4.2.	Experimental Equipment.	134
4.4.3.	Operation and Evaluation of System.	135
4.5.	ANALYTICAL RESULTS OBTAINED WITH THE PHOTON COUNTING SYSTEM.	139

		Page
4.5.1.	Results with the Microwave Plasma System.	140
4.5.2.	Results with a Non-flame Atomic Fluorescence System.	141
4.5.3.	Results with a Non-flame Atomic Absorption System.	145
4.5.4.	Results with a Cool Flame Atomic Fluorescence System.	146
4.5.5.	Results with a Cool Flame Atomic Emission System.	147
4.5.6.	Summary of Results.	148
4.6.	AN IMPROVED AND SIMPLIFIED PHOTON COUNTER.	149
4.6.1.	Equipment and Performance.	149
4.6.2.	The effect of Cooling the Photomultiplier.	151
4.6.3.	Application to Atomic Fluorescence Spectrometry.	153
4.6.4.	Application to Atomic Absorption Spectrometry.	156
4.7.	A THEORETICAL ANALYSIS OF PHOTO-ELECTRON PULSE DISTORTION BY THE PHOTOMULTIPLIER ANODE NETWORK.	158
4.8.	CONCLUSIONS.	165
Chapter V		167
5.1.	INTRODUCTION.	168
5.2.	SOURCES OF NOISE IN PHOTON COUNTING.	169
5.2.1.	Poisson Noise.	169
5.2.2.	Johnston Noise.	170
5.2.3.	Flicker Noise.	171
5.2.4.	Read-out Noise.	173
5.2.5.	Total Noise in Photon Counting.	173
5.3.	THE COMPARISON OF NOISE IN PHOTON COUNTING AND D.C. SYSTEMS.	173
5.4.	SIGNAL TO NOISE RATIO EXPRESSIONS IN PHOTON COUNTING.	177

		Page
5.4.1.	The Time-related Signal to Noise Ratio in Atomic Fluorescence and Atomic Emission Spectrometry.	179
5.4.2.	The Signal to Noise Ratio in Atomic Absorption Spectrometry	186
5.4.3.	The Signal to Noise Ratio for Transient Signals.	189
5.5.	CONCLUSIONS.	191
APPENDIX I.		193
APPENDIX II.		195
REFERENCES.		199

CHAPTER I

INTRODUCTION

1.1. HISTORY OF SPECTROSCOPY.

The study of spectroscopy was founded in 1663, with the discovery by Isaac Newton that white light could be resolved by a prism into a spectrum of colours. Over one hundred years elapsed before the next significant advance was made, when Joseph Fraunhofer observed dark lines in the spectrum of the Sun and measured their wavelength with the first transmission grating. The origins of analytical spectroscopy can be traced to the work of Bunsen and Kirchhoff, who in 1860 used the first pre-mixed air-coal gas flame to observe the atomic emission of five new elements Cs, Rb, Tl, In and Ga (1,2).

Atomic emission (AE) spectroscopy received further attention in the early part of this century mainly in connection with the study of arcs and sparks. Advances in flame emission spectroscopy were few until 1928 when Lundergardh published a series of papers (3) describing the use of the air-acetylene flame and a pneumatic nebuliser for introducing aqueous samples. The first instruments which were designed for the determination of the alkali metals became available in the mid nineteen forties and since then the technique has been extended to cover most of the elements in the periodic table.

The phenomenon of atomic absorption (AA) was first observed by Fraunhofer, but it was not until 1860 that Kirchhoff postulated that the absorption lines resulted from the presence of certain elements in the solar atmosphere. The theory of AA was developed during the first part of this century; much of this work can be found in the text of "Resonance Radiation and Excited Atoms" by Mitchell and Zemansky (4). It was not until 1953 that Walsh (5) and then Alkemade and Milatz (6) demonstrated the use of AA as an

analytical method. During the last nineteen years the technique has become established as one of the most versatile and widely used methods of trace element analysis.

In 1905 Wood was experimenting with sodium vapour lamps and observed the atomic fluorescence of the sodium D lines (7). After this initial discovery the atomic fluorescence (AF) of several other elements including Hg, Li, Cd and Zn was observed and again these early studies are summarised by Mitchell and Zemansky (4). The early workers used quartz cells to confine the atomic vapour, usually at reduced pressure. The first observation of AF in a flame was reported by Nichol and Howes (8) in 1923 and then by Badger (9) and Mankopff (10) who obtained weak signals from the elements Ba, Ca, Cd, Li, Mg, Hg, Na, Ag and Sr.

Atomic fluorescence was not used in the analytical context until 1964 when Winefordner and co-workers (11 - 14) published a series of papers describing the practical technique, and making an initial attempt at quantitative theory. Since then both Winefordner (15) and Dagnall, West et al (16 - 22) have developed the method to encompass some thirty-five elements.

1.2. STATEMENT OF INTENT.

A number of topics related to analytical spectrometry are studied in this thesis and although the chapters are interelated the work encompasses a wide range of basic theory. In the interests of continuity therefore, this statement of intent is included to define more clearly the links between the various sections.

The results presented relate mainly to the study of microwave excited plasma, emission spectrometry and the photon counting technique of signal measurement; however studies involving both AA and AF are also included. By way of introduction therefore a review of the properties required in an atomic emission excitation source is given and the discussion then extended to include the requirements for AA and AF.

Little is known about the physical processes that take place in steady state microwave plasmas and as yet no generally accepted theory is available. It is not therefore possible to give an account of the theory, before describing the actual experimental work that has been performed. The theory and characterisation of the plasma will therefore proceed throughout the second chapter, each section being related to the relevant experimental work. At the end of the chapter mechanisms for plasma excitation and operation are discussed.

Chapter III is an investigation of an emission spectrometric trace analysis system based on the plasma. Particular attention is given to the optimisation of the system and to its operating characteristics. A platinum loop sampling and vaporisation device was used with the plasma and this is described in detail. Observations of multiple peak vaporisation and metal atom adsorption on the platinum surface are reported. Explanations and possible applications

of these phenomena are considered.

Sampling is a critical factor in the analytical use of microwave plasmas and to date only one-shot devices producing transient spectral signals have proved successful. The measurement of transient signals requires techniques different to those normally employed in emission spectrometry. L'Vov (23) has presented theoretical work on the measurement of transient spectral signals and has elucidated the advantages of integral measurement. This work will be reviewed and two methods of signal integration described, capacitative integration and photon counting (24). At the time of first considering photon counting only one paper (25) discussing its use in atomic spectrometry had been presented. The validity of the results quoted was somewhat in doubt, and therefore to evaluate the technique more fully an extensive study of both photon counting hardware and measurement theory was undertaken; the results of this work are presented in chapters IV and V. Detailed circuit analysis is performed and criteria laid down for the choice of components. Two practical photon counting systems are described and their application to a number of systems, e.g. flame AE, AF and AA and non-flame AF and AA described. Statistical theory for photon counting measurement of analytical signals is presented, and particular attention given to the effect on signal to noise ratio of increasing count period.

1.3. THE PROPERTIES REQUIRED OF AN EXCITATION SOURCE IN ATOMIC EMISSION SPECTROMETRY.

The basic assumption of atomic emission spectrometry is that the intensity of the emitted radiation is proportional to the number of analyte atoms. Because the sample is usually in the solid or liquid phase, containing the analyte element in compound form, the source must be capable of both spectral excitation and free atom

production. By considering in more detail the steps involved between sample introduction and the emission of radiation the requirements of the excitation source will be defined.

An aqueous sample will undergo the following processes during emission analysis:

(i) introduction into the excitation medium.

(ii) desolvation and vapourisation of the analyte species (processes one and two may be reserved chronologically depending on the source chosen).

(iii) atomisation.

(iv) excitation of the free analyte atoms.

(v) radiative decay of the excited atoms.

Desolvation and vapourisation require thermal energy to overcome the latent heat of each process and to raise the temperature to the point at which the necessary phase changes occur rapidly. Temperature and total enthalpy of the source are therefore the thermodynamic quantities of importance, although it must be remembered that the kinetics of these processes will be affected by the physical state of the sample upon introduction (i.e. solvent, droplet size etc.). The total energy required to atomise the analyte in trace analysis is usually small and therefore the temperature and the chemical composition (especially the presence of oxidising species) within the source, usually determine the efficiency of the atomisation process. Similarly, the degree of excitation is strongly dependent on temperature (see equation 2.1.) but here other factors such as the nature of the exciting species and its number density are of importance. The probability of radiative deactivation occurring in preference to collisional deactivation has only a weak temperature dependence and

is largely determined by the quenching ability of the other chemical species and once again their number density. From these considerations it can be concluded that the ideal excitation source should have the following properties:

(i) a high, but not excessive temperature (ionisation limits the degree of excitation that can be achieved by temperature rises).

(ii) a total enthalpy great enough to supply sufficient energy to the sample without destroying the dynamic equilibrium which makes the source stable.

(iii) an inert chemical composition (occasionally specific chemical conditions such as a reducing atmosphere are more advantageous than inert conditions).

(iv) an absence of quenching species such as NO, CO, CO_2, N_2 etc. which promote collisional deactivation of excited states

and since the emission signal has to be measured

(v) a low background emission in the region of the spectrum being studied.

(vi) a high degree of stability.

Modern analytical flames such as air-acetylene (typical flow rates when used for emission C_2H_2, 1.8 $l\,min^{-1}$; air, 8.0 $l\,min^{-1}$) and nitrous oxide-acetylene (typical flow rates when used for emission C_2H_2, 2.16 $l\,min^{-1}$; N_2O, 4.0 $l\,min^{-1}$)attain temperatures of 2300 ° C and 3000 ° C respectively (26,27) and will produce (from samples introduced as aerosol sprays) adequate free atom populations for most elements (28). However, the moderate temperature of these flames prevents useful degrees of excitation occurring for those elements having their first excited states more than ca 3.5 eV above the ground state. The chemical reactions that occur in the combustion process,

for example:

$3/2\ O_2 + C_2H_2 \longrightarrow 2CO + H_2O$ + secondary products

$2N_2O + C_2H_2 \longrightarrow 2CO + H_2 + 2N_2$ + secondary products

and

$CO + \frac{1}{2}O_2 \longrightarrow CO_2^*$

produce a large number of species e.g. OH, CH, C_2, CO, CN, CO_2, NH, NO etc. which are then excited or are produced in the excited state (chemiluminescence) and result in an intense background radiation occurring over a considerable proportion of the visible and near U.V. spectrum. Kirkbright et. al. (29,31) have shown that separated flames may be used to advantage when background radiation is the limiting factor in analytical performance. Several of the common flames species e.g. O, O_2 and OH are oxidising agents and cause a reduction in the free atom population of certain elements by the formation of stable oxides e.g. SiO, Al_2O_3. Other species such as CO, NO and CN are efficient quenchers and therefore reduce the intensity of the emission signal.

This discussion of flames, though brief, does indicate that they are far from ideal sources for emission spectrometry. Many of the difficulties can be overcome, but the basic limitation remains that the kinetic energy of the individual particles is in general too low to excite efficiently atoms of elements other than those in the first two groups of the periodic table. Electrical sources of excitation do not suffer this basic limitation because the gaseous plasmas formed, in which the excitation takes place, usually contain highly energetic electrons with energies up to and above the ionisation potential of the carrier gas (e.g. 15.76 eV for Ar) Many electrical sources of excitation have been studied e.g. d.c. arcs (32,33), hollow

cathode discharges (34), RF plasmas (35), microwave plasmas (36), etc. and the difference often found between analytical systems using these sources and those employing flames is the method of sample introduction. Flames generate their energy internally and therefore each portion of the flame bulk may be regarded, to a first approximation, as self supporting. Plasmas however, derive their energy from an external source and it is therefore important that sample introduction does not seriously disturb the coupling between the plasma and the power source. In some cases it is convenient to fabricate one of the source electrodes (usually the cathode) from the sample material, although this is not always practical in trace analysis and indeed the presence of any electrodes invariably results in contamination of the plasma by the electrode material.

1.4. ELECTRODELESS PLASMAS AS SOURCES OF SPECTRAL EXCITATION.

The high frequency electrodeless discharge was discovered by Hittorf (35) in 1884 and a second paper by J. J. Thompson (37) appeared in 1891. The early work was carried out with evacuated glass vessels often sealed to form lamps. In 1928 Jackson (38) reported the use of an electrodeless discharge lamp (EDL) operated from a 10 M.Hz oscillator for the study of the spectrum of Caesium. Meggers et. al. (39 - 41) described the preparation of an EDL of Mercury 198 and proposed this source as a secondary wavelength standard.

The optimum frequency for lamp operation has been the subject of considerable study and it has been concluded by a number of workers that microwave frequencies ($>$ 500 M Hz) are the most suitable. Jacobsen and Harrison (42) found a sixteen-fold increase in intensity of the Hg 546.1 nm line from a lamp operated at 3000 M.Hz, compared

with the same lamp operated at 150 M Hz and at the same power. Forrester et. al. (43) reported that an EDL powered at 95 watts at 2450 M Hz gave ten times greater line intensity than one operated at 1 K W at 70 M Hz for the same emission line. There is also evidence (40,42) that lamp life i.e. the period during which an appreciable free atom population can be maintained is extended with increase of the operating frequency. A further convenience of using radiation of about 0.11 m wavelength, is that resonant cavities (44) to provide efficient coupling between the plasma and power source are easily constructed and have dimensions compatible with the normal optical systems used in emission spectrometry.

Today microwave powered EDLs made from quartz bulbs filled with a few torr of inert gas, usually argon and helium and a few mg of the required metal or metal halide (45 - 48) are commonly used as sources in atomic fluorescence spectrometry.

Sealed EDLs are not convenient for routine quantitative chemical analysis, as calibration of atomic line intensity versus elemental mass is impossible when lamp dimensions and operating conditions cannot be accurately reproduced. The free flowing, microwave excited, atmospheric pressure, argon plasma has therefore been studied as a more convenient adaption of the source for emission spectrometry (49). Free flowing devices have the advantage that they can handle a number of compounds either sequentially or simultaneously without serious memory effects.

1.5. THE ANALYTICAL CURVE IN ATOMIC EMISSION SPECTROMETRY.

The analytical curve describes the variation of the emitted line intensity with the concentration of the analyte element. The limiting point on the curve at the low concentration end represents the limit

of detection for the particular element. The concentration at which the limit of detection occurs depends on several factors of which the line oscillator strength (50), the thermodynamic temperature of the source, the degree of atomisation and the quality of the dispersive/detection system used are among the most important. In particular the dispersive/detection system should have a large aperture in order to collect a large solid angle of the emitted radiation, but a narrow band pass ideally approximating to the width of the emission line in order to reject unwanted background radiation.

When the atomic concentration in the excitation source is low, the line intensity corresponding to the integrated area under the line profile varies linearly with analyte concentration (52). (Current theories for AE consider only lines broadened by Doppler (23) and Lorentz (23) contributions and as yet no general theory for lines including significant Stark broadening (51) is available; experimental evidence however suggests that the presence of Stark effects does not seriously alter the shape of the analytical curve). This linear portion of the line represents the most important part analytically since precise calibrations can be made and extrapolation down to lower concentrations performed with confidence.

At high atomic density the number of analyte atoms is so great that the centre of the emitted line is strongly self absorbed by the excess of ground state atoms and at this point, the emission in the centre of the line approaches a maximum (according to the Planck black body radiator law) further emission occurring only from the line wings. Under these conditions the area under the emission profile, i.e. the intensity of the emitted line increases as the root of the atomic concentration (52). The effect on the line profile is to

flatten the peak and to broaden the wings. In certain instances a dip appears in the centre of the line profile, the process being known as 'self-reversal'. This occurs when analyte atoms diffuse into the cooler outer regions of the source and then absorb strongly the emitted radiation over a narrow line profile (both Doppler and Lorentz half-widths are proportional to the temperature). The high density portion of the analytical curve is less useful analytically, because the change in emitted intensity resulting from a change in the analyte concentration is somewhat less.

Analytical atomic emission curves obtained by actual measurement often deviate from the ideal case as described above. Variations in the degree of ionisation, the degree of dissociation, interferences and optical effects can cause deviations from ideality. For a mathematical treatment and fuller description of the analytical curve shape in AE, the reader is referred to the text by Mavrodineanu (50).

1.6. SOURCE AND ATOMISER REQUIREMENTS IN AA AND AF.

The function of the source in AE is to atomise and spectrally excite the analyte element; in AA and AF the functions of atomisation and excitation are separated, excitation being achieved by irradiating the free atom cloud with either a continuous or line source. Because the first step for each technique is the production of a free atom cloud, sources used for AE such as flames often prove suitable atomisers for both AA and AF. A brief list of atomiser and source requirements for AA and AF is given in the following sub-sections and where applicable comparisons drawn with source requirements for AE.

1.6.1. Atomiser Requirements in AA and AF.

The following are the properties required of an atomiser for AA and AF:-

(i) a temperature and enthalpy sufficient to vapourise and atomise

samples rapidly.

(ii) a low background emission.

(iii) stability of the background emission and free atom population.

(iv) an inert chemical composition free from oxidising species.

Differences occur between the techniques with regard to the presence of quenching species. AE and AF depend on radiational decay of the excited state occurring, whereas AA depends on the reverse process and thus the presence of quenchers reduces signals in AF and AE but may enhance signals in AA. Because excitation is achieved independently in AA and AF, several devices which produce atomic clouds by vapourisation from a hot surface have been employed e.g. the Massmann furnace (53), L'Vov furnace (54), West type filament (55) and the platinum loop atomiser (56). Provided that oxygen is excluded from the atomic cloud by a shielding gas, a free atom population can be maintained for a sufficient period to facilitate signal measurement. For AF non-quenching gases such as Ar or He are preferred but for AA quenchers such as N_2 or H_2 may prove optimum. In the later chapters of this thesis both flame and non-flame atomisers are used for AF and AA studies. Electrical plasmas e.g. d.c. arcs (57) and microwave plasmas (58) have also been used as atomisers for AA.

1.6.2. Source Requirements in AA.

(i) In AA the source is viewed directly by the detector and the quantity measured is the absorbed intensity. The magnitude of the absorbed intensity depends on the source intensity and therefore, although it is the fraction of radiation absorbed which varies linearly with concentration, it is still advantageous to have an intense source.

(ii) Maximum absorption occurs at the line centre and therefore it

is essential for high analytical sensitivity, that the source line is free from self reversal. Radiation falling outside the absorption profile of the analyte element cannot contribute to the absorbed intensity and therefore excessive broadening due to self-absorption, Doppler and Lorentz effects is wasteful and degrades the analytical sensitivity. Continuum sources can be used but only in conjunction with narrow band-pass monochromators, which prevent excessive amounts of radiation outside the spectral range of the absorption profile from reaching the detector.

(iii) high drift stability and freedom from noise.

1.6.3. Source Requirements in AF.

(i) The signal intensity is directly proportional to the exciting line intensity for AF and therefore a high intensity source is a prerequisite for high analytical sensitivity.

(ii) The detector does not view the source in AF and therefore the width of the exciting line profile is not of the same importance as in AA. Strongest excitation occurs at the line centre where the absorption coefficient is greatest and therefore the source should be free from self reversal. Continuum sources can be used to good advantage in AF (particularly for multi-element analysis) without the necessity for high resolution monochromators.

(iii) High drift stability and freedom from noise.

The most widely used source in analytical atomic spectrometry is the hollow cathode lamp (HCL) (34), which is capable of providing an intense narrow emission profile, free from serious self reversal effects, for most elements. These lamps have proved ideal sources for AA, but for many elements have lacked sufficient intensity for use in AF. The electrodeless discharge tube (EDL) has yielded higher emission

intensities than the HCL for a number of elements (45 - 48) and though line broadening due to self-absorption, Doppler and Lorentz effects has limited their use in AA, they have often proved superior for AF. Both HCLs and EDLs were used to obtain some of the results presented in this thesis. The continuum source most widely used is the xenon arc (59), continuously operated at powers of typically 500 W and capable of being pulsed at peak powers of several kilowatts. The intensity of continuum sources is generally less than that of the line sources, but this is in some degree compensated by a lower background noise (60).

The general discussion of atomiser and source requirements in AE, AF and AA has been limited to physical properties and has not included the more practical considerations of cost, operating lifetime and simplicity.

1.7. THE ANALYTICAL CURVE IN AA.

The purpose of this thesis is not to study the shapes of analytical growth curves, however a number of such curves will be shown and therefore a brief description of their salient features is in order. For AA it is the fraction of radiation absorbed that is plotted versus the atomic concentration. Many analysts convert this ratio (52) to absorbance (A), but since the growth curves for α and A are linear over approximately the same region this exercise seems unnecessary. Modern theories for curve shapes in AA and AF are based on a mixed line profile, comprising Doppler and Lorentz contributions expressed in the form due to Voigt (61). The line profile then has a parameter known as the 'damping ratio (a)' which is numerically equal to $(\ln 2)^{\frac{1}{2}}$ times the ratio of the Lorentz to Doppler half width. The effect of the 'a' value on curve shapes in AA (23) and AF (62) has been discussed,

however no further consideration will be given here as the 'a' value will be treated as a parameter of the atom reservoir.

1.7.1. Line Source.

At low atomic density the absorption α varies linearly with the analyte concentration and it is this region that is of analytical importance. When the atomic density is high the radiation from the line source is almost totally absorbed and α approaches asymptotically a value of unity.

1.7.2. Continuum Source.

Once again when the atomic density is low the absorption varies linearly with the anlyte concentration. At high concentration the centre of the absorption profile completely absorbs the incident radiation and further absorption can then only occur in the line wings. The change in the absorption profile with increasing atomic concentration is completely analagous to the change in the emission profile in AE, and therefore at high concentration the absorption varies as the root of the atomic density. Indeed growth curves for AA with a continuum source have an identical shape to growth curves in AE. The apparent broadening of line profiles at high atomic concentrations is in fact a statistical effect (ignoring possible resonance broadening (51)), because the number of atoms is so large that the absolute emission or absorption occurring at points in the wings of the probability distribution (line profile) is greater.

Deviations from the predicted curve shape for both line and continuum sources in AA, and AF, occur for the same reasons as in AE, i.e. variations in dissociation and ionisation, interferences and optical effects (52).

1.8. THE ANALYTICAL CURVE IN AF.

The analytical curve in AF consists of a plot of the emitted intensity versus the analyte concentration and once again the damping ratio is a parameter. AF can be viewed as a series combination of AA and AF and this is reflected in the shape of the analytical curves.

1.8.1. Line Source.

The first part of the curve is linear, since at low atomic density the absorption of radiation varies linearly with concentration and there is no significant self absorption of the emitted beam. At high atomic density however, all the incident radiation is absorbed and then self absorption of the emitted beam occurs in proportion to the route of the atomic concentration. The result is that the slope of the analytical curve becomes negative, the final asymptote being proportional to the reciprocal route of the concentration. The curve then, exhibits a maximum whose position and width can be shown to depend on the damping ratio (63).

1.8.2. Continuum Source.

When a continuum excitation source is used, the initial section of the curve is linear, corresponding to linear absorption of the exciting beam and freedom from self absorption effects. For the high density case, the exciting beam is entirely absorbed at the line centre and further absorption occurs in proportion to the route of the atomic concentration. The emitted beam also suffers absorption in proportion to the route of the atomic concentration with the result that the final asymptote is horizontal. The part of the curve corresponding to intermediate concentrations exhibits a slight maximum (not always observed in practice) whose position and pronouncement is dependent on the 'a' value.

ooo000ooo

CHAPTER II

AN INVESTIGATION OF THE PHYSICAL PROPERTIES OF A MICROWAVE EXCITED ARGON PLASMA

2.1. INTRODUCTION.

This chapter will be concerned with determining some of the physical properties of a microwave excited, atmospheric pressure argon plasma. The most important property of the plasma is the nature of the equilibrium, because once this is known all the other properties can be calculated from bulk system parameters such as the temperature and the electron density. Measurement of these parameters is in itself the first step in determining what kind of equilibrium pertains, and therefore the first part of the chapter will describe a number of methods that were employed to estimate plasma temperature. More than one method of temperature measurement will be described because as will become apparent in the section on plasma mechanism, more than one temperature can be ascribed to the plasma. Once the relevant temperatures have been found, electron density is calculated on the basis of an assumed equilibrium and the results compared with those from other recently published work. The nature of the equilibrium is then determined by theoretical tests and its relevance to microscopic plasma processes discussed.

The determination of meaningful temperatures enables plasma particle energies to be estimated, which in turn allows for calculation of collision cross sections and electric field strength. These properties are important because they indicate the manner in which plasma particles gain energy from the high frequency microwave field. This process is of particular significance in relation to the mechanism of ionisation, which will be discussed towards the end of the chapter.

A plasma can be defined as a body of gas having a proportion of its constituent atoms in the ionised state. As such it can be expected to contain neutral groundstate atoms, excited atoms, ions and free

electrons. The spectral characteristics of a plasma are determined by atomic parameters such as the transition probabilities and the statistical weights and by the relative populations of the various quantum states. For dense laboratory plasmas the population of states is usually controlled by collisional processes, but in certain instances, e.g. resonance transitions, radiative processes may dominate.

The concept of Local Thermodynamic (thermal) Equilibrium (LTE) is often used in plasma spectroscopy. A system in LTE has a population of states identical to that of a system in complete thermodynamic equilibrium having the same total density (mass), temperature and chemical composition as the actual system. The equilibrium is described as local, because it is assumed that the population of states is controlled by collisional processes only, and that the relevant temperature is that which describes the distribution function of the species dominating the reaction rates. The dominating species is the electrons and their distribution function Maxwellian. The reason for the domination of the electrons is that their velocities are much higher and their cross sections at least not lower than those of any other plasma particle. A notable exception is the momentum transfer cross sections which are small for particles of different masses, the exchange occurring in the ratio of the masses of the colliding species. The result is that whilst the distribution function of the atoms, ions and electrons is Maxwellian their kinetic temperatures may be quite different.

The plasma parameters of spectroscopic interest therefore are the temperature and density of the free electrons, and a knowledge of these quantities will indicate the excitation mechanism. However a

temperature has no spectroscopic significance unless related to a defined equilibrium be it LTE or Coronal (the equilibrium that occurs when the population of states is controlled jointly by radiative and collisional processes). The problem in its generality is complex but a fruitful approach is to assume that LTE exists, measure the temperature and electron density by a number of different methods and then apply a theoretical self consistency check to verify the assumptions. Griem (51) has calculated from first principles a number of validity criteria for the LTE assumption and these will be applied to the experimental results at the end of this chapter.

2.2. DETERMINATION OF THE ELECTRON TEMPERATURE BY THE RELATIVE INTENSITY OF SPECTRAL LINES METHOD.

2.2.1. Theory.

The intensity of a spectral line originating from an optically thin (i.e. there is no self-absorption) LTE plasma is given by (50):

$$I = \frac{hcN_o g_u A}{Q(T)\lambda} \cdot \exp(-E_u / kT) \text{ watts cm}^{-3} \text{ st}^{-1}. \quad .... \quad 2.1.$$

where h is the Planck's constant,

c is the velocity of light,

N_o is the number of free atoms,

g_u is the statistical weight of the level E_u,

Q(T) is the partition function,

A is the Einstein transition probability for spontaneous emission,

λ is the wavelength of the spectral line,

k is the Boltzmann constant

and T is the absolute temperature.

Equation 2.1 forms the basis of a number of methods of temperature determination, the most obvious being the measurement of the absolute intensity of a spectral line and calculation of T by insertion of the

known constants, and N_o (determined independently). This method is rarely used because calibration of the optical system is extremely arduous and precise values of transition probabilities are not always known. A simpler approach is to measure the relative intensities of two spectral lines (denoted m and n)and thus avoid the complicated calibration procedure required for absolute intensity measurement. For this so-called 'Two Line Method' equation 2.1. is written in the form

$$\frac{I_m}{I_n} = \left[\frac{g_{um}A_m\lambda_n}{g_{un}A_n\lambda_m}\right] \cdot \exp\left[\frac{(E_{un} - E_{um})}{kT}\right] \quad .... \quad 2.2.$$

from which T can be determined. The Two Line Method is convenient and yields good accuracy when the transition probabilities of the lines are well known. Kirkbright et. al. (64) determined the temperatures of some analytical flames by nebulising solutions of iron into them and measuring the relative intensities of various pairs of iron lines. When the transition probabilities are not well known as is the case for Ar ($\pm$ 25%) equation 2.1 may be written

$$\log_{10}\left(\frac{I\lambda}{g_uA}\right) = -\frac{E_u}{2.303kT} - \log_{10}\left(\frac{Q(T)}{hcN_o}\right) \quad .... \quad 2.3.$$

and the temperature determined by measuring the relative intensities of a series of lines. The results are plotted on a graph of $\log_{10}(I\lambda/g_uA)$ versus E_u in which case random errors in the quoted transition probabilities should tend to average out.

For moderate temperatures the Boltzmann factor $\exp(-E_u/kT)$ ensures that a large proportion of the atoms remain in the ground state and for this reason equation 2.1 rarely applies to resonance lines, because the emitted radiation is self absorbed by the preponderance of ground state atoms. To avoid errors caused by self-absorption and

by radiative depopulation of the excited state, spectral lines that do not terminate in the ground state are preferred for intensity measurement. Self absorption still occurs for lines terminating in higher levels, but this problem can be overcome by selecting lines that are self absorbed to the same extent.

Consider therefore a parallel beam of light emitted from a continuous source of radiation passing through a layer of monatomic gas of thickness x. If the intensity of the incident beam is I_o then the transmitted intensity I_ν is given by

$$I_\nu = I_o \exp(-K_\nu x) \qquad \ldots.2.4.$$

where K_ν is the absorption coefficient at the frequency ν

Now let the gas atoms possess an upper energy level u and a lower level l, then transitions between these levels will be described by the three Einstein transition probabilities B_{lu}, A_{ul} and B_{ul}

where B_{lu} is the absorption transition probability

and B_{ul} is the stimulated emission transition probability

Suppose there are N_o atoms per cc of which δN_ν are capable of absorbing in the frequency range ν to $\nu + \delta\nu$ and N' excited atoms of which $\delta N'$ are capable of emitting radiation in this frequency range. The loss of energy from a parallel isotropic beam of radiation of intensity I_ν between ν and $\nu + \delta\nu$ when travelling between planes at x and $x + \delta x$ is given by (4):

$$dI_\nu \, d\nu = \frac{A_{ul}}{4\pi} \cdot h\nu \, n_u dx + \frac{I_\nu}{4\pi} \cdot h\nu \, dx \, (B_{ul}n_u - B_{lu}n_l) \qquad \ldots.2.5.$$

Assuming that collisional population of the states dominates, the spontaneous emission term can be omitted leaving

$$\frac{-dI_\nu}{I_\nu} \frac{d\nu}{dx} = \frac{h\nu}{4\pi} \left(B_{lu} \delta N_\nu - B_{ul} \delta N'_\nu\right) \qquad \ldots.2.6.$$

but from 1.4

$$\frac{-dI_\nu}{I_\nu}\frac{d\nu}{dx} = K_\nu$$

therefore $K_\nu \, d\nu = \frac{h\nu}{4\pi} \left(B_{lu} \delta N_\nu - B_{ul} \delta N'_\nu\right)$

The total absorption of the line K is thus given by the integral of $K_\nu \, d\nu$ over the line width which yields

$$K = \int K_\nu \, d\nu = \frac{h\nu}{4\pi} \left(B_{lu} N - B_{ul} N'\right) \qquad \ldots.2.7.$$

where ν is now the frequency at the centre of the spectral line,

N is the number of atoms in the state 1

and N'is the number of atoms in the excited state u.

Now since (4) $$A_{ul} = \frac{2h\nu^3}{c^2} \frac{g_l}{g_u}$$

and $$\frac{B_{ul}}{B_{lu}} = \frac{g_l}{g_u}$$

$$K = \frac{h\nu}{4\pi} N B_{lu} \left(1 - \frac{g_l}{g_u} \frac{N'}{N}\right) \qquad \ldots.2.8.$$

Normally the proportion of atoms in the excited state is small and therefore $g_l N' / g_u N$ can be ignored. Substitution for B_{lu} yields

$$K = \frac{\lambda^2}{8\pi} A_{ul} \frac{g_u}{g_l} N \qquad \ldots.2.9.$$

Now if the population of states obeys a Boltzmann Law corresponding to a temperature T then (65)

$$\frac{N}{N_o} = \frac{g_l \exp\left(-E_l/kT\right)}{Q(T)}$$

and equation 2.8 becomes

$$K = \frac{\lambda^2 N_o A_{ul} g_u}{8\pi Q(T)} \exp\left(-E_l/kT\right) \qquad \ldots.2.10.$$

Thus for two lines denoted m and n the ratio of their integrated absorption coefficients is given by

$$\frac{K_m}{K_n} = \left(\frac{g_{um} A_m \lambda_m^2}{g_{un} A_n \lambda_n^2}\right) \exp\left[\frac{\left(E_{ln} - E_{lm}\right)}{k T}\right] \qquad \ldots.2.11.$$

and for lines self absorbed to the same degree the ratio will be equal to unity. This criterion will be used in the following sections to select the lines for temperature measurement.

The intensity of a spectral line viewed at right angles to the plasma axis may not exactly represent the emitted intensity as expressed by equation 2.1, because the observed intensity is integrated throughout the plasma depth. Scanning across the plasma at right angles to the axis does not therefore yield a true radial temperature profile. The true radial profile may be resolved from the observed profile by making a series of radial intensity measurements (usually 30 or more) and subjecting them to an Abel transform (66). Microwave plasmas run at atmospheric pressure have a natural radius of ca 1.0 mm resulting from the self generated magnetic field which effectively 'bottles' the plasma. For this reason no Abel transform was performed, because of the difficulty of collecting adequate radial data on such a small emitting column. Certainly the errors introduced by not transforming the data are lessened by the limited physical depth of the plasma and in any case analytical measurements are always made on the observed intensities.

2.2.2. The Plasma.

The plasma was operated in a 2 mm quartz tube (quartz is preferred because it is transparent to both U.V. and microwave radiation) inside a $\frac{3}{4}$ wave resonant cavity (Electro-Medical Supplies type 210), designed to operate at 2450 M Hz. Power was drawn from an E.M.S. "Microtron 200" generator, maximum plasma stability being obtained with the input power at 65 W and the argon flow at 250 ml/min. After initiation with a 'Tesla' coil a bluish purple plasma of about 11.0 cm length was formed. Figure I shows a survey of the plasma between 275.0 and 440.0 nm.

The most intense emissions are tabulated in Table I together with a few weak systems occurring outside the spectral range of the plot shown.

Table I. Observed emissions from the microwave plasma.

Peak Number	System	Wavelength (nm)
1	OH	308.9
2	NH	336.0
3	N_2 second positive	337.1
4	N_2 second positive	357.6
5	Ar (not resolved)	394.7; 394.9
6	Ar (not resolved)	404.5; 404.4
7	Ar (not resolved)	415.8; 416.4
8	Ar	418.2
9	Ar (not resolved)	419.0
10	Ar (not resolved)	419.8; 420.1
11	Ar	425.9
12	Ar	426.6
13	Ar	427.2
14	Ar	430.0
15	Ar (not resolved)	433.3; 433.5
16	N_2 second positive	434.3
17	CO Angstrom	451.0
18	H	486.3
19	C_2 Swan Band	516.5

The presence of N, C, O and H indicated impurities in the argon, probably N_2, CO_2 and H_2O from the cylinder and from the gas flow system. Attempts to purify the argon have succeeded in decreasing the concentration of nitrogen containing molecules, but the OH band is

very persistent. This is to be expected when the gas flow system consists mainly of glass and polythene (as was the case here) which do not prevent the adsorption of water vapour. The relative intensities of the peaks in Fig. I are only approximate because the wavelength scan speed used was too great to allow for full recorder response to occur. It should be noted that none of the Ar^{II} lines e.g. 351.78 nm and 406.06 nm appear on the trace which indicates a temperature under 10000 ^{c} K. (Ar^{II}, Ei = 27.63 eV).

The standard $\frac{3}{4}$ wave cavity does not respond critically to tuning and this does promote stable coupling of the microwave power to the plasma. The electric field in this type of cavity appears to be quite uniform since no discontinuities were visible along the plasma length.

2.2.3. Optical Considerations.

At the time of starting the work on temperature measurement the only instrument available was a Hilger Large Quartz Spectrograph employing photographic recording. Argon has two series of lines that broadly fulfill the criteria for temperature measurement, the 4s - 4p series at 690 - 760 nm and the 4s - 5p series at 390 - 430 nm. Whilst it is far superior to employ both series of lines for temperature measurement, thus giving a greater range of E_u, the prism instrument had insufficient dispersion at 700 nm to make this possible. The relative intensities of the argon 4s - 5p series were therefore recorded on Ilford N-30 plates which are U.V. sensitive.

The random nature of photon emission from the plasma and fluctuations in the microwave power, tuning and gas flow results in noise on the optical signal. Photographic recording measures the intensities of all the lines simultaneously and therefore tends to

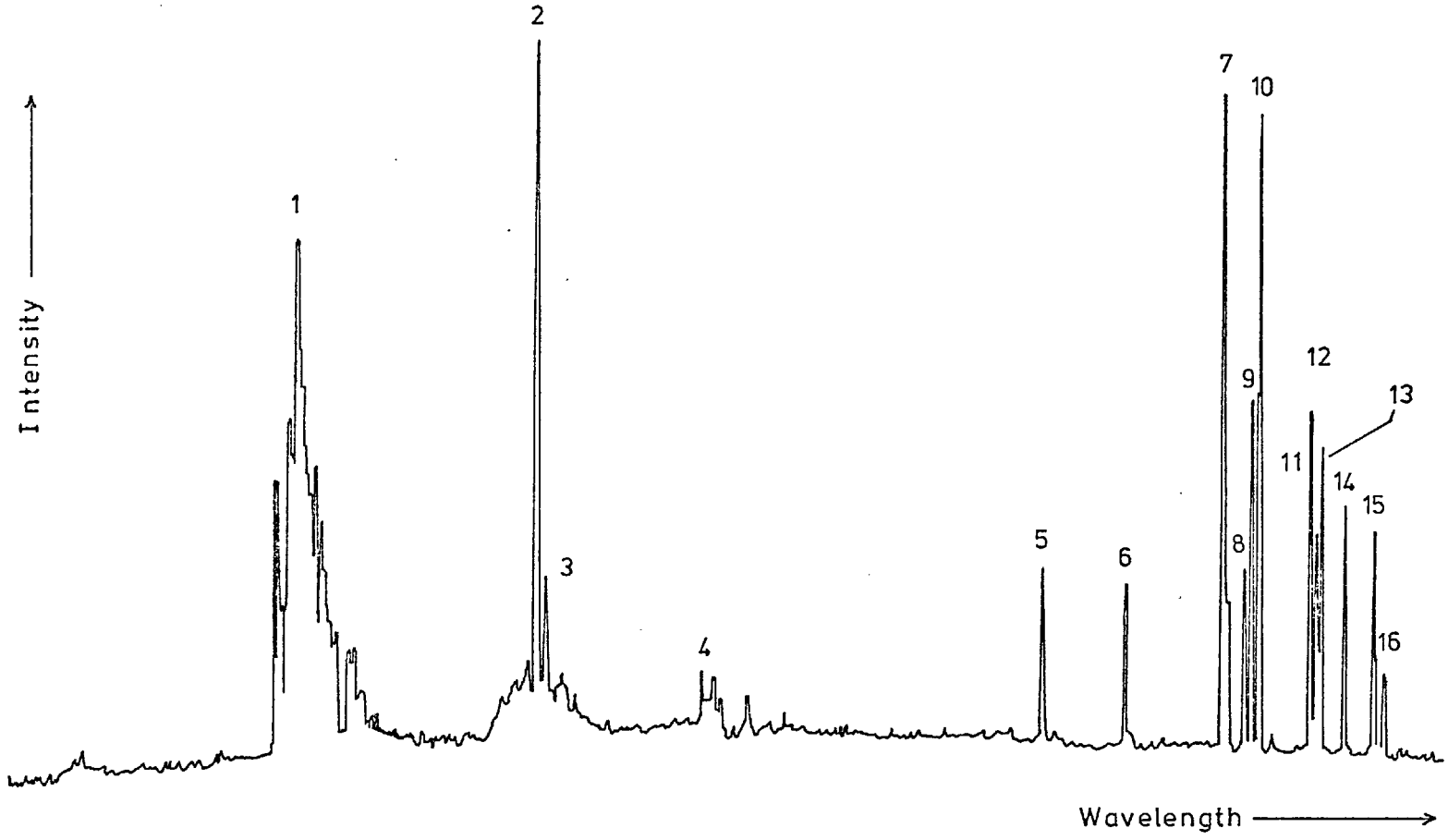


Fig. 1. Microwave plasma spectrum between 275.0 and 440.0nm.

remove errors due to fluctuations in the plasma radiation output. Errors caused by random photon emission are lessened because the optical signal is integrated over the exposure period.

The cavity and plasma tube were mounted on the optical bar of the spectrograph and a 7.5 cm focal length, quartz lens employed to focus the image of the plasma onto the entrance slit. Care was taken to ensure that the centre portion of the plasma image coincided with the slit opening. Before exposures were taken the slit jaws were cleaned and then set to 15 microns width. Because the image of the plasma completely filled the slit, the solid angle of light falling on the photographic plate was controlled entirely by the aperture of the spectrograph. The wavelength control of the spectrograph was adjusted so that the plate covered a range from 297.0 - 600.0 nm, which located the 4s - 5p series lines close to the plate centre. After initiation of the plasma, a period of one hour was allowed for the cavity and plasma tube to reach thermal equilibrium before exposures were taken.

2.2.4. The Photographic Recording Method.

(i) Identification of the Argon Lines

Initial identification of the argon lines was made by comparison with an iron spectrum, photographed adjacent to the plasma spectrum (15 min. exposure) on the same plate. The wavelength of the iron lines was determined by comparison with a standard plate. Fig. 2 shows a chart recorder trace of the argon spectrum, the lines for convenience being numbered 1 - 14. Table 2 lists the lines and their associated constants, the values are from Corliss and Schumaker (67). The transition probabilities are averages of the values given in the literature and the uncertainties are calculated from the spread of these results.

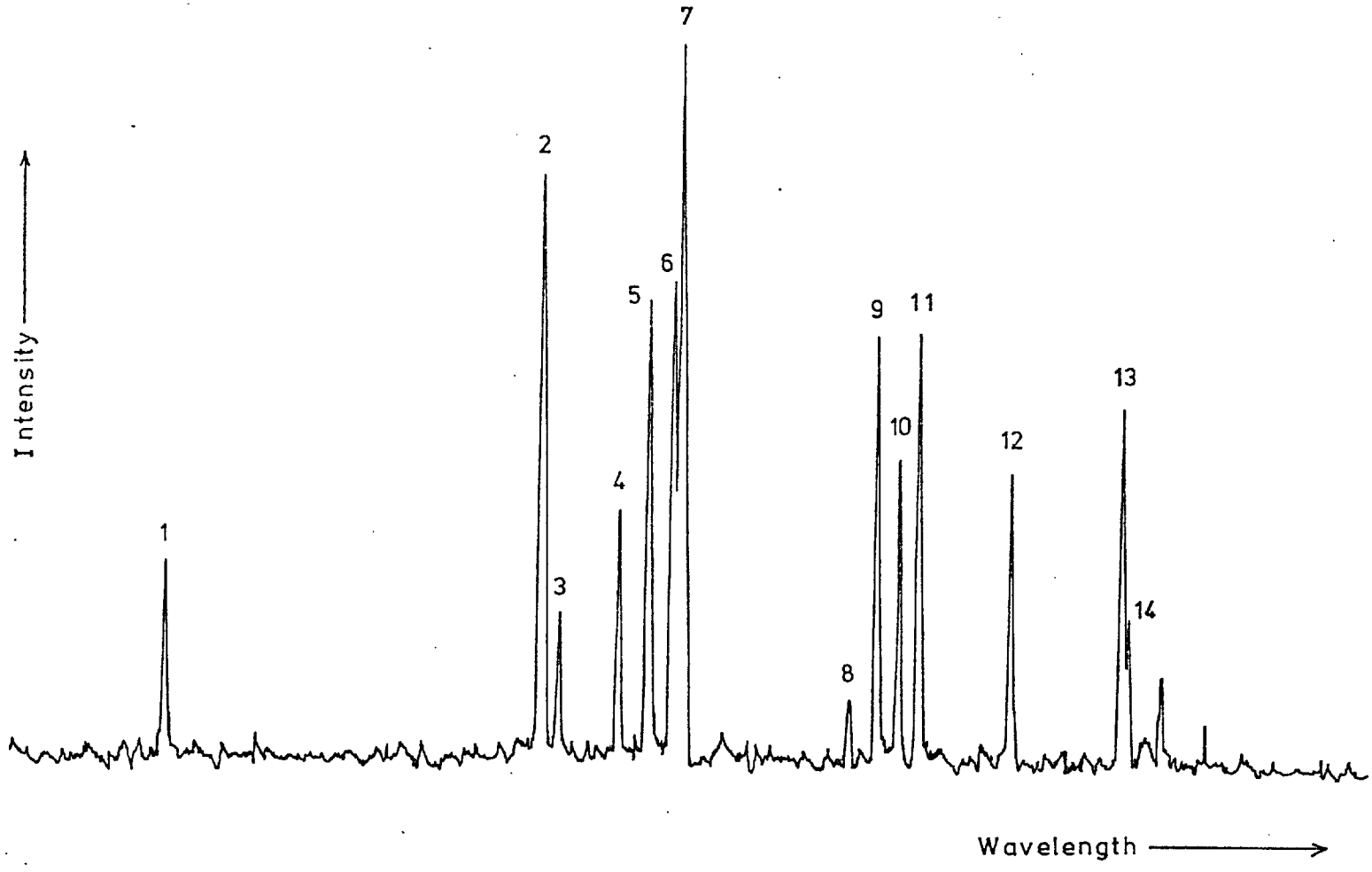


Fig. 2. Argon 4s-5p series lines from the microwave plasma.

Table 2. Argon 4s - 5p series transitions and wavelength data.

Line Number	Wavelength (nm)	Transition	$A_{ul} \times 10^{-5}$ (sec^{-1})		g_u	$E_u \times 10^{-3}$ (cm^{-1})
1	404.442; 404.596	-	-		-	-
2	415.859	$^1S_5 - {}^3P_6$	15.5	1.4	5	117.184
3	416.418	$^1S_5 - {}^3P_7$	2.73	0.23	3	117.151
4	418.188	$^1S_3 - {}^3P_2$	5.3	0.8	3	118.460
5	419.071; 419.103	-	-		-	-
6	419.832	$^1S_4 - {}^3P_5$	31.0	0.4	1	117.563
7	420.067	$^1S_5 - {}^3P_9$	10.0	0.5	7	116.943
8	425.118	$^1S_5 - {}^3P_{10}$	1.1	0.14	3	116.660
9	425.936	$^1S_2 - {}^3P_1$	45.0	4.0	1	118.871
10	426.629	$^1S_4 - {}^3P_6$	3.3	0.2	5	117.184
11	427.217	$^1S_4 - {}^3P_7$	8.7	0.4	3	117.151
12	430.010	$^1S_4 - {}^3P_8$	4.1	0.2	5	116.999
13	433.356	$^1S_2 - {}^3P_3$	6.2	0.3	5	118.469
14	433.534	$^1S_2 - {}^3P_2$	4.3	0.3	3	118.460

(ii) Emulsion Calibration.

Before attempting intensity measurements from a photographic plate the characteristics of the light sensitive emulsion were determined. This was necessary because each emulsion responds differently to wavelength and to time of exposure. The wavelength range of the measurements was only 18 nm and therefore little variation in wavelength response was expected. This was confirmed by exposing the plate to the emission of a tungsten ribbon standard lamp and comparing the relative intensity at different wavelengths to that predicted by the Planck relation i.e.

$$I_T(\nu) = \frac{2h\nu^3}{c^2} \left[\exp\left(\frac{h\nu}{kT}\right) - 1 \right]^{-1}$$

where T is the black body temperature in degrees absolute.

A more important consideration was that of exposure time or total optical density on the plate. The normal time/optical density relation for an emulsion is shown in Fig. 3. The curve approximately obeys the Law

$$\text{optical density} \propto \log t$$

where t is the exposure time. However, the curve is not entirely linear and therefore care must be taken to ensure that density measurements are made only on the linear portion of the slope. Generally line intensities are measured in the presence of background radiation and therefore the optical densities of the two have to be subtracted. If the total and background density are not on the linear part of the curve, distortion of the relative intensities results. The method most commonly used for determining emulsion characteristics is is the rotating logarithmic step sector. The sector is cut so that when rotated at high speed in front of the spectrograph slit, the image of the slit is exposed in sections for periods of time that are related by a logarithmic law. This technique is particularly useful when the source is intense and only short exposure times are required. Attempts to use the device with the plasma were unsatisfactory because the sector and its focussing lens obscured the slit jaws, thus making it impossible to focus the small image of the plasma centrally on the slit aperture. A number of trial exposures were made with the plasma and these indicated that times of 1 - 16 minutes would yield satisfactory spectra. With exposure times of this length it was possible to calibrate the emulsion, without loss of accuracy due to timing errors simply by making timed exposures. Furthermore by using a Hartmann diaphram twelve exposures could be

made on a single 4 x 10 inch N-30, thereby avoiding the necessity of cross standardising the emulsions of several plates.

Argon spectra were recorded with exposure times of 1, 2, 4, 6, 8, 12 and 16 minutes on a single plate. The plate was placed in developer for 4 minutes, in fixer for $4\frac{1}{2}$ minutes, washed with distilled water and finally rinsed with methanol to remove any surface marks. The total optical density of each line on each spectrum was then measured with a Joyce-Label automatic recording microdensitometer. Hence, an emulsion calibration for each resolved spectral line was constructed by plotting the total optical density versus the log of the exposure time. Two such calibration curves for the 418.188 nm and the 425.936 nm lines are shown together with the model curve in Fig. 3. The straight lines drawn are least squares lines fitted to the first four points of each curve by linear regression analysis. The calculations were performed on an I.B.M. 7094 computer, the program being written to include calculation of the standard deviation of the optical density measurements.

A microdensitometer scan of a clear section of the plate produced a flat baseline indicating uniform development of the plate and a flat wavelength response of the emulsion over the region of spectrum covered by the 4s - 5p series lines.

(iii) Relative Line Intensity Measurements.

The total optical density measured for a particular line represents the sum of the line intensity and the argon continuum intensity. Before the relative intensities could be calculated therefore, the optical densities recorded on the plate for the two emissions had to be subtracted. This procedure is only valid if the total and background density both fall on the linear portion of the emulsion calibration.

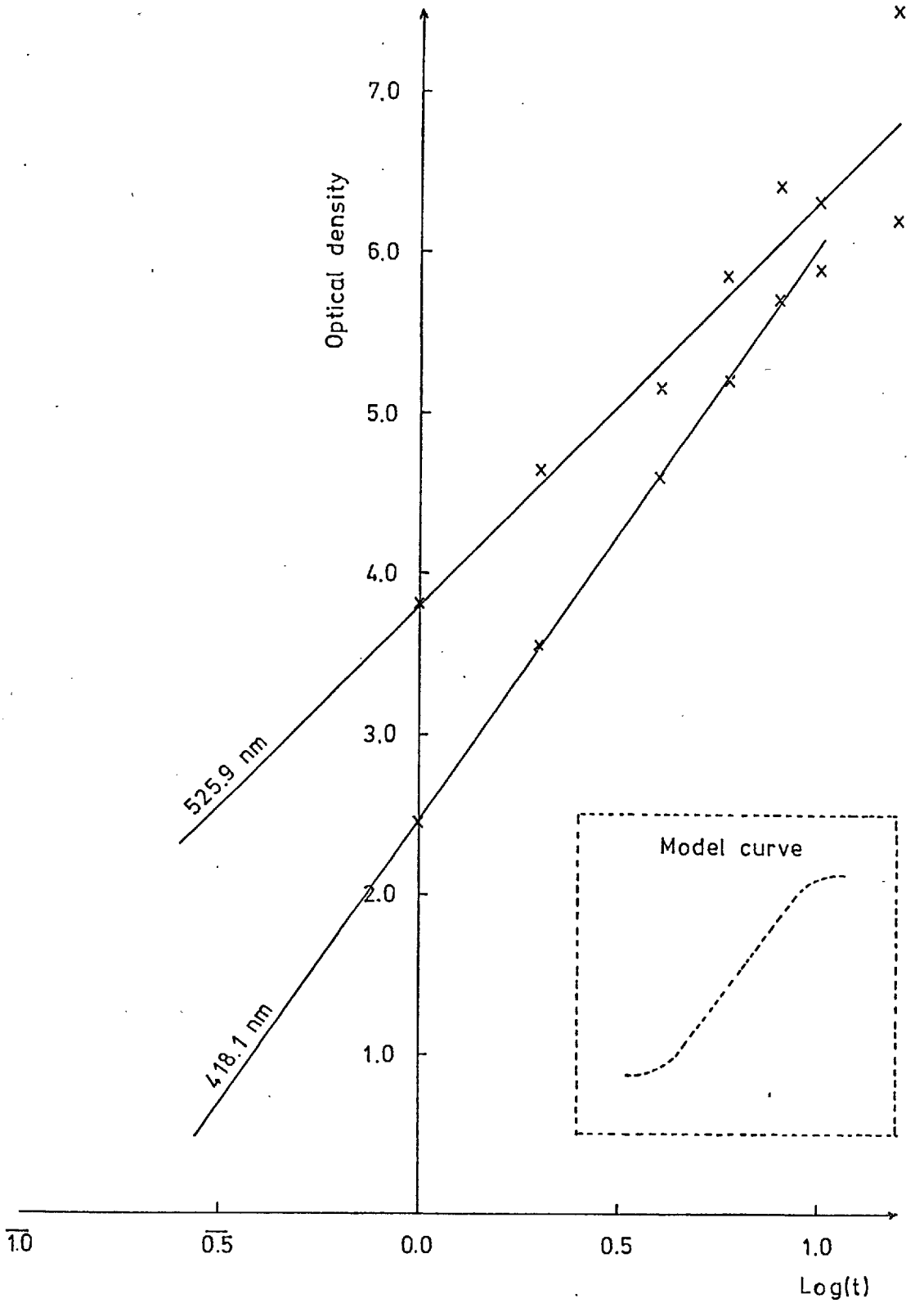


Fig. 3. Emulsion calibration curves.

For this reason only the 1, 2, 4 and 6 minute exposures were used for temperature measurement.

Line intensities were measured from the four spectra by taking the total density as that given by the least squares line, and subtracting from it the background density at that wavelength. Using these results and the values quoted in Table 2, four plots of $\log_{10}(I\lambda/g_u A_{ul})$ versus E_u were constructed. The plot from the one minute exposure is shown in Fig. 4, the numbers of the points correspond to the numbers of the lines. Now had the errors associated with each point on the graph been random, the distribution of points about a straight line would have been different for each of the four plots. This was not the case and indeed the distribution of points about a straight line was very similar in each graph.

Self absorption was thought to be responsible and therefore a computer program was written in order to solve equation 2.11 for all possible line combinations. Before the program could be run an estimate of the plasma electron temperature was obtained from the dotted line drawn in Fig. 4. This line was drawn by inspection and yielded a temperature of ca 4000 ° K which was then used to calculate the ratios given in Table 3. The results do not give the absolute extent to which each line is self-absorbed, and indeed because of errors in the transition probabilities the ratios are subject to uncertainty. However, it can be seen that lines 2 and 7 are considerably self-absorbed with respect to the other lines, and this was reflected in their low ordinate values on all the $\log(I\lambda/g_u A_{ul})$ versus E_u plots. With respect to each other they are self-absorbed to a similar extent i.e. $K_2/K_7 = 1.09$. Alternatively line 8 appears to be less self-absorbed than any other line ($K_2/K_8 = 22.47$, $K_7/K_8 = 20.71$) and this was confirmed by high ordinate values on each of the plots.

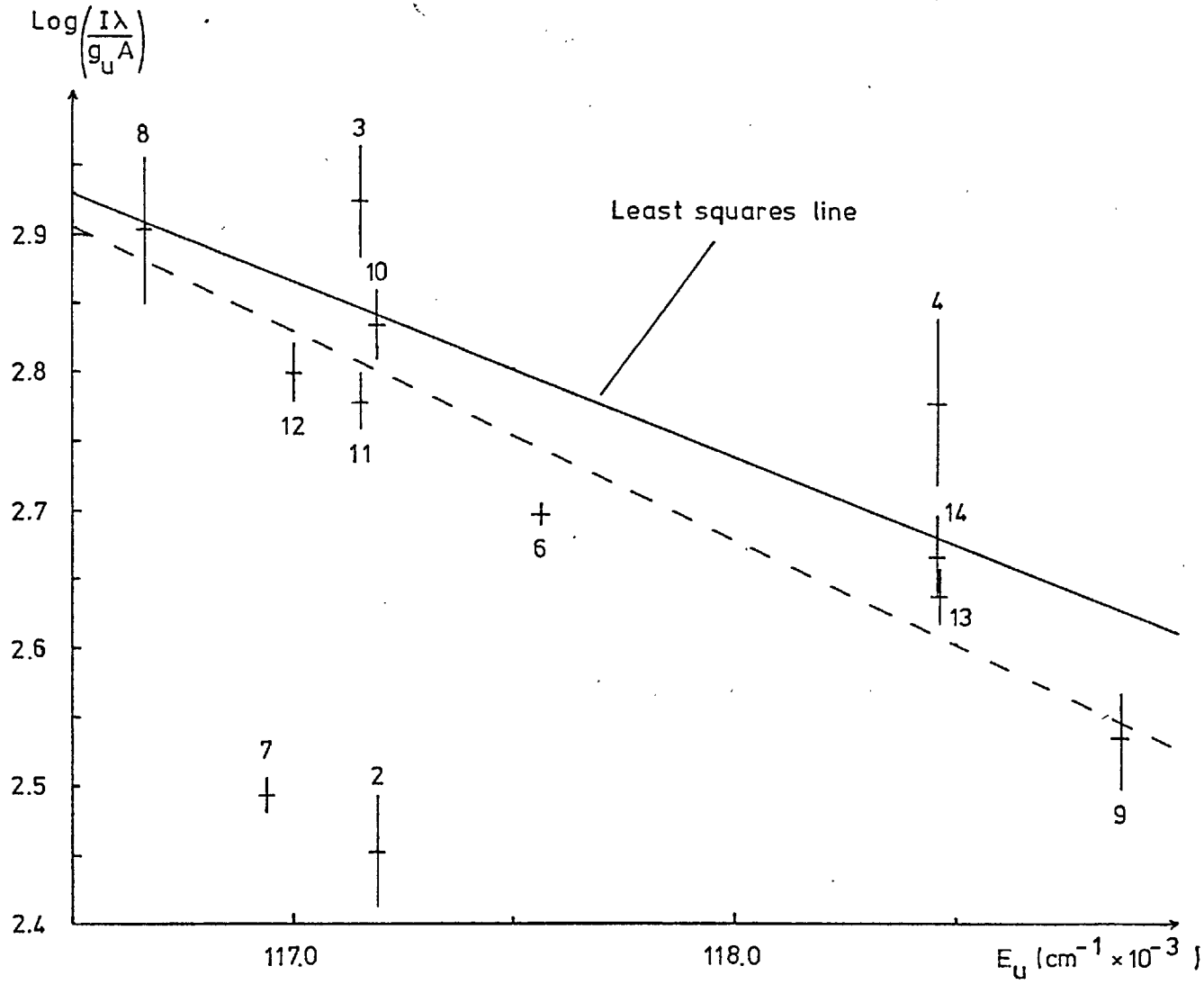


Fig. 4. Relative line intensity plot for the argon 4s-5p series (1 minute exposure)

Table 3. Self-absorption Coefficient ratios (K_m/K_n) for twelve argon lines at 4000° K

		NUMERATOR K_m											
		K_2/	K_3/	K_4/	K_6/	K_7/	K_8/	K_9/	K_{10}/	K_{11}/	K_{12}/	K_{13}/	K_{14}/
DENOMINATOR K_n	K_2	1.0	0.11	0.13	0.33	0.92	0.04	0.27	0.18	0.29	0.23	0.19	0.08
	K_3	9.44	1.0	1.18	3.09	8.70	0.42	2.55	1.70	2.70	2.15	1.82	0.76
	K_4	8.01	0.85	1.0	2.62	7.38	0.36	2.17	1.44	2.29	1.82	1.54	0.64
	K_6	3.05	0.32	0.38	1.0	2.81	0.14	0.83	0.55	0.87	0.69	0.59	0.25
	K_7	1.09	0.12	0.14	0.36	1.0	0.05	0.29	0.20	0.31	0.25	0.21	0.09
	K_8	22.47	2.38	2.81	7.37	20.71	1.0	6.08	4.05	6.42	5.11	4.34	1.81
	K_9	3.70	0.39	0.46	1.21	3.41	0.16	1.0	0.67	1.06	0.84	0.71	0.30
	K_{10}	5.55	0.59	0.69	1.82	5.12	0.25	1.50	1.0	1.59	1.26	1.07	0.45
	K_{11}	3.50	0.37	0.44	1.15	3.23	0.16	0.95	0.63	1.0	0.80	0.68	0.28
	K_{12}	4.40	0.47	0.55	1.44	4.05	0.20	1.19	0.79	1.26	1.0	0.85	0.35
	K_{13}	5.18	0.55	0.65	1.70	4.78	0.23	1.40	0.93	1.48	1.18	1.0	0.42
	K_{14}	12.45	1.32	1.56	4.08	11.47	0.55	3.37	2.24	3.56	2.83	2.40	1.0

On the basis of these calculations it was decided not to employ lines 2, 7 and 8 in the temperature determination. Consideration was also given to rejecting line 6 because it was not fully resolved from line 7, however because it fell reasonably close to the straight line and because this was an initial attempt at temperature measurement, it was included.

A least squares line was fitted to the chosen points on each graph and the temperatures as calculated from the slopes listed in Table 4.

Table 4. Results of electron temperature measurement by photographic method.

Exposure time (minutes)	Slope x 10^{-3} (cm)	Intercept	Standard deviation of the ordinates	Temperature °K
1.0	-0.126	17.609	0.066	4960
2.0	-0.109	15.704	0.106	5730
4.0	-0.101	14.766	0.137	6190
6.0	-0.103	15.081	0.138	6070

The numerical mean of these results is 5738 ° K, but this result does not take into account the spread of the data points. A better estimate of the mean was therefore obtained from normalised data. In theory each curve has the same slope but a different intercept and therefore by subtracting the intercept from each data point, all the points could be considered as falling on a single straight line. The line through the normalised data was computed by the least squares method and yielded a final average of 5680 ° K.

(iv) Error analysis for graphically determined temperature.

A number of methods can be employed to estimate the error in the final temperature. Vertical error bars drawn on the graph in Fig. 4 indicate the maximum and minimum values of the ordinate, calculated from the quoted errors in the transition probabilities. Using these bars to draw a 'worst' straight line through the data was not considered a valid method of calculating the error, because it is unlikely that all the errors would combine in one particular sense. Similarly to have used the standard deviations of the ordinates in like manner, would have yielded a result in excess of the probable error. The total probable uncertainty in the final result was therefore determined by computing the standard deviation of the four temperature estimates, using the mean calculated from the normalised data. Thus the electron

temperature of the plasma was estimated to be

$$5680 \pm 480\ ^{\circ}K$$

Having estimated the total uncertainty in the temperature measurement, this section will be concluded with a discussion of the sources of error. Probably the most significant source of error was self-absorption of the lines, which was clearly illustrated by the fact that in nearly every plot the same points were distributed on the same side of the line each time. A more careful selection of the lines may have improved the precision, but a better solution would have been to include the 4s - 4p series in the determination.

The largest deviation from the mean temperature occurred with the one minute exposure. Study of the model emulsion calibration (Fig. 3) indicates that this exposure may have been subject to failure of the curve linearity at low optical density. Furthermore as it was the shortest exposure taken, the uncertainty in the timing was the greatest.

Instability in the plasma undoubtedly contributed to the variation in temperature between exposures. Random fluctuations in power, coupling and gas flow as well as long term drift in each of these parameters could have contributed to variations in the electron temperature.

Another possible source of error was the occurrence of band emissions superimposed on the argon lines, thus causing false intensity measurements. No such bands were observed but errors from this source or perhaps from molecular fluorescence of the quartz cannot be entirely discounted.

2.3. DETERMINATION OF THE ELECTRON TEMPERATURE BY THE RELATIVE LINE-CONTINUUM METHOD.

2.3.1. Theory.

The line spectrum emitted by a plasma results from electron

transitions between bound atomic states. The energy spread of the photons emitted by this process is small, approximating to the sum of the energy widths of the two stationary states. Free (ionised) electrons may also make transitions into bound states but because the upper level of the transition effectively comprises an infinite number of energy states, the emitted radiation is continuous. This is known as Recombination radiation. An electron moving through a plasma is constantly accelerated and decelerated by the local potential field of the ions and therefore emits photons due to transitions between unbound i.e. continuous energy states. These free-free transitions of the electrons make a contribution to the continuum known as Bremsstrahlung radiation. The total continuum intensity at the frequency ν is therefore given by

$$I_\nu^c = I_\nu^r + I_\nu^b$$

where I_ν^r is the intensity at the frequency ν due to recombination and I_ν^b is the intensity at the frequency ν due to Bremsstrahlung

Now it has been shown that (65),

$$I_\nu^r \, d\nu = KZ^4 n_e \frac{N^z}{n^3} \, G_{fb} \left(\frac{kT_e}{E_i} \right)^{3/2} \cdot \exp - \left(\frac{h\nu + \Delta E_i}{kT_e} \right) \cdot \sum_{n'}^{\infty} \exp \left(\frac{Z^2 E_i}{n' kT_e} \right) d\nu \qquad \ldots.2.12.$$

where k is a constant,

Z is the charge on the ion,

n_e is the concentration of free electrons,

N^z is the number of ions per unit volume,

G_{fb} is the free-bound Gaunt factor,

E_i is the unperturbed ionisation potential of the atoms,

E_i is the depression of the ionisation potential

and n' is the principal quantum number set by the Inglis Teller limit (68).

The derivation of equation 2.12 is complex, but it will suffice here to point out salient features which serve to illustrate the mechanism of the recombination process. The recombination process may be represented by

$$Ar^{+}(N^{1}) + e(n_e) \rightarrow Ar(N) + h$$

and it is obvious that the intensity of the radiation emitted is proportional to the reaction rate,

that is $I_{\nu}^{r} \propto \frac{dN^{1}}{dt} \quad (Ar^{+})$

$$\propto \Omega\, n_e N^{1}(Ar^{+}) \qquad \ldots.2.13.$$

where Ω is the recombination emission coefficient.

Now n_e and N^{1} can be calculated from the Saha Equation and Ω from the electron cross sections for recombination. Equation 2.13 should then describe the rate of emission of photons having energies up to E_i (the unperturbed ionisation potential). However, in practice two factors tend to reduce the ionisation potential below that for an isolated atom.

In a plasma each electron and ion is surrounded by a net charge of the opposite sign which is not entirely broken down by thermal agitation. The result is that ionisation occurs at energies lower than E_i because following the production of an electron ion pair there is a release of energy caused by the coulombic attraction of the neighbouring particles. The other factor arises from the Stark shift and broadening of bound states caused by local electron and ion fields. Inglis and Teller (68) showed that at high values of the Principal quantum number n where the energy difference between states is small (for Hydrogenic systems $\Delta E \propto (1/n^2 - 1/(n+1)^2)$) the Stark effect would 'drown' out discrete levels resulting in an advance of the Series Limit from $n = \infty$ to $n = n'$. The range of photon energies

should therefore be given by the inequality

$$h\nu \lesssim E_i - E_g - \Delta E_i \qquad \ldots.2.14.$$

where E_g results from the Stark drowning of discrete levels and E_i is the depression of the ionisation potential due to Coulombic interaction.

Obviously then, the expression on the right hand side of equation 2.14 will appear in Saha type expressions and in calculation of the partition functions since

$$Q(T) = \sum_{n}^{n'} g_n \exp(-E_n/kT) \qquad \ldots.2.15.$$

Indeed without the effective series limit, the sum in equation 2.15 would diverge and an arbritrary cut-off procedure would have to be employed.

The intensity of the Bremsstrahlung radiation is given by (65)

$$I^b = Kn_e N^Z Z^2 . \frac{G_{ff}}{2} \left(\frac{E_i}{kT_e} \right)^{\frac{1}{2}} \exp -\left(\frac{h\nu + \Delta E_i}{kT_e} \right) d\nu \qquad \ldots.2.16.$$

where G_{ff} is the free-free Gaunt factor.

Equation 2.16 is calculated from classical electromagnetic theory and once again includes the dimensionless Gaunt factor wich is employed to unify the results from classical theory with those from wave-mechanical treatment.

Olsen (69) and Johnston (70) have calculated the total continuum intensity of argon for a 1.0 Å band centred at 426.2 nm and with substitution of constants and correction factors obtained

$$I^c_\nu \Delta\nu = 5.07.10^{-34} \frac{n_e^2}{(T_e)^{\frac{1}{2}}} \exp - \frac{(h\nu - E_g + \Delta E_i)}{kT_e} \text{ watts cm}^{-3} \text{ st}^{-1}. \qquad \ldots.2.17$$

Now the Saha equation can be written

$$N_o = n_e N^1 \frac{\hbar^3}{2(2\pi mkT_e)^{3/2}} \frac{Q(T)}{Q_i(T)} \exp\left(\frac{E_i}{kT} \right) \qquad \ldots.2.18$$

where N^1 is the number of singly charged ions.

m is the mass of the electron

$Q_i(T)$ is the partition function of the ion.

Re-stating equation 2.1

$$I_\nu^l = \frac{hcN_o g_u A_{ul}}{Q(T)\lambda} \cdot \exp\left(\frac{-E_u}{kT}\right)$$

and substituting for N_o from the Saha equation in which the numerator in the exponential has been converted to $(E_i - \Delta E_i)$ yields

$$I_\nu^l = \frac{h\nu\, g_u A_{ul}}{Q_i(T)} \cdot \frac{n_e^2}{T_e^{3/2}} \cdot \frac{\hbar^3}{2(2\pi mk)^{3/2}} \exp\left(\frac{E_i - E_u - \Delta E_i}{kT_e}\right)$$

Now substituting in constants for the Ar 425.9 nm line yields

$$I_\nu^l = 3.86.10^{-30} \frac{n_e^2}{T_e^{3/2}} \exp\left(\frac{E_i - E_u - \Delta E_i}{kT_e}\right)$$

and therefore the ratio of the line to continuum intensity is

$$\frac{I_\nu^l}{I_\nu^l} = \frac{7.61.10^3}{T_e} \cdot \exp\left(\frac{E_i - E_l - E_g}{kT_e}\right) \qquad \ldots.2.19$$

since $h\nu = E_u - E_l$

where E_l is the lower energy level of the transition.

Now Olsen calculated $E_g = 3.047.10^{-19}$ J.

and since $E_i = 2.525.10^{-18}$ J.

$E_l = 1.896.10^{-18}$ J.

and $k = 1.38 .10^{-23}$ J. C^{-1}. molecule^{-1}

$$\frac{I_\nu^l}{I_\nu^c} = \frac{7.61.10^3}{T_e} \exp\left(\frac{2.35.10^4}{T_e}\right) \qquad \ldots.2.20$$

Thus the ratio of the line to continuum intensity (R) at a given wavelength can be expressed as a function of T_e only and this function is plotted in Fig. 5 for values of T_e from 10000 - 15000° K.

2.3.2. Experimental.

The instrument chosen for measuring the line to continuum ratio was a Hilger Watts D330 monochromator, fitted with a grating having

1200 lines per mm (blaze 350 nm) which yielded a linear dispersion of 26 A per mm in the plane of the exit slit. The width of the exit slit was therefore adjusted to 38 microns giving the required spectral band-pass of 1 Å at the detector.

Radiation passing through the exit slit was detected by an EMI 6256S photomultiplier tube, having an S type photo-cathode which has a peak spectral response at about 390 nm. For the purpose of identifying the 425.9 nm line and the continuum at 426.2 nm, the output of the photomultiplier was displayed on a Servoscribe potentiometric recorder having a 20 K ohm load resistor across its input terminals. Intensity measurements were made with the photomultiplier used in the photon counting mode (see later chapters). This enabled integration of the light signal and therefore an increase in the precision of measurement (see chapter 5). The line and continuum intensity and the dark count were taken as the average of four ten second counts.

The optical arrangement was similar to that used for the relative line intensity measurements. The image of the plasma was focussed centrally on the monochromator entrance slit, which was set at 38 microns to correspond to the width of the exit slit. To prevent excess light reaching the detector the height of the entrance slit was reduced with a Hartmann diaphram to about 1 mm. As before one hour was allowed for the plasma system to stabilise before readings were taken.

2.3.3. Results.

Photon counting measurement yielded the following results

Average dark count from the photomultiplier	= 11437 counts
Total intensity of a 1 Å band centred at 426.2 nm	= 34302 counts
Total intensity of a 1 Å band centred at 425.9 nm	= 109297 counts

from which the true line intensity was calculated as 74995 counts and the true continuum intensity as 22865. The ratio of the line to continuum intensity was therefore 3.28 which from Fig. 5 corresponds to an electron temperature of 13350° K. Johnston (70) estimated a 15% uncertainty in equation 2.20 most of the error being associated with the emission coefficient of the continuum.

Systematic errors caused by self-absorption of the 425.9 nm line and wrong wavelength settings, together with random errors due to noise on the optical signal add to the uncertainty in the final result. The 425.9 nm transition does not appear to be strongly self-absorbed (see Table 3 and ref. 71) however some self-absorption is inevitable. The uncertainty in the optical signal was found to be about 2% and allowing for errors not amenable to calculation, an over all error of 20% was considered to be realistic. The temperature extremes corresponding to a 20% error are shown in Fig. 5 and from these the final result was calculated as

$$T_e = 13350 \pm 1000^\circ K$$

This result is seriously at variance with the temperature obtained by the relative line intensity method. For a collision dominated LTE plasma the two results should be identical and therefore reasons for the discrepancy must be sought. Firstly the validity of the LTE assumption must be doubted since both Johnston (70) and Olsen (67) have obtained consistent temperatures from LTE argon plasmas using expressions identical to those presented here. Secondly consideration must be given to the possibility that the continuum intensity is being added to by a process not considered in equation 2.20. Molecular fluorescence of the quartz or emission from the Ar_2^+ molecular ion could be occurring but the spectral plots of the plasma

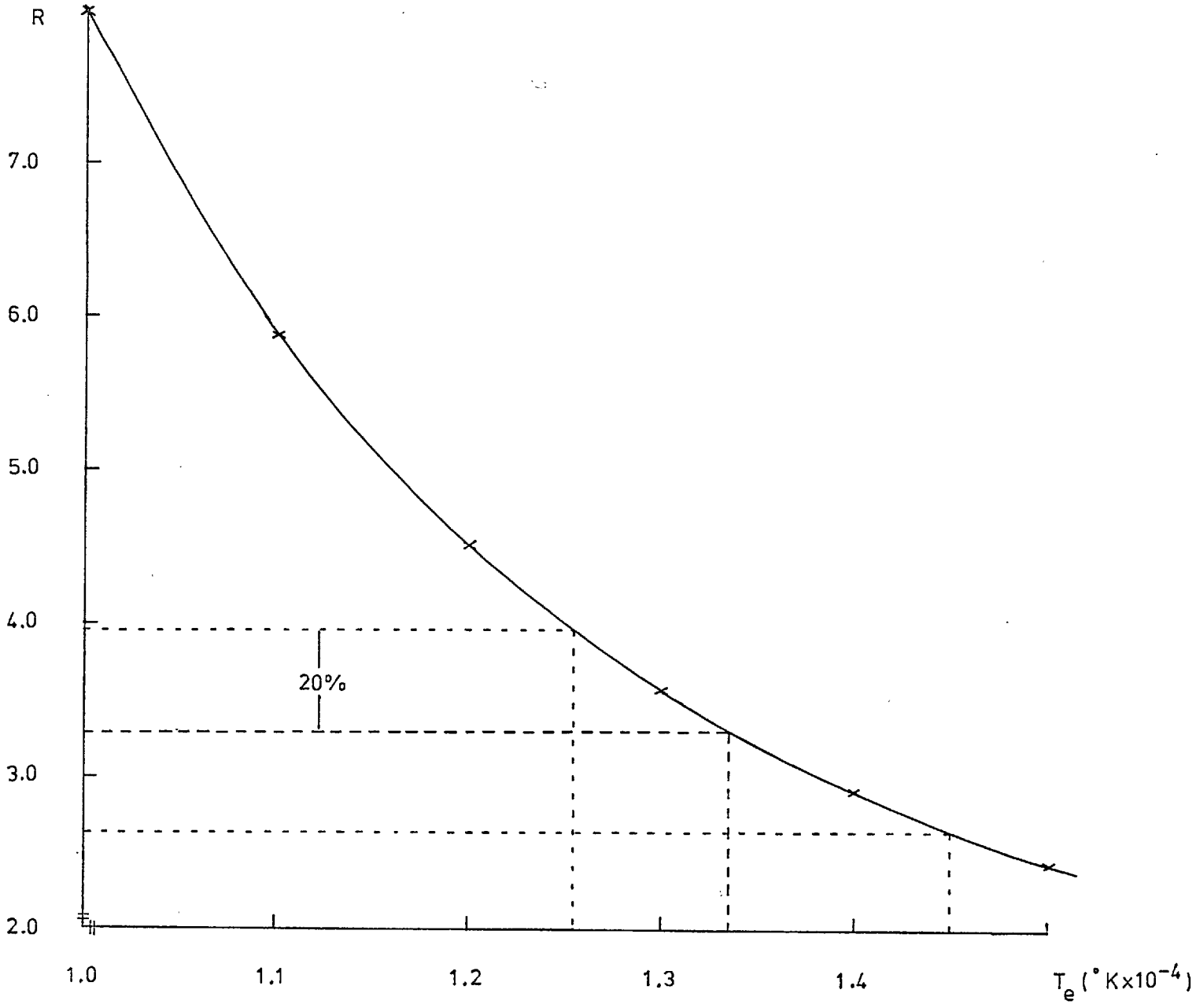


Fig. 5. Plot of line to continuum ratio versus electron temperature.

do not indicate any broad band emissions in the 400 to 450 nm range. The Ar_2^+ molecular ion is formed on the collision of an excited argon atom with a ground state argon atom (72):-

$$Ar^* + Ar \longrightarrow Ar_2^+ + e^- \qquad \ldots.2.21$$

Equation 2.21 indicates a third mechanism which may cause erroneous results from the line to continuum method. The formation of the ion decreases the number of excited Ar atoms thus reducing the intensity of the line emission. This mechanism is likely to be of importance at atmospheric pressure since the required collision is most probable. Dissociation of the molecular ion results in the emission of vacuum ultra-violet radiation.

Having dealt with some possible explanations of the temperature discrepancy, further discussion will be left until a formal test of the LTE assumption has been made.

2.4. DETERMINATION OF THE ELECTRON TEMPERATURE BY THE DOUBLE PROBE METHOD.

Electrostatic probes enable plasma parameters such as electron temperature and density to be determined independently of spectroscopic quantities. They therefore serve as a useful check on results obtained by spectroscopic techniques and unlike other non-spectroscopic methods such as microwave diagnostics, the equipment required is extremely simple. Generally probes are used for studying low temperature plasmas in which the probe can be immersed without vapourising and therefore contaminating the plasma gas. The gas temperature of the microwave plasma was estimated (see section 2.5) initially to be 750 ° C and therefore platinum probes were considered suitable.

A probe inserted into a plasma initially collects more electrons than ions because of the greater electron velocities. A negative potential is therefore established on the probe (known as the Floating

Potential V_f) such that some of the electrons are repelled, thus balancing the electron and ion currents. The positive ions form a sheath round the negative probe and from this point the ion current becomes insensitive to further negative changes in the probe potential. If however the probe is made more positive, an electron begins to flow which may become large enough to seriously disturb the plasma equilibrium.

Johnson and Malter (73, 74) suggested the use of double probes which do not draw large currents from the plasma and therefore disturb the equilibrium. Furthermore double probes require no reference electrode and are therefore suitable for use with electrodeless plasmas. The circuit used to obtain the double probe characteristics is shown schematically in Fig. 6. In practice a stabilised d.c. supply was used to bias the probes and voltages and currents measured with a Marconi digital volt meter having an electrometer input. The plasma operating conditions were as before with the argon flow rate at 250 ml min^{-1} and the input power at 65 W. Probes were made from 0.1 mm diameter platinum wire protruding from quartz insulators and were inserted through serum caps sealed onto each end of the plasma tube (2 mm inside diameter). The length of each probe was made approximately equal, actual measurement with a travelling microscope showed the dimensions to be Probe I = 2.22 mm and Probe 2 = 1.70 mm.

A typical double probe characteristic is shown in Fig. 7.

where I_d is the current flowing in the external circuit

V_d is the differential probe voltage

i_{ei} is the electron current to probe i (i = 1,2)

i^s_{pi} is the saturated ion current to probe i (i = 1,2)

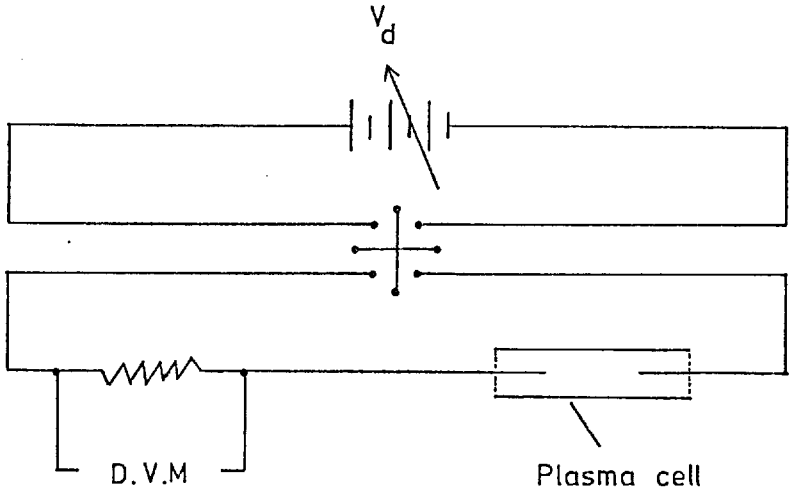


Fig.6. Plasma probe circuit.

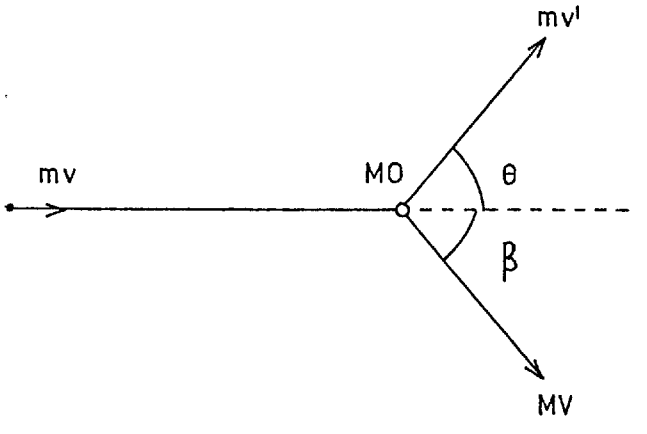


Fig.9. Schematic electron-atom collision.

2.4.1. Theory of electron temperature measurement.

Assuming the electrons to have a Maxwellian distribution of velocities and the plasma to be an equipotential volume (in fact potential gradients do exist in plasmas because of the different diffusion rates of electrons and ions and because of spatial variations in the external field; however probes can be adjusted spatially to yield zero potential at which point the equipotential condition is approximately satisfied), then the electron current collected by a probe is given by

$$i_{ei} = Aj_o \exp -\left(\frac{eV}{kT_e}\right) \qquad \ldots.2.22$$

where A is the probe area

j_o is the random current density in the plasma

and V is the retarding probe potential

Maintaining the condition that there can be no net current drain from the plasma (the plasma is neutral in bulk) i.e. the total electron and ion currents are equal and opposite, then the condition at various potentials can be considered:

$V_d = 0$

Both probes float at the floating potential V_f and since there is no net potential in the circuit $I_d = 0$ (point a on Fig. 7)

V_d small and negative

Probe 2 becomes more positive and collects more electrons whilst probe 1 becomes more negative and collects less electrons, in accordance with equation 2.22. The result is that electrons pass through the external circuit from probe 2 to probe 1 restoring the balance and moving to point b on the characteristic.

V_d larger and negative

Probe 2 now collects the entire electron current to the system and i_{e1}

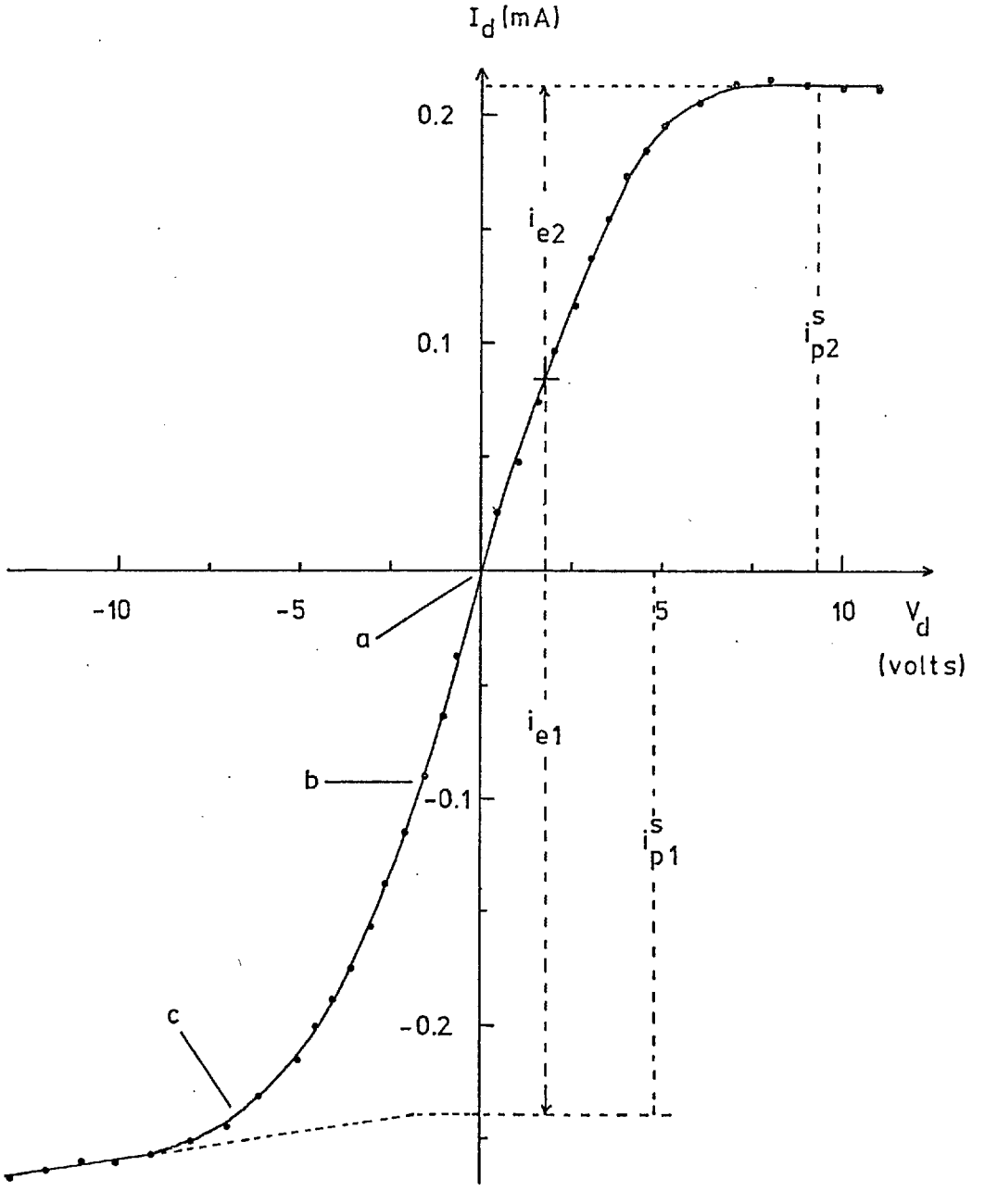


Fig. 7. A typical double probe characteristic.

drops to zero. For equal sized probes, half the electrons flow through the circuit to probe 1 and point c on the characteristic is reached.

V_d large and negative.

i_{e2} equals the saturated ion current i_p^s and therefore no further current change occurs. As V_d is made more negative the potential of P_2 remains fixed whilst P_1 becomes more negative with V_d. A slight increase in current does occur after saturation and this is attributed to expansion of the ion sheath at higher negative potentials. Under these conditions Johnson and Malter showed that i_{pi}^s should be measured at a point 0.8 of the distance, between the break of the extrapolated saturated ion current line with the characteristic and the ordinate axis (see Fig. 7). The saturated ion current is several orders of magnitude less than the saturated electron current (i.e. electron sheathed operation) and therefore the double probe method does not disturb the plasma equilibrium. Where probes are of different area and the equipotential condition is not entirely fulfilled, the characteristic may not quite pass through zero (see Fig 7), however no serious error results.

In order to determine the electron temperature from the characteristic Johnson and Malter calculated the following relations

$$T_e = 11{,}600\ (G - G^2)\ \sum\ i_{pi}^s \left(\frac{dV_d}{dI_d}\right)_{V_d = 0} \qquad \ldots.2.23$$

where $\left(\frac{dV_d}{dI_d}\right)_{V_d = 0}$ is the slope of the characteristic at $V_d = 0$ (i.e. the resistance).

$$\sum i_{pi}^s = i_{p1}^s + i_{p2}^s$$

and $$G = \left(\frac{i_{e2}}{\sum i_{p1}^s}\right)_{V_d = 0}$$

where $\left(i_{e2}\right)_{V_d = 0} = \left(I_d\right)_{V_d = 0} - \left(i_{p1}\right)_{V_d = 0}$

Six characteristics were plotted and using equation 2.23 temperatures of 25580, 21650, 23900, 24950, 23030 and 26400° K were obtained. The mean temperature was 24250° K and the standard deviation approximately 1600 °K (six results are insufficient to accurately estimate the standard deviation). The temperature is much higher than that determined by the other two methods because only high energy electrons i.e. those with energies in excess of eV_f are sampled by the double probe technique. These electrons occur in the high energy tail of the distribution (see section 2.8.1.) and are responsible for maintaining the ionisation equilibrium. More consideration will be given to the mechanism of ionisation in the concluding sections of this chapter.

Normally probe characteristics can be used to determine electron concentrations, but this was not the case for the atmospheric pressure plasma. The theory given above was developed for probes operated in low pressure plasmas, where the mean free path of the electrons is greater than the probe diameter and sheath thickness. For plasmas operated at higher pressures the current is modified by collisions of the changed particles with neutral atoms. The probable effect of the collisions is to decrease the rate of change of current with voltage and to disturb the purely exponential relationship of equation 2.22. The error introduced into the temperature measurement however, may not be too serious, because whilst the differential term in equation 2.23 gets larger the G term probably decreases. It seems a reasonable assumption that under ion sheathed operation, the total saturated ion current will be less affected by increase of pressure than the electron current. A possible way of viewing the

situation is that equation 2.23 applies only to those electrons within one mean free path of the probe. The result is that whilst the theory may provide an estimate of the electron energy, it would almost certainly give erroneous results if used to determine their number density. A theory of single probe operation at high particle density has been given (75), but it requires accurate knowledge of electron and ion mean free paths and temperatures.

2.5. DETERMINATION OF THE NEUTRAL ARGON TEMPERATURE.

The previous experiments have been aimed at determining the electron temperature and have yielded results in excess of 5000° K. If the neutral argon was of this order then it would not be possible to contain the plasma in a quartz tube and indeed the fact that the quartz can tolerate contact with the plasma for long periods indicates a gas temperature below 1000° K. The most convenient device for measuring gas temperatures in a confined space is a low thermal capacity thermo-couple. The difficulty associated with using a thermo-couple to measure plasma gas temperature, is that the hot junction cannot be immersed in the plasma because large and spurious e.m.f. s are generated by the local electric field. The technique adopted therefore was to measure the temperature at various positions down stream from the plasma and to construct a graph of temperature versus distance from the plasma. The gas temperature within the plasma was then determined by extrapolation and the results checked by studying the action of the plasma on various compounds of known melting point.

For these measurements it was necessary to view the plasma at a point outside the cavity and to achieve this the power had to be increased to 70 W (the length of the plasma increased with increasing

microwave power). The cavity and plasma tube were mounted horizontally and the thermo-couple clamped axially within the quartz tube. A chrome-alumel thermo-couple was used, its cold junction kept in iced water and the e.m.f. s generated recorded with a Servoscribe potentiometric recorder. Temperatures corresponding to the measured e.m.f. s were taken from N.B.S. calibration tables.

The distance between the plasma and the thermo-couple was measured using a travelling microscope and to allow for slight variations due to plasma flicker, several readings at each position were taken. Ten minutes were allowed before each set of readings in order to ensure thermal equilibrium of the thermo-couple with the gas. The results of these measurements are shown in Fig. 8. Extrapolation of the curve to the ordinate axis indicated a gas temperature of about 690 ° C.

The melting point experiments were carried out using the salts KIO_3 (m.p. 560 ° C), LiCl (m.p. 613 ° C), V_2O_5 (690 ° C) and KBr (m.p. 730 ° C). Each salt was ground to produce small crystals and then a few of these were placed in the plasma tube and viewed with the travelling microscope. The plasma was then initiated and the crystals which were immersed in the plasma, studied for signs of melting. It was found that KIO_3 and LiCl melted rapidly whilst KBr remained in the solid state after an exposure of several minutes. V_2O_5 melted slowly in the plasma requiring about one minute for all the solid phase to disappear.

From the thermo-couple measurements and the melting point observations it was concluded that the gas temperature in the plasma was approximately 690 ° C. It should be noted that these measurements related to the tip of the plasma where the quartz was somewhat cooler

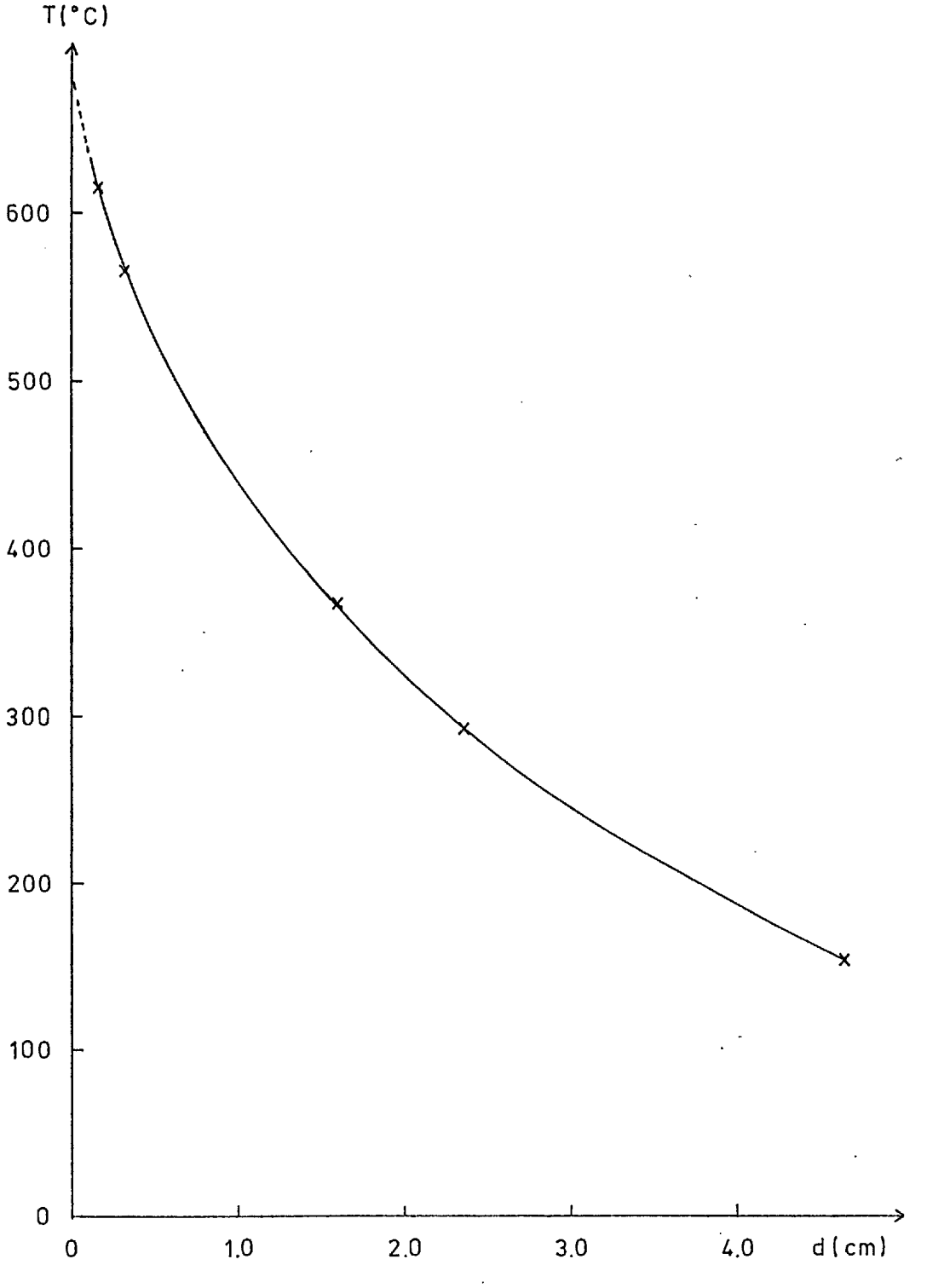


Fig. 8. Downstream gas temperature of the plasma.

and thus capable of causing greater heat losses from the neutral gas. The temperature in the centre of the discharge was therefore probably between 700 and 750 °C.

The low temperature of the neutral gas compared with that of the electrons can be explained by the manner in which each particle derives its energy. Charged particles i.e. ions and electrons are directly accelerated by the applied microwave field whereas the neutral gas atoms are unaffected. The neutral gas atoms must therefore gain energy by collisional exchange with the ions and electrons. Consider the situation depicted in Fig. 9 where an electron of mass m and initial velocity v collides with an atom of mass M and initial velocity zero. An elastic collision results in the particles moving off in the directions shown with changed velocities v' and V. Now from the law of conservation of energy

$$\tfrac{1}{2}mv^2 = \tfrac{1}{2}mv'^2 + \tfrac{1}{2}MV^2$$

and from the law of conservation of linear momentum

$$mv = mv' \cos\theta + MV \cos\beta \qquad \text{(x direction)}$$

$$0 = mv' \sin\theta + MV \sin\beta \qquad \text{(y direction)}$$

Eliminating V and β and rearranging shows that the fractional change in velocity of the electron Δv is given by

$$\frac{\Delta v}{V} = -\frac{m}{M}(1 - \cos\theta) \qquad \text{....2.24.}$$

and since energy is proportional to v^2 and $\Delta(v^2) = 2v\Delta V$, the fraction of energy lost by the incident electron is

$$\frac{\Delta E}{E} = \frac{2m}{M}(1 - \cos\theta) \qquad \text{....2.25.}$$

This equation shows that the transfer of energy from the electrons to the neutral gas is extremely inefficient and that electrons can go on gaining energy from the field, without causing much heating of the

neutral gas. The ions however have masses almost identical to that of the neutral gas atoms and therefore impart a large proportion (up to one half) of their energy to the neutral atoms upon collision. The net result is heating of the neutral gas and depression of the ion temperature. Large temperature differences between the various plasma particles is indicative of a low degree of ionisation of the carrier gas.

The low temperature of the plasma gas is a serious drawback when the plasma is used as a source for emission spectrometry. The number of compounds that can be atomised efficiently by a gas at 700 ^{o}C is rather limited and for this reason it is usual to introduce foreign species into the plasma in the vapour state.

2.6. THE EFFECT OF ADDING NITROGEN TO THE PLASMA.

The spectral plot shown in Fig. I indicated that trace impurities of nitrogen and water were present in the argon gas. Nitrogen is an interesting gas spectroscopically because it has a large number of band emissions, corresponding to a wide range of photon energies and the structure of the molecule makes it an efficient quencher. Experiments were therefore carried out to determine which nitrogen bands could be excited by the plasma and how much nitrogen was required to quench the discharge.

Quenching was found to occur when the level of nitrogen reached 5% of the total flow. The mechanism of quenching by nitrogen is almost certainly collisional damping of the electron energies, by conversion of their kinetic energy into the internal energy of the nitrogen molecule. For the process to be favourable the energy discrepancy must be small and because nitrogen has many closely spaced energy levels available, the condition can be met for large numbers

of electrons. At low pressures (ca 5 torr) average electron energies are somewhat higher (the electrons suffer fewer collisions) and appreciable dissociation and ionisation of N_2 occurs so that the plasma may be run on pure nitrogen.

Fig. 10 shows a spectral plot of the plasma between 290 and 430 nm when run on 250 ml.min^{-1}. Ar plus 10 ml.min^{-1}. N_2 at 65 W input power. The principle emissions are identified showing that the nitrogen is readily excited by the free electrons and will therefore damp their energy distribution. Three nitrogen band systems appear, the N_2 Second Positive $C^3\pi$ - $B^3\pi$, NH $A^3\pi$ - $X^3\Sigma$ and N_2^+ First Negative $B^2\Sigma_u^+$ - $X^2\Sigma_g^+$. It is interesting to note that the $C^3\pi$ level of the nitrogen second positive is about 11.1 eV above the ground state, which would correspond to a resonance photon of 113 nm (which is far into the vacuum ultra-violet region of the spectrum). Provided then, that substances can be introduced into the plasma in suitable form, there appears to be sufficient numbers of high energy species available to excite a wide range of spectral transitions. The word species is used because argon has two meta-stable levels at 11.49 and 11.66 eV, and it is to be expected that meta-stable atoms having lifetimes longer than that of a normal excited state will also be active in the excitation process. Observations on supersonic argon plasmas doped with N_2 (76) have shown that radiation can persist in field free regions for unexpectedly long periods. The appearance of N_2 Second Positive bands and the lack of bands from levels above 11.66 eV was taken as proof that excitation was occurring by collisional energy exchange with meta-stable atoms. Further consideration will be given to the importance of meta-stable levels in the discussion on plasma mechanism.

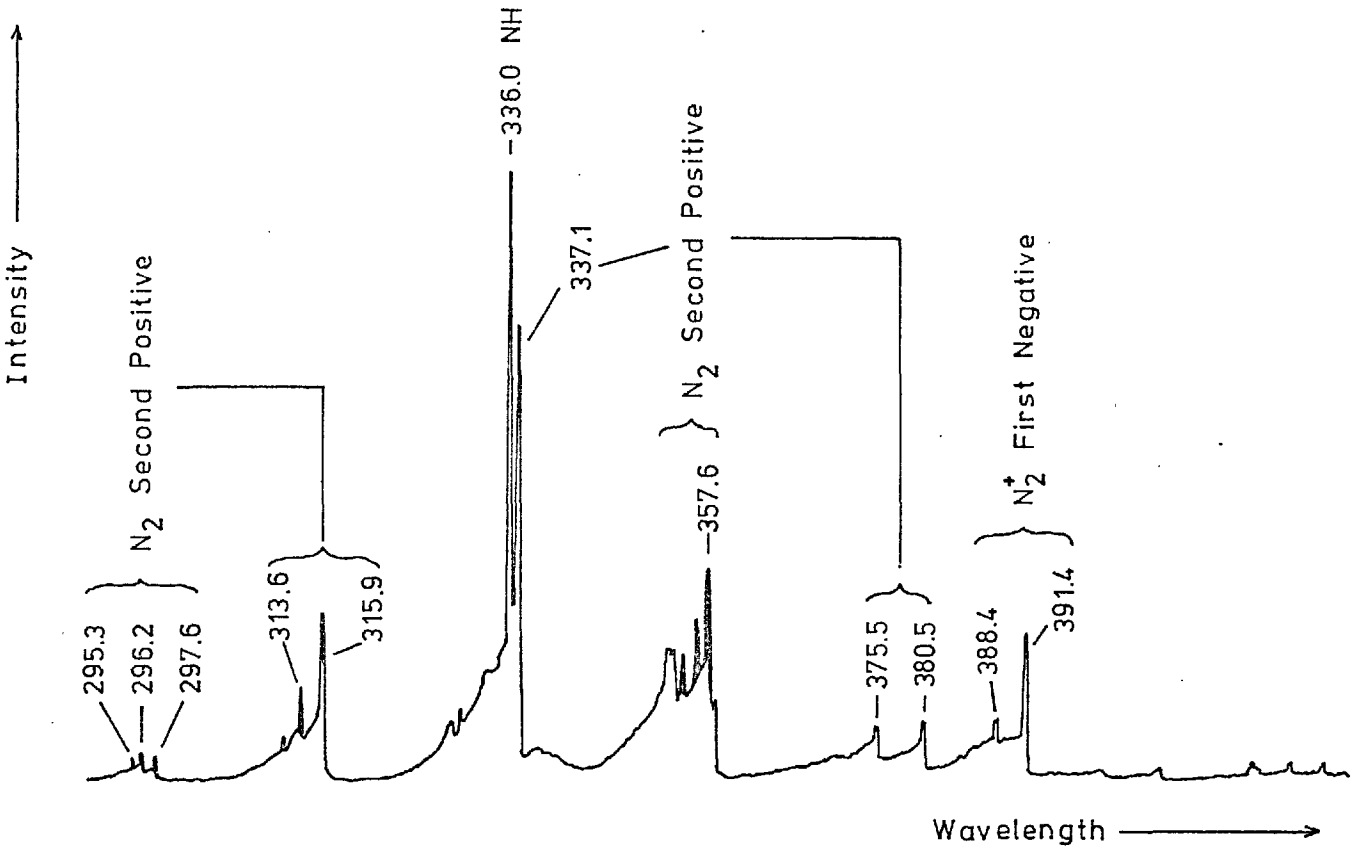


Fig.10. Argon plasma spectrum with 5% nitrogen.

2.7. EQUILIBRIUM OF THE PLASMA.

2.7.1. Theory.

The most important fact that must be established about any gaseous system is whether or not that system conforms to a defined equilibrium. For non-equilibrium systems, the ability to completely describe the microscopic processes by a few bulk parameters such as temperatures and particle density is lost. Temperature may still have significance because it is a parameter of the distribution function of particle velocities (nearly always Maxwellian), however it cannot be employed to calculate spectroscopic properties using equation such as Boltzmann and Saha. Alternatively, for a system in complete thermodynamic equilibrium all particles are characterised by a Maxwellian distribution of velocities corresponding to some temperature T, the distribution between various stages of ionisation is given by the Saha equation and the distribution within the bound levels of any stage obey Boltzmann statistics. In the absence of complete thermodynamic equilibrium the concept of LTE (see section 2.1) can be invoked, where it is assumed that the distribution of states is dominated by collisional processes to the exclusion of radiative processes, which are then associated with insignificant energy exchange and losses.

When considering the criteria that must apply for a system to be in LTE it is necessary to consider the excited states and ground state separately. For a given excited level n to be in collisional equilibrium with respect to higher levels, its total transition probability for radiational decay must be considerably less than its rate of collisional excitation to higher levels. This condition is particularly stringent for lower levels because transition probabilities

for radiative decay are inversely proportional to the quantum number of the state ($A \propto 1/n^{9/2}$ for hydrogenic states), and collisional cross sections are small. Griem (51) has calculated that for the relative population of a given state to be within 10% of LTE with respect to higher levels, the collisional population rate should be ten times the radiational population rate and that this pertains if

$$n_e \gg 7.10^{18} \frac{Z^7}{n^{17/2}} \left(\frac{kT_e}{Z^2 E_i} \right)^{\frac{1}{2}} \quad cm^{-3} \qquad \ldots.2.26.$$

where Z is the charge on the ion

n is the principal quantum number of the level n

and the other symbols have the same meanings as before.

The condition that the ground state is in LTE with the first excited state is the most stringent because radiative decay rates can be extremely high and thus when LTE does pertain to the ground state it can be safely assumed that complete LTE exists between all other levels. The ground state is in LTE with respect to higher levels when its radiative population rate is negligible compared with its collisional population rate, which in a sense is opposite to the condition for LTE of the excited levels. The following criterion has been calculated:

$$n_e \gg 9.10^{17} \left(\frac{E_u}{E_i} \right)^3 \left(\frac{kT_e}{E_i} \right)^{\frac{1}{2}} \quad cm^{-3} \qquad \ldots.2.27.$$

This relation is rarely satisfied in practice, however the ground state can still approach an LTE population because the effective radiational population rate is reduced by the occurrence of self-absorption. The condition in equation 2.27 can often therefore be relaxed by a factor of 10.

2.7.2. Experimental Evidence.

During the period that the results presented in the first part

of this chapter were being obtained, plasma parameters were also the subject of study of two other workers namely Winefordner (77) and Vickers (78) whose results have recently been published. Vickers reports studies on low pressure argon and helium plasmas run at various powers in a $\frac{3}{4}$ wave tapered waveguide and Winefordner reports studies on a free flowing, atmospheric pressure argon plasma run at 100 W in a similar cavity. Since the purpose of this chapter is to investigate the plasma mechanism, for which parameter determination is merely a means, the results of these workers will also be taken into account.

Assuming that the plasma is in LTE the electron density can be calculated from the Saha equation (2.18). Taking the number density at 700 °C to be $7.55.10^{18}$ cm^{-3}, the mass of the argon atom as $6.68.10^{-23}$ g, the Baltzmann constant as $1.38.10^{-16}$ ergs K^{-1}, the ionisation potential as 15.76 eV and approximating the partition functions to the statistical weights of the relevant ground states i.e. $Q(T) = 2.0 + 1 = 1$ and $Q_i(T) = 2(1 + \frac{1}{2}) + 1 = 4$, the electron density can be calculated if the temperature is known. Winefordner, using the relative line intensity method obtained an excitation temperature of 4920 ± 400 °K and from measurement of the absolute intensity of the 425.9 nm argon line an excitation temperature of 6560 ± 500 °K. Furthermore by measuring the relative radiances of the 407.7 nm Sr (II) and 460.7 nm Sr (I) line and the 396.8 nm Ca (II) and 422.7 nm Ca (I) line temperatures of 5050 and 4980 °K were obtained. The average of these results 5400 ± 500 °K which is in good agreement with the excitation temperature of 5680 °K. Using this value, the electron density from Saha is ($n_e = N^1$)

$$n_e = 1.2.10^{16} \text{ cm}^{-3}.$$

however allowing for a temperature error of 480 °K the electron density could be reduced to $2.4.10^{15}$. In the Winefordner paper an independent estimate of the electron density was made, by measuring the Stark broadening of the hydrogen H -β line (no interferometer was available for this measurement to be made in the work reported here). The hydrogen is present in the plasma from the dissociation of water vapour which is present as an impurity in the argon. The electron density obtained was

$$n_e = 1.8.10^{15} \text{ cm}^{-3} \qquad \text{(no error quoted)}$$

Substituting appropriate values into equation 2.26 i.e. T = 5680 °K and considering levels of principal quantum number 4 and higher the criterion for LTE is that

$$n_e \doteqdot 10^{13} \text{ cm}^{-3}$$

Therefore it can be assumed that the excited levels of the argon are in LTE having a Boltzmann distribution of states corresponding to an electron temperature of 5680 ± 480 °K. The straight line of the log $(I\lambda/g_uA)$ versus E_u plots indicates a Boltzmann population but is not in itself a sufficient criterion for LTE. The condition that the ground state is in LTE with the first excited state (the 4^3P_1, state at 11.56 eV) is given by substituting values into equation 2.27.

$$\text{i.e. } n_e \gg 1.2.10^{17} \text{ cm}^{-3}$$

However it has been shown that in argon self-absorption is such (51, 70) that this condition may be relaxed by a factor of 10. Because there is a substantial uncertainty in the electron density, it is probably best to assume that the ground state is not purely collision populated, but approaches a coronal equilibrium (51) being jointly populated by collisional and radiational processes.

The random errors associated with each of the temperature

measurement techniques are not large enough to explain the difference in the values obtained especially taking into account the results of the line to continuum method. It is therefore necessary to consider whether all the relevant factors have been accounted for.

2.8. PLASMA MECHANISM.

2.8.1. The Ionisation Recombination Equilibrium.

There exists in argon plasmas an ionisation recombination equilibrium characterised by the equations

$$Ar + e^{*} \longrightarrow Ar^{+} + e + e \qquad ....2.28.$$

$$Ar^{+} + e \longrightarrow Ar + h\nu \qquad ....2.29.$$

$$Ar^{+} + e + e \longrightarrow Ar + e \qquad ....2.30.$$

Now because the electron density is low radiative recombination is likely to dominate over three body recombination so that the equilibrium is described mainly by equations 2.28 and 2.29. It has therefore been suggested (79, 80) that this equilibrium gives rise to two distinct groups of electrons, a high energy low density group (characterised by *) and a low energy high density group. Each group is assumed to have a Maxwellian distribution of velocities characterised by a different temperature. Because the double probe method samples only those electrons with energies above eV_f, it is mainly the high energy group whose temperature is estimated. The equilibrium then is a balance between the ionisation rate produced by the high energy electrons and the rate of electron and ion removal by diffusion to the walls (both free and ambipolar diffusion (81)) and radiative recombination. Kenty (82) has shown that radiative recombination cross sections decrease with increase of energy and therefore whilst it will be primarily high energy electrons that are lost by diffusion, the low energy group will be depleted mainly by recombination.

It appears therefore that the bound states are in collisional equilibrium with the high density low energy group of electrons and that this equilibrium extends down from the continuum to the first excited state. This lower level is generally known as the thermal limit because it represents the lowest state in equilibrium with the free electron, thermal distribution. Levels below the thermal limit (i.e. the ground state) have a population which is approximately coronal, being determined by a combination of collisional and radiational processes. Meta-stable states are no exception to the LTE assumption because their long lifetimes ensure that their populations are always collision controlled. Clearly then, the spectroscopic properties of the plasma are dominated by the low energy group of electrons, but some interference from the high energy group is inevitable. This may account for the variance in the temperatures obtained by the different methods although there is no apparent reason why the line to continuum method should include a large contribution from the high energy group.

2.8.2. The Ionisation Process.

Before ionisation breakdown can occur in the plasma, the presence of a few free electrons is required (in the absence of extensive field ionisation) which are supplied by means of a Tesla coil. Now consider the experience of a single free electron initially having zero energy. The electron is accelerated by the field for a short period until either the field changes direction or the electron collides with an atom. The collision changes the direction of the electron but does not seriously alter its speed, the energy exchange occurring in proportion to $2m/M$ (see equation 2.25). This process continues with the electron gaining energy in steps, from the field and losing energy by elastic collisions. When the electron attains an energy slightly

above that of the first excited state, there is a finite probability that an inelastic collision will occur, the electron losing nearly all its energy which unless the state is meta-stable will be radiated away by emission of a photon. Provided that the electric field is high enough, a few of the electrons will reach the ionisation potential without suffering inelastic collisions and thus produce further ionisation.

These arguments are general and may apply equally well to a d.c. or an a.c. field. It is therefore necessary to consider the effect that the frequency of the field has on the ionisation process. An electron accelerated by the field will move off in a particular direction and since both voltage and electron current are initially in phase, will present a resistive load to the generator. The energy exchange between the field and the electron then approaches one hundred per cent efficiency. Now when the field changes direction, the force on the electron changes direction, but its direction of motion does not change abruptly (assuming no collisions occur) so that a phase lag develops between voltage and current, and the load presented to the generator becomes partially reactive. The electron decelctates and loses energy which it passes back to the field so that the electron does work on the generator. After a few cycles a steady phase lag develops and for a voltage represented by

$$e = E \sin \omega t$$

and a current by $i = I \sin (\omega t + \phi)$

where e is the instantaneous voltage,

E is the peak voltage,

i is the instantaneous current,

I is the peak current,

ω is the angular frequency of the field,

t is the time and

ϕ is the angular phase lag.

The average power per cycle transferred to the electrons by the generator is given by

$$P = V_{rms} I_{rms} \cos\phi$$

Now the value of ϕ depends both on the frequency of the applied field and on the electron collision frequency because electron atom collisions interrupt the out of phase motion and therefore promote efficient energy exchange between the electrons and the field. At low pressures the phase lag approaches 90° and energy exchange becomes very inefficient because the work done by the field on the electrons during half the cycle, is returned to the field by the electrons during the second half of the cycle. Alternatively at high pressures the high collision rate reduces the phase lag to near zero causing the electrons to receive the maximum acceleration from the field. From these arguments it would appear that maximum electron energies occur at high pressures but this is not the case because collisional energy damping becomes increasingly important. For example, it has been found (81) that in Ar at 992 M.Hz. the optimum pressure for breakdown is 1 torr.

The effective field that the electrons experience is therefore a function of the applied frequency and the collision frequency and it has been shown (81) that it can be expressed in the form

$$E_e^2 = E^2 \frac{\nu_c^2}{\nu_c^2 + \omega^2} \qquad \ldots.2.31$$

where E_e is the effective field

E is the true field

and ν_c is the collision frequency

The collision frequency can be calculated from the kinetic theory (81) and is given by the relation

$$\nu_c = 2.1.10^8 \, u^{\frac{1}{2}} \, pQ \qquad \ldots.2.32$$

where u is the electron energy in volts

p is the gas pressure in torr

and Q is the collision cross section in angstroms squared

Argon has the unusual property that the collision cross section is energy dependent, indeed at about 0.4 eV argon is almost transparent to electrons (the Ramsauer Effect) so that an electron gaining energy from the field can pass easily through the 0.4 eV region (provided phase lag is not excessive) and move on to higher energies. However between 1 and 12 eV the collision cross section rises rapidly with the result that collisional damping is increased. Above 12 eV the collision cross section gradually decreases, although above the appropriate threshold energy cross sections for excitation and ionisation increase steeply. The temperature of 5680° K corresponds to an electron energy of kT (the electron only has two degrees of freedom in a bi-directional field) equals 0.49 eV. Vickers (78) obtained a temperature of 4535° K at 25 torr and 100 W corresponding to an electron energy of 0.39 eV. The surprising ubiquity of the 0.35 to 0.55 eV energy range in argon is undoubtedly related to the unusual energy dependence of the collision cross section.

Taking the temperature of the high energy group of electrons, which are responsible for ionisation, to be that determined by the double probe method yields an electron energy of 2.1 eV. Using the data from MacDonald (81), the collision cross section for electrons at 2.1 eV in argon is approximately $4.0.10^{-16}$ cm^2 and substituting the appropriate values into equation 2.32 yields a collision frequency

of $9.3.10^{11}$ sec.$^{-1}$. Comparing this with the frequency of the applied field i.e. $2.45.10^{9}$ sec.$^{-1}$ indicates that 378 collisions occur per cycle of the field. Substituting into equation 2.31 shows that the effective field is 0.9997 of the actual field, which is to be expected in view of the large number of collisions. One other important parameter that can now be determined directly is the electron mean free path L given by the relation (81) :-

$$L = \frac{1}{p.2.82.10^{-17}.Q} \quad \text{cm}$$

which yields a value of $9.3.10^{-5}$ cm for the high energy group. This value indicates that electrons cannot be swept out of the bulk plasma by the field and that the principal loss will occur by diffusion. Furthermore, the high frequency of the microwave field means that the electron does not travel far in one half-cycle of acceleration.

Finally using the data obtained it is possible to gain an indication of the minimum electric field strength (within an order of magnitude) required for breakdown to occur. The classical random walk problem indicates that the mean square of the distance travelled in N collisions is given by $2L^2 N/3$ and setting this equal to the square of the distance that an electron must travel to diffuse out of the plasma (say a radius) will yield the number of collisions en route. Now in order to maintain the ionisation equilibrium such an electron must reach the ionisation potential before being lost, so that setting the energy gained between collisions equal to ΔE the following relation must hold

$$E_i = N' \Delta E$$

where N' is the average number of collisions before being lost

and E_i is the ionisation potential

The average change in the square of the electron velocity between

collisions is

$$(\Delta V)^2 = \left(\frac{E_e e}{m}\right)^2 . \quad (\Delta t)^2$$

where e is the charge on the electron

m is the mass of the electron

Δt is the average time between collisions

and thus the average energy gain between collisions is

$$\Delta E = \frac{1}{2m} E_e^2 e^2 (\Delta t)^2$$

Now $$(\Delta t)^2 = \frac{2}{\nu_c^2}$$

and thus $$\Delta E = \frac{E_e^2 e^2}{\nu_c^2 m}$$

Therefore the effective field strength is given by

$$E_e = \frac{\nu_c}{e} \sqrt{\frac{E_i m}{N'}} \qquad ....2.33.$$

Taking the radius of the plasma to be 5.10^{-4} m and calculating N' to be $4.34.10^5$, equation 2.33 yields an effective field of

$$E_e = 4.23.10^5 \text{ volts } m^{-1}$$

This seems a high value but is in reasonable agreement with the results of studies specifically aimed at determining breakdown fields (81).

2.8.3. Penning Ionisation.

The existence of meta-stable states in the carrier gas can lower the effective ionisation potential, when impurity atoms having ionisation potentials below the meta-stable level, are present. The process is represented by the equation

$$Ar_{meta} + M \longrightarrow M^+ + Ar + e \qquad ....2.34.$$

where M is an impurity atom.

The energy difference between the meta-stable level and the ionisation potential of the foreign species is carried off by the ejected electron (83). Meta-stable levels have long lifetimes of the order of milliseconds during which period thousands of collisions may occur. If there should be only one impurity atom per thousand argon atoms the process represented in equation 2.34 is still highly probable. Mercury (E_i = 10.4 eV) in particular has been employed in breakdown studies in rare gases, to lower the effective ionisation potential.

One other mechanism has been suggested for meta-stable ionisation viz. (84) :

$$Ar_{meta} + A_{meta} \longrightarrow Ar^{+} + e + Ar$$

although the probability of this collision occurring must be very low.

2.8.4. Ionisation of Impurities.

The presence of elements in the plasma having ionisation potentials below that of argon contribute to the total electron density. For example, the spectral plots of the plasma indicate that water dissociates into H and OH and it can be shown that partial dissociation of OH also occurs (77). The ionisation potential of O is 13.62 eV and that of H 13.60 eV and thus both these elements will be ionised to an appreciable degree.

2.8.5. The Excitation Mechanism.

The existence of a quasi-LTE equilibrium in the plasma has already been established, but it will be useful to conclude this chapter with a brief consideration of the microscopic mechanisms of the excitation process.

The populations of the lowest energy levels reflect a balance between collisional excitation and de-excitation and radiative de-excitation (emission) and excitation (self-absorption). These

processes may be represented thus

$$Ar + e \rightleftharpoons Ar^* + e \qquad \text{collisional equilibrium}$$

$$Ar^* \rightleftharpoons Ar + h\nu \qquad \text{radiative equilibrium}$$

However, the situation for the highly excited states is somewhat different. Radiative excitation and de-excitation cross sections are small but cross sections for collisional excitation and de-excitation and radiative recombination are high. The following mechanisms are therefore likely to be of importance

$$Ar + e \rightleftharpoons Ar^* + e$$

$$Ar^+ + e \rightarrow Ar^* + h\nu$$

In other words, radiative recombination may be a mechanism for the population of excited states, but the electron concentration is probably sufficient to re-distribute the captured electrons according to a thermal distribution i.e. a Boltzmann distribution.

2.8.6. The Excitation of Foreign Species.

The excitation of foreign species in the plasma may be viewed in a similar fashion to the excitation of Ar. Differences arise however, because many elements have ionisation potentials below that of argon and are therefore likely to be extensively ionised, both by the Penning mechanism and direct electron impact. Under these conditions radiative recombination of the low energy electron group may assume a greater importance in populating the excited states of the foreign atoms. Vickers (78) postulates that for low pressure microwave plasmas, radiative recombination is the major mechanism for the excitation of foreign species however the evidence presented is not conclusive.

Excitation by meta-stable atoms has already been mentioned (see section 2.6), but the mechanism is not as general as direct electron excitation because two conditions apply. One, the process is most

favoured when the energy difference between the meta-stable level and the relevant excitation potential is small (4); and two, the total spin of the colliding partners must equal the spin of the resulting particles (the Wigner Spin Conversion Rule (4)).

oooOOOooo

CHAPTER III

A MICROWAVE-EXCITED, ATMOSPHERIC PRESSURE, ARGON PLASMA SUITABLE FOR TRACE ANALYSIS BY ATOMIC EMISSION SPECTROMETRY

3.1. INTRODUCTION

The technique of atomic emission spectrometry has in recent years been overshadowed by the rapid growth in the use of AA and AF. This growth has resulted directly from the improved sensitivity and selectivity that AA and AF offer for a wide range of elements, when analysed using flame systems. The universal acceptance of the flame as the preferred atom reservoir has limited AE as the most sensitive technique, to those elements having major resonance lines above ca. 350 nm e.g. Na, K, Ca, Sr, Al and In.

Atomic emission has the advantage that it requires no auxilliary source of excitation, and therefore the instrumentation tends to be considerably simpler and cheaper than that used for AA and AF. Furthermore the fact that the excitation source is non-specific, enables AE to be used for multi-element analysis even on an unknown matrix. The techniques of AA and AF which do employ specific excitation sources have advantages in spectral selectivity, but in part this is counteracted by the greater number of spectral lines that can be used for AE compared with AA and AF (both are restricted mainly to resonance lines). Certainly then, provided that a sufficiently energetic source of excitation e.g. a plasma is available, AE is an extremely versatile method of analysis.

A number of electrical sources have been used for emission spectrometry (see section 1.3.), however those that appear to have the greatest potential for trace analysis are the electrodeless discharges. The absence of electrodes in the exciting plasma minimises both interferences and problems of sample introduction.

Recently high powered RF electrodeless plasmas have received extensive study both theoretically and in the analytical context.

Johnston (70) reports comprehensive spectroscopic studies on an RF, atmospheric pressure, free flowing, argon plasma run at 6 KW and 4.5 M Hz. From temperature and electron density measurements it was concluded that the plasma closely approximated to an L.T.E. fluid, having a Boltzmann population of states corresponding to a temperature of ca. 10000 °K. The existence of L.T.E. in the plasma enabled it to be used for the measurement of argon atomic transition probabilities.

The high temperature and running stability of such plasmas has caused a number of workers (85,86) to investigate them for analytical purposes. Detection limits of 10 p.p.m. Cu, 5 p.p.m. Ni and 10 p.p.m. Mn have been reported (85) for samples introduced as aqueous aerosals. Greenfield and Dagnall et. al. (86) have used an RF (36 MHz at 2.5 KW) plasma run on Ar-N_2 mixtures for the atomic emission determination of elements such as boron and beryllium, introduced directly as a fine powdered sample. The powder was formed into a fluidised bed by electro-mechanical vibration and then blown into the plasma by the gas flow. Once the sampling device had been loaded with about 3.5 g of sample, the emission signal decreased exponentially with time. This meant that in the absence of an integral technique of signal measurement, timed observations had to be made. A number of matrixes were investigated e.g. $CaCO_3$, SiO_2, Al_2O_3 and MgO, but only MgO was found capable of producing both a non-coagulating powder cloud and a sufficiently low background emission. Detection limits of 0.1 p.p.m. Be and 2.5 p.p.m. B were reported for the MgO matrix. The ability of the plasma to produce free atoms from samples of this nature, illustrates the enormous energy available in this type of source. Drawbacks of the system included the high cost of the equipment, an intense and sometimes noisy background spectrum and

excessive ionisation for elements having low ionisation potentials.

In 1965 Cooke et. al. (36) proposed the use of low wattage (less than 100 watts) microwave excited plasmas for the spectral identification of species eluted from a gas chromatograph. The system composed a low pressure free flowing plasma which was initially used to detect the presence of hetero atoms such as nitrogen, chlorine, fluorine, sulphur and others. By monitoring the emission of atomic carbon (247.86 nm) and carbon containing species such as CN, the device served as a general G.L.C. detector. Cooke estimated the limit of detection for carbon to be 10^{-16} g. Later Lisk and Bache (87 - 89) employed the technique for the identification of halogen and phosphorus residues from insecticides.

Recently Runnels and Gibson (49) showed that plasmas of this type could be used for the determination of metals. In their system volatile organometallic species, dissolved in organic solvents, were deposited on a platinum loop with a microlitre syringe. First the solvent was evaporated, the loop was then placed inside the plasma cell and the compound vapourised into the plasma by electrical heating of the loop. The plasma in this case was a free flowing, atmospheric pressure system, run at 25 watts in a $\frac{1}{4}$ wave resonant cavity. Typical detection limits were in the range 10^{-11} to 10^{-12} g for elements such as silver, iron and copper.

The previous work (36, 49,chapter 2) has shown that microwave excited argon plasmas contain a sufficient number of high energy electrons to strongly excite the spectral lines of most elements. For routine analytical application the system must be capable of handling samples in different compound forms and therefore in the work reported here, the solutions used were made up from inorganic salts

such as the sulphates, chlorides, oxides etc. and no attempt was made to choose the most volatile species. It has been shown (36, 49, chapter 2) that excessive amounts of any species will extinguish the plasma, thus methods such as the platinum loop vapouriser (90) and G.L.C. elution which remove the solvent first and do not require the plasma to supply the vapourisation energy to the sample, are preferable. The system described here employed platinum or tungsten loops for both sampling and vapourisation of the analyte compound.

Early workers experienced difficulties caused by plating out of the sample on the walls of the containing quartz tube (usually 2 mm internal diameter). To avoid this difficulty conditions were established under which the plasma could be operated almost entirely in free air like a flame.

3.2. THE EXPERIMENTAL SYSTEM

The microwave induced argon plasma system is depicted in Fig. 11. Microwave energy at 2450 ± 25MHz was derived from a 'Microtron 200' microwave generator (Electro-Medical Supplies, Wantage, England) and coupling was via an Evenson (44) type $\frac{1}{4}$ wave resonant cavity (E.M.S. type 214L). The radiation emitted from the plasma was analysed with a Unicam SP.900 spectrophotometer fitted with an E.M.I. 9601B photomultiplier. The internal chopper, a.c. amplifier and read out normally incorporated in the instrument were by-passed in favour of a d.c. amplifier/integrator.

3.2.1. The d.c. Amplifier/Integrator.

Weak and transient light signals such as those described here cannot be adequately recorded by the a.c. detection electronics common to most commercial spectrophotometers. A 50 Hz chopper as fitted to the SP. 900 accepts and rejects light for alternate periods

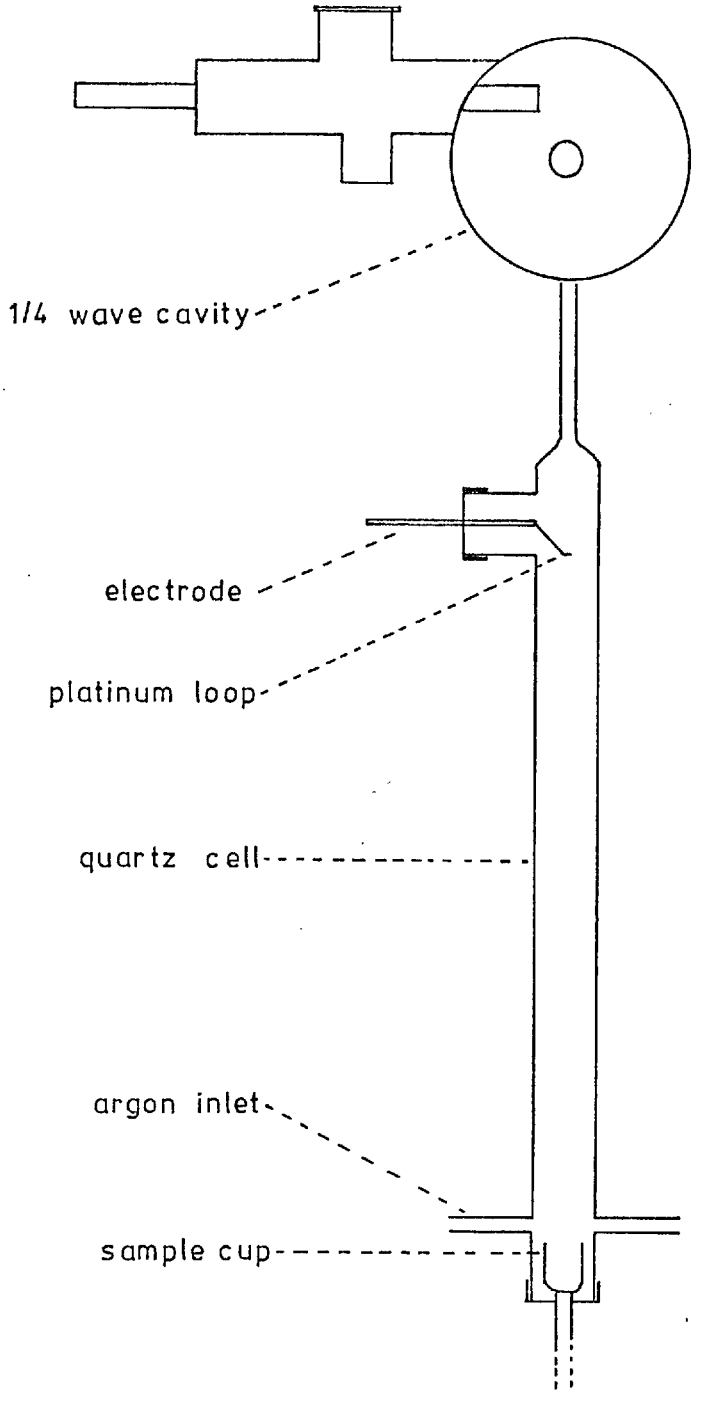


Fig.11. The microwave plasma cell.

of 10 m secs., so that a transient signal of similar duration could theoretically yield outputs ranging from zero to a nominally correct value. This disastrous effect on the analytical precision decreases with increase of signal duration or of chopper frequency. However, even when acceptable precision is obtained the use of a chopper causes 50% the signal information to be wasted. D.c. systems can provide an answer, but only if the response time of the circuitry is low (usually five times lower) compared with the half-life of the event, otherwise signal distortion (see chapter 4) resulting in poor precision and linearity of the analytical curve result. The situation is made worse when the signal duration is found to be concentration dependent, or the profile composed of a number of peaks. The work of L'Vov (23) has shown that the optimum method of handling transient signals of this type is by integration which largely removes measurement errors resulting from variations in the signal profile.

The circuit of the d.c. amplifier/integrator is shown in Fig. 12, power was supplied by a Coutant stabilised supply giving -15, 0 and +15 volts. Before use a warm-up time of about one hour was allowed after which operation proceeded as follows. The switch S1 was set in position 1 to allow voltage and current trimming of the first operational amplifier (OA1). With the output of the amplifier connected to a Servoscribe potentiometric recorder and the 5 K ohm potentiometer set to the earth end of its track, RV1 was adjusted to give 0V output (the optimum values of Rt_1 and Rt_2 for each operational amplifier are supplied by the manufacturer). S1 was then moved to position 2 and the output of the second operational amplifier trimmed to zero by adjusting the helipot RV2. At this point S1 could be moved to position 3 and the device operated as a d.c. amplifier with a gain of X100.

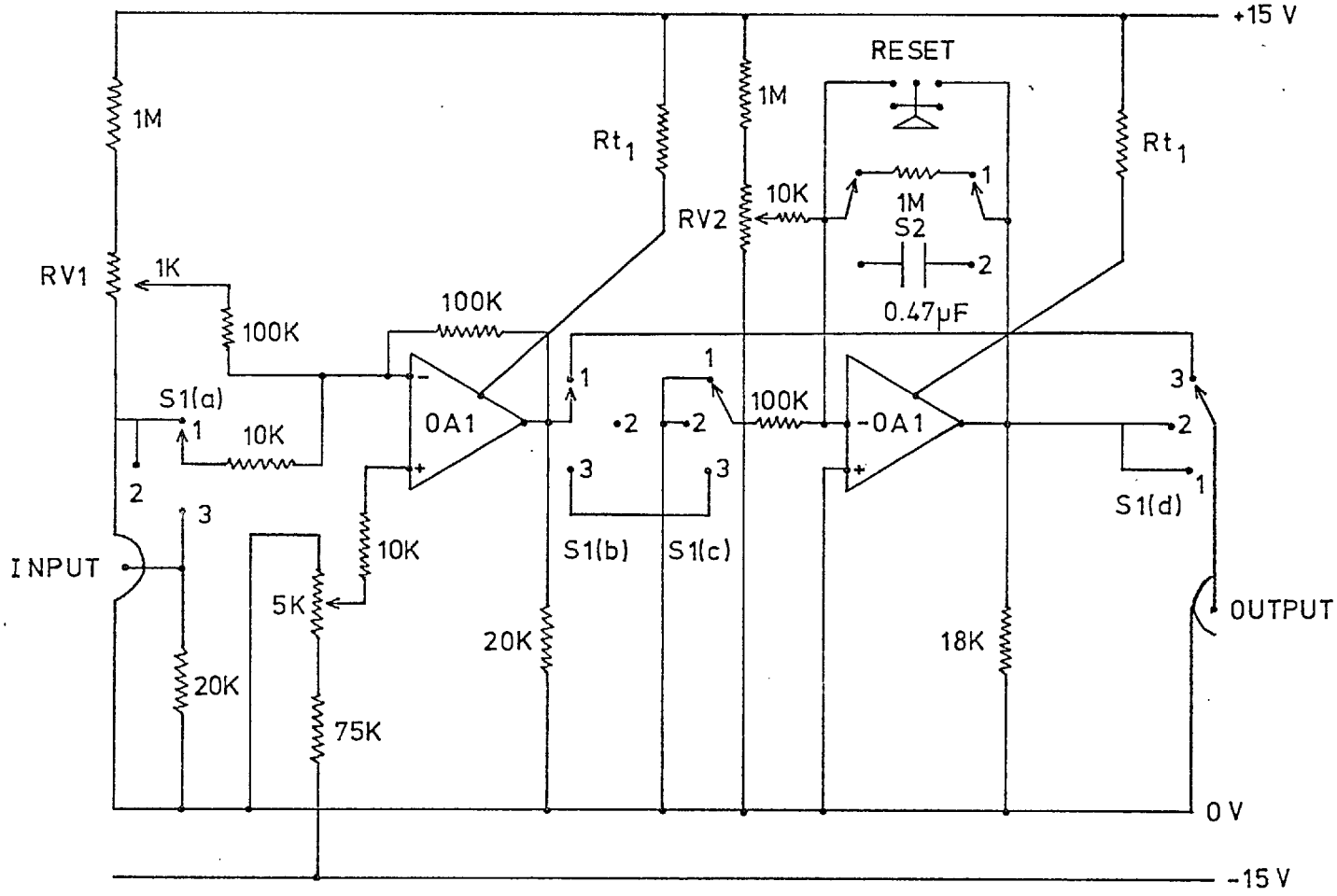


Fig.12. Circuit diagram of the d.c. amplifier/integrator.

With switch S2 in position 2, the unit integrated the input signal after a gain of 10 due to OA1. The capacitor in the feedback loop of OA2 charges at a rate proportional to the input voltage so that:-

$$E_{output} = -\frac{1}{RC}\int_{o}^{t} E_{in}\, dt \qquad \ldots\ 2.1.$$

Thus for a 10V output, 50 mV would have to be applied to the input for 1 second. The output voltage can be reset by pressing the reset button which discharges the capacitor. Before each series of measurements the dark current from the photomultiplier and the background radiation signal had to be offset. This was achieved by operating the amplifier in the differential mode, i.e. with S1 in position 3 and S2 in position 1 and trimming the output to zero with the 5 K ohm potentiometer. A final adjustment was made with S2 in position 2, setting the integrated output to zero by finely adjusting RV2. The device then integrated only the transient signal.

The components used in this system were not expensive and it is proposed to construct a new amplifier/integrator using chopper stabilised operational amplifiers and precision potentiometers, which should lessen the need for constant re-trimming which was found necessary with this circuit.

3.2.2. The Plasma Cell.

The plasma cell was constructed in transparent quartz from a piece of 8 mm (internal diameter) tubing ca 10 cm in length with a jet fused into one end of it. The gas inlets were attached at the lower end and a third port just below the fused jet allowed the platinum or tungsten loops to be introduced via a P.V.C. plug. Dimensions were not found to be critical except in the case of the jet, which should be 2 mm internal diameter and sufficiently long (ca 15 mm) to give laminar flow at the orifice. If the jet was made too short the plasma

was unstable and difficult to ignite. It was not possible to make the jet diameter approach the diameter of the plasma (see below), because the gas velocity was then too great for the plasma to be ignited. Use of a 2 mm jet however, caused the plasma to wander somewhat and hence change its position relative to the spectrophotometer slit. Because of the different rates of diffusion of electrons and ions plasmas in general have a negative sheath and a positive core. It was hence possible to solve the problem of 'wander' by securing to the jet a 10 mm length of steel needle so that it was opposite the slit centre, parallel to it and protruding about 1 mm above the jet orifice. The lower end of the plasma was attracted to this needle, probably by the 'mirror charge effect', and the plasma was therefore held parallel to the slit. A pyrex sample cup (minimum capacity ca 20 micro litres) treated inside with Hopkin and Williams 'Repelcote' was sealed onto a greased glass rod mounted into the main tube via a rubber septum cap; this arrangement allowed the sample cup to be slid up and down so that the sample solution could be applied tothe loop. The 'Repelcote' prevented surface adsorption of the analyte onto the glass and caused the sample solution to have a flat meniscus which facilitated precise sampling. (It is desirable to immerse the loop to the same depth for each sample). The diameter of the cup should be small enough to allow gas to pass when it is in the raised position so that the plasma is not quenched. An alternative method of sampling is to place the solution on the loop with a syringe.

3.2.3. The Plasma.

The main body of the plasma was formed above the jet orifice so that the plating out and devitrification problems encountered when the plasma is operated within a quartz tube were eliminated. Under

the optimum experimental conditions (see below) a short section of the plasma (ca 2 mm) remained in the tube whilst a stable pencil some 20 mm in length and 1.0 mm diameter extended beyond the orifice. The plasma was formed by first tuning the cavity to minimum reflected power (with a reflected power meter) and then initiating with a 'Tesla' vacuum tester.

3.2.4. The Sampling Loops.

For most elements the loops were made from 10 mm lengths of 0.1 mm diameter platinum wire spot welded to 1 mm steel electrodes. The loops formed resembled an ellipse having a major axis of 0.86 mm and a minor axis of 0.62 mm.

It was found that such a loop when just immersed below the surface of an aqueous solution, picked up a sample of ca 0.12 micro litre volume in the form of a surface tension film with reproducible dimensions. The measurement was made by taking ten samples from a solution containing 1000 p.p.m. Cd, washing them into a 10 ml volumetric flask and analysing the resulting solution by atomic absorption spectrometry. Several loops were made and their sampling volumes were found to range between 0.1 and 0.15 micro litres.

The aqueous film was evaporated first by passing a current of about 0.1 amps d.c. through the loop; during this process the plasma became less stable and shorter in length. The current was then switched to 1.9 amps causing the compound remaining on the loop to vapo rise and pass into the plasma region. Tungsten loops made from 0.1 mm tungsten (m.p. 3380 ° C) wire were used when a higher volatilisation temperature than could be achieved with platinum (m.p. 1769 ° C) was required. Two difficulties arose when using tungsten, oxidation of the loop and oxide burn off readily occurred, and shock

heating of the argon by the loop caused some increase in plasma instability.

3.3. OPTIMISATION OF THE OPERATING CONDITIONS.

Solutions of cadmium sulphate were chosen for optimising the system, as salts of Cd are not usually difficult to vapourise and Cd has an intense resonance line at 228.8 nm.

3.3.1. Argon Flow Rate.

Gas flow rate was found to be the most critical factor influencing plasma stability and therefore a careful study of its effect was made. An oscilloscope with a storage facility was used to observe the signal profiles obtained when samples containing 10 p.p.m. Cd were vapourised into the plasma at varying gas flow rates. The calibrated time base on this instrument enabled the delay time (from switch on of the loop current to the beginning of the signal profile) and signal duration to be measured. With an argon flow rate of 3.0 - 2.1 $l.min^{-1}$ the plasma was unstable owing to turbulance in the gas jet. Fig.13A shows a typical signal profile under these conditions; the shape is assymetrical having an approximately linear growth and exponential decay. The turbulence of the plasma is reflected in the positive and negative fluctuations superimposed on the main profile. In this instance the delay time was 75 m sec and the signal duration 225 m sec.

The plasma was stable when the argon flow rate was between 2.1 and 1.6 $l.min^{-1}$ and was easy to initiate. The profile obtained (Fig. 13B) is smoother than before and slightly flattened at the bottom; the delay time was once again 75 m sec and the signal duration slightly longer at 250 m sec.

Below 1.6 l min^{-1} the plasma rapidly decreased in length and was

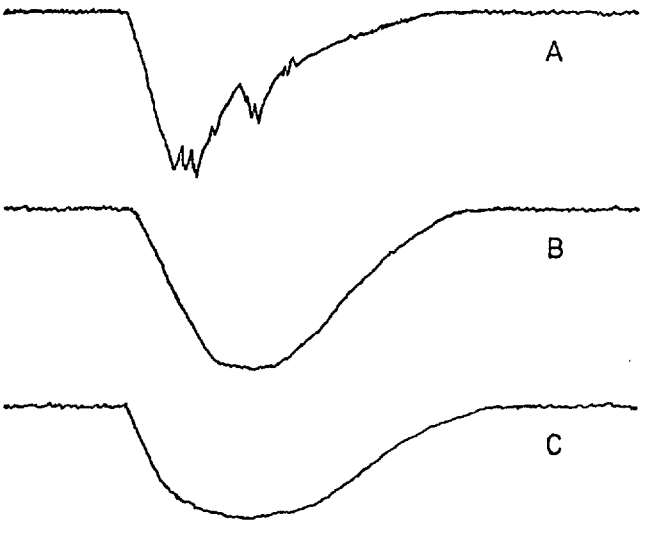


Fig.13. Transient signal profiles.

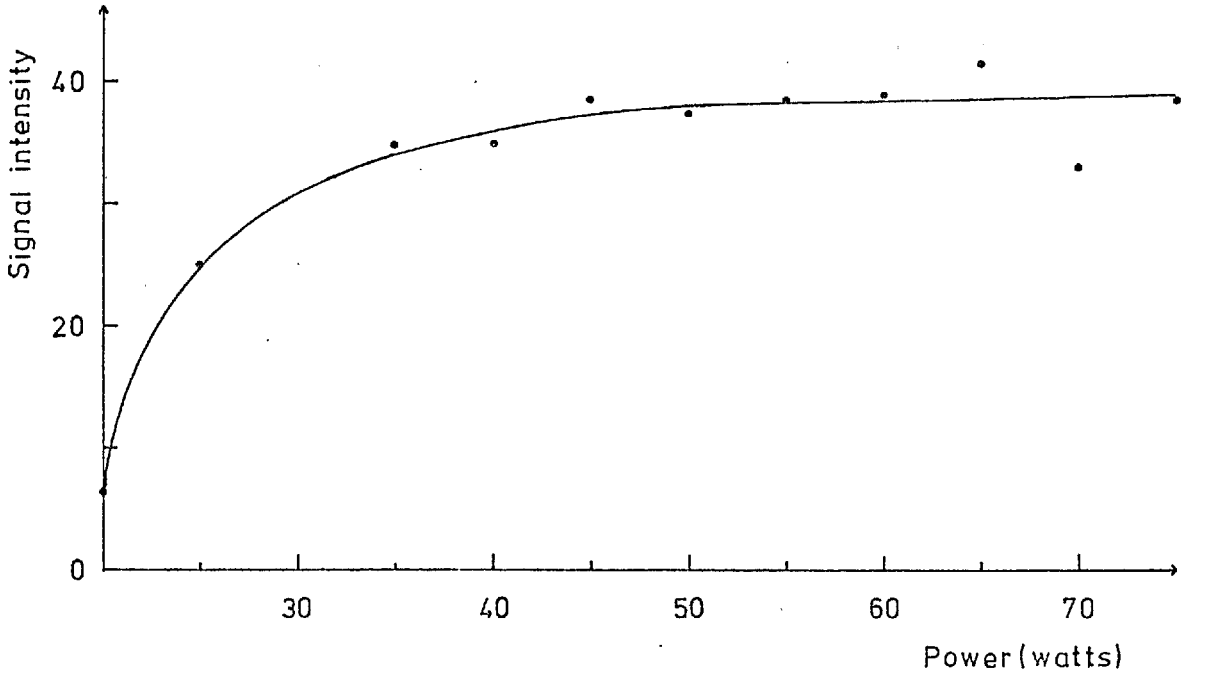


Fig.14. Signal versus power curve for cadmium.

finally quenched at ca 1.0 l min^{-1}. As stated before plasmas are sensitive to the introduction of molecular species and the rate of sample introduction must be kept low to avoid quenching. Under optimum conditions about 5 seconds were required to evaporate the water, but at these low flow rates considerable longer periods i.e. 10 - 20 seconds were necessary. The signal profile (Fig. 13C) once again had a 75 m sec delay time and 250 m sec duration although the shallowness of the profile indicates a slightly lower rate of sample introduction into the plasma. A flow rate of 1.85 l min^{-1} was chosen as optimum because it resulted in a stable plasma and a reproducible signal profile.

3.3.2. Microwave Power.

With the argon flow rate set at 1.85 l min^{-1} a plasma could be established at microwave powers ranging from 20 to 75 W. Samples containing 0.1 p.p.m. Cd were vaporised into the plasma at varying powers within this range and the resulting signals were recorded on a Servoscribe potentiometric recorder (Fig. 14). It was noted that the plasma increased in length with increasing microwave power; Fig. 15 is a plot of microwave power versus plasma length. The graph shows that at about 35 W the length of the plasma reached 20 mm which was then sufficient to fill the slit (20 mm long) of the Unicam SP 900. The steep rise in the power/signal curve was therefore attributed to the increase in plasma dimensions and not to an increase in the excitation temperature. The coupling of microwave power to the plasma was not 100% efficient and increasing the input power above the level required to give a stable plasma resulted in higher reflected powers (which tend to overheat the magnetron valve) and a slightly longer plasma, but no increase in the emission signal. The optimum microwave

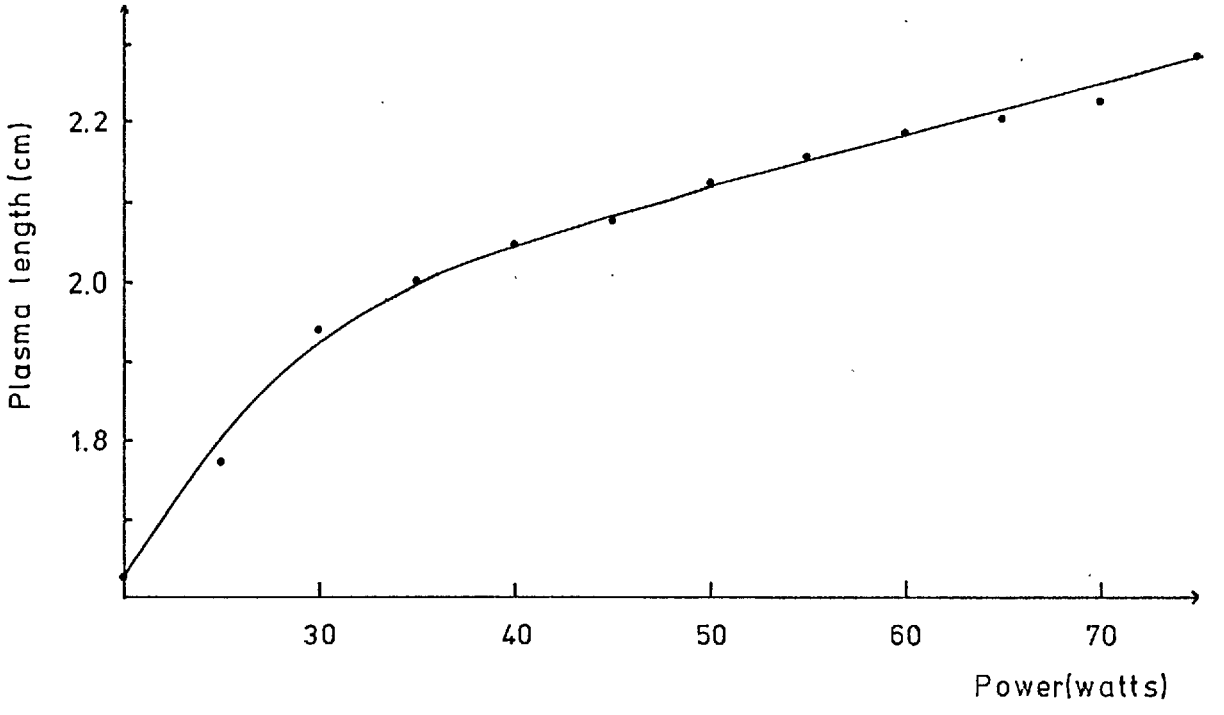


Fig. 15. Plasma length versus input power.

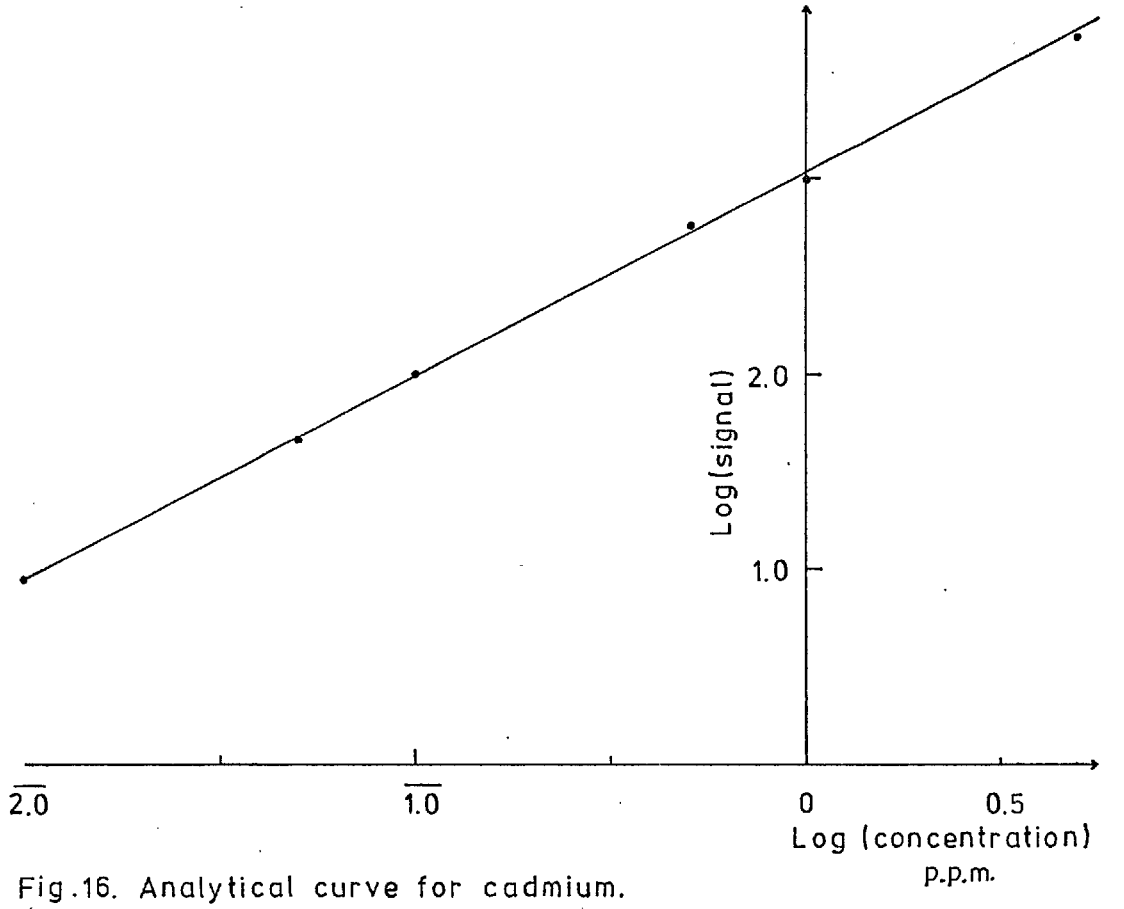


Fig. 16. Analytical curve for cadmium.

power was therefore selected as 45 W because it yielded a stable plasma and represented a point on the plateau of the power/signal curve.

3.3.3. The Occurrence of Intensity Antinodes in the Plasma.

The entrance slit of the monochromator was blocked except for a 2 mm square portion in the centre. The emission intensities of the argon background and of cadmium signals were then observed at different heights in the plasma. In each case it was found that a large maximum occurred opposite the central tuning electrode of the cavity, together with a much smaller one near the edge of the cavity approximately 9 mm below the first. It is thought that these maxima occur at positions where the electric field intensity within the cavity is greatest.

3.4. THE ANALYTICAL WORKING CURVE FOR CADMIUM.

Analytical grade chemicals and deionised water were used in the preparation of all solutions. The fundamental assumption of emission spectrometry is that the emission intensity is proportional to the number of atoms of the emitting species. This relation can be expressed in the form

$$I = K N^m \rho$$

where I is the emitted intensity

K is the constant

ρ is the excitation factor

N is the number of atoms of the emitter

m is the emission factor

Now taking logs yields

$$\log I = \log K\rho + m \log N$$

The emission factor m in the ideal case is equal to unity, but in the normal circumstances where background radiation, and self-absorption (50)

are present m varies to maintain the equality.

Ten samples at each concentration examined were vapourised into the plasma and the intensities recorded at 228.8 nm were averaged. The analytical working curve is shown in Fig. 16, the slope of the log/log plot is close to unity (1.046) and the curve is linear over the concentration range 0.01 - 5.00 p.p.m. These results show that at least for trace element analysis, the plasma yields a linear response free from serious background or self-absorption effects. It was not possible to study concentrations above 5.0 p.p.m. because the capacitor used in the integrator charged too slowly above this level. Curves constructed without using the integrator were not of a reproducible shape and were non-linear, the signal increasing approximately four-fold for a thousand-fold increase in concentration. The detection limit was found to be 0.002 p.p.m. or in absolute terms $2.0 \cdot 10^{-13}$ g. Normally the detection limit is assessed as the concentration at which the signal peak height equals twice the magnitude of the random fluctuation in the base line. Using the integrator removed the random fluctuation almost completely, and in this case it was found that baseline drift limited the minimum detectable signal. Precision data was obtained by analysing thirty solutions containing 0.25 p.p.m. Cd. The relative standard deviation defined as

$$\frac{\sigma}{x} \times 100\% \qquad \ldots\ldots$$

where σ is the standard deviation

and x is the mean

was found to be 10% and this was attributed to the following causes:

(i) variation in the quantity picked up by the loop.

(ii) plasma flicker.

(iii) variation in the proportion of sample entering the plasma (the plasma pencil did not completely fill the 2 mm jet orifice)

(iv) electronic noise, particularly drift in the potentiometers and operational amplifiers which were not chopper stabilised.

3.5. APPLICATION TO OTHER ELEMENTS.

Table 5 shows the limits of detection obtained with platinum or tungsten loops (as indicated) for a range of elements.

TABLE 5 LIMITS OF DETECTION FOR VARIOUS ELEMENTS.

Element	Wavelength (nm)	Loop Material	Limit of Detection(g)	Limit of Detection for 0.12 Micro l. sample (p.p.m.)
Zinc	213.85	Pt	$8.0 \cdot 10^{-11}$	0.67
Antimony	252.85	Pt	$5.0 \cdot 10^{-10}$	4.60
Selenium	203.98	Pt	$4.0 \cdot 10^{-10}$	3.24
Arsenic	228.81	Pt	$4.2 \cdot 10^{-11}$	0.35
Lead	261.41	Pt	$1.2 \cdot 10^{-10}$	1.0
Cadmium	228.81	Pt	$2.0 \cdot 10^{-13}$	0.0017
Iron	248.32	Pt	$3.0 \cdot 10^{-10}$	2.5
Iodine	206.16	Pt	$1.2 \cdot 10^{-9}$	10.0
Copper	217.89	W	$1.2 \cdot 10^{-10}$	1.0
Boron	249.77	W	$1.2 \cdot 10^{-10}$	1.0
Beryllium	234.86	Pt	$1.2 \cdot 10^{-10}$	1.0
Mercury	253.65	Pt	$1.6 \cdot 10^{-11}$	0.13

Relative detection limits (i.e. p.p.m.) could be improved by taking larger samples e.g. 5 micro litres placed on the loop with a syringe, or by evaporating several samples on the loop before high temperature vapourisation. As can be seen, the system is applicable to elements which are well known to form stable refractory oxides in flames, provided that the stable oxide is not formed on the loop at the

vapourisation stage.

For example, solutions of ferrous ammonium sulphate deposited on a platinum loop yielded no iron signal until excess HCl was added to the solution. It is thought that $FeSO_4.(NH_4)_2SO_4.6H_2O$ degrades to Fe_2O_3 (m.p. 1538° C) on the loop whereas the $(FeCl_4)^-$ ion (yellow) formed by the addition of excess HCl degrades to $FeCl_3.6H_2O$ which is more volatile (b.p. 280° C). Strong signals from atomic carbon at 247.8 nm were obtained when dilute solutions of acetone were placed in the sample cup. The results show that the system is capable of high sensitivity analysis on small sample volumes, for a range of elements in different matrix forms.

3.6. INTERFERENCES.

Generally interferences should not be a serious problem because the analyte species is at all times shielded and diluted by an inert gas, thus preventing vapour phase formation of stable oxides as often occurs in flames. Furthermore the plasma possesses energetic electrons capable of breaking the strongest of molecular bonds. The interference study carried out here relates to cadmium only because it was felt that this should give a general indication of interference problems and that a potential user of the system would require a specific study of his sample matrix that an apriori examination could not accomplish.

3.6.1. Special Interference.

Solutions containing 0.25 p.p.m. Cd together with various other elements present in thousand-fold excess were studied. The strongest spectral interference associated with cadmium comes from the 228.812 nm direct line emission of arsenic. The solutions of arsenic were prepared by dissolving arsenic trioxide in 20% (V/V) hydrochloric acid and then diluting to volume with water. When a sample containing both

cadmium and arsenic was vapourised by switching the current directly to 1.9 amps, a large positive interference was observed. However, it was found subsequently that emission peaks were observed without heating the loop and that further peaks could be obtained by increasing the loop current to its maximum over a period of time. (see section 3.7). No interference was observed from either cobalt or antimony, both of which exhibit emission close to 228.8 nm, Co at 228.781 nm and Sb at 228.898 nm, when present in thousand-fold excess. Cadmium solution (0.25 p.p.m.) containing 5000 p.p.m. sodium did show slight positive interference but this was due to light leaks by-passing the prism of the SP 900. Under these conditions sodium emission was observed visually for several minutes after the Cd signal had been received. The rapid temperature rise of the loop - 20 to ca 1400° C in about 0.1 seconds - probably causes an explosion of vapour, with the result that at high concentrations appreciable amounts of analyte become adsorbed on the cell walls and then proceeds to re-vapourise more slowly.

3.6.2. Chemical Interference.

The effects of phosphate, silicate, aluminium and vanadium when present in thousand-fold excess compared with cadmium were also investigated. Only vanadium, present in the form of ammonium metavanadate was found to interfere giving a 40% reduction in the expected signal intensity. Interference in the plasma system may originate from two sources; a process occurring on the loop preventing complete vapourisation of the analyte compound or the formation of a molecular species which is not completely degraded by collisional activation in the plasma. In the first case a time factor or memory effect should appear because of the higher temperature required

for complete sample vapourisation, as this was not evident the interference of vanadium was attributed to the second process.

3.7. OBSERVATIONS ON THE PLATINUM LOOP SAMPLING DEVICE.

Both Runnels and Gibson (49) and Winefordner et al (56) have described the use of the platinum loop sampling device but neither groups reported any unexpected observations. The Winefordner device was used in an atomic fluorescence system for producing atomic vapour which was then excited by an EDL.

3.7.1. The Occurrence of Multiple Vapourisation Peaks.

(i) Arsenic

Multiple vapourisation peaks were first observed when studying the interference of arsenic on cadmium. Figure 17 shows two traces (d.c. measurement) which illustrate the effect of adding arsenic to a cadmium solution, the concentrations were chosen so that the peaks caused by both arsenic and cadmium were easily discernible. When a solution containing 10 p.p.m. As alone was placed on the loop peaks 1 and 2 (Fig. 17) were observed after ca 40 seconds. The current was then switched on and increased steadily to its maximum of 1.9 amps; peaks 3 and 4 were observed when the current reached 1.5 amps and the loop was just below red heat (ca 500 °C). The separation of peaks 1 and 2 was about 3 seconds each, the separation of peaks 3 and 4 depended on the rate at which the loop was heated. Fig. 17 shows that cadmium was vapourised at a temperature between that of two of the arsenic peaks 3 and 4.

To establish beyond doubt the nature of each peak would have required an extensive and time consuming study which was not considered relevant to the main theme of the work. However the following observations were made, and some tentative conclusions drawn. An

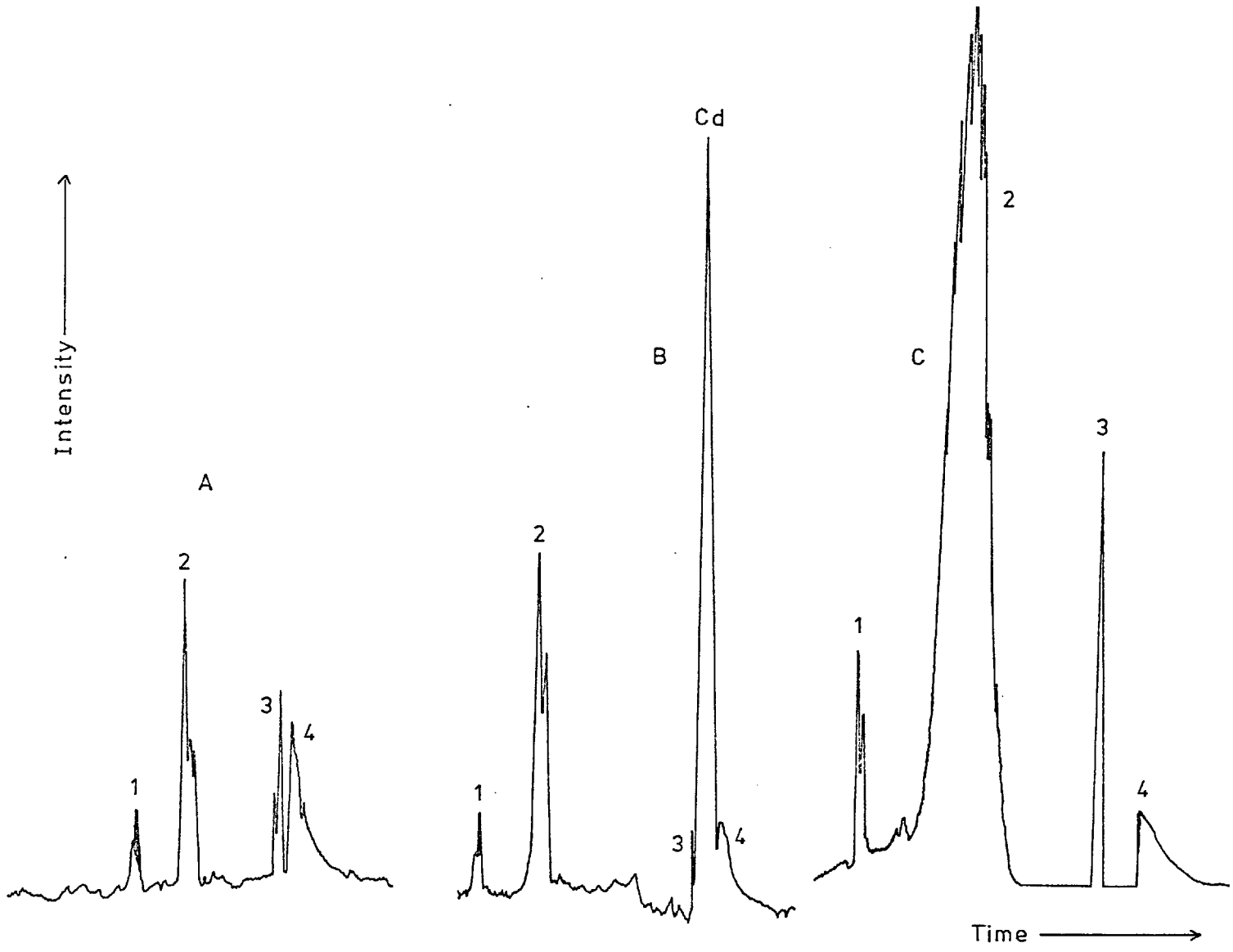


Fig.17. Multiple peak vapourisation of arsenic.

examination of the chemistry of arsenic indicated that the following compounds might have been formed during the evaporation/vapourisation cycle of the loop

ortho-arsenic acid $H_3AsO_4.\frac{1}{2}H_2O$ - m.p. 35.5 C; b.p. 160 °C

arsenous oxychloride AsOCl - unstable, no data available

arsenic trichloride $AsCl_3$ - m.p. 8.5 °C; b.p. 63 °C

arsenic trioxide As_2O_3:

natural form arsenalite (cubic or monoclinic) sublimes at 193 °C

claudetite m.p. 315 °C; b.p. 457 °C

arsenic pentoxide - decomposes at 315 °C

Fig. 17 shows that at high concentration i.e. 1000 p.p.m. peak 2 became the major species and from the above data it would appear that $AsCl_3$ is the most likely compound. Peak one could possibly be due to the unstable oxychloride. The peaks 3 and 4 probably resulted from the selective vapourisation of different crystalline forms of the trioxide.

(ii) Cadmium

The complex chemistry of arsenic made it difficult to identify all the species and therefore it was decided to try a simple mixture of cadmium chloride and cadmium iodide. Two strong peaks were observed but both were 'noisy' appearing to compose a number of smaller peaks. The noisy nature of the signals obtained in this work, was attributed to the rather crude method used for controlling the heating current ramp which involved turning by hand the spindle of a potentiometer.

(iii) Iron

Solutions of iron made up from $FeCl_3.6H_2O$ dissolved in 5% HCl yielded two peaks both below red heat. Assuming the first step

to be recrystallisation of $FeCl_3$, three possible forms could have been responsible

$FeCl_3.6H_2O$ m.p. 37 °C; b.p. 280 °C

$FeCl_3.2\frac{1}{2}H_2O$ m.p. 56 °C; no boiling point given

$FeCl_3$ m.p.306 °C; decomposes at 315 °C

(iv) Mercury

The solutions of mercury used in this study were made from $HgCl_2$ dissolved in 0.5% HCl and then diluted to one litre volume. Three peaks (Fig. 18) were observed and these were attributed to $HgCl_2$ m.p. 276 °C; b.p. 302 °C; Hg_2Cl_2 sublimes at 400 °C and Hg^0 m.p. -38.87 °C; b.p. 357 °C. Although at first surprising that Hg^I and Hg^0 should result from a solution of $HgCl_2$, it is well known that $HgCl_2$ is reduced to Hg^0 by boiling with HCl in the presence of a copper foil on which an amalgam forms. Platinum also forms an amalgam with mercury and it may be that the decrease in the free energy of the system caused by amalgamation is a driving force behind the reduction process.

In order to positively identify each of the peaks it was decided to investigate the effect of reducing and oxidising agents on the system. Reducing agents such as ascorbic acid, excess metallic mercury and $SnCl_2$ removed peak one and caused an enhancement of peaks 2 and 3. Oxidising agents such as acid $KMnO_4$ and Ce^{IV} resulted in an increase in peak one and a diminution of peaks 2 and 3. Finally a minute crystal of 'Analar' $HgCl_2$ was placed on the loop and a large peak lasting nearly one minute was observed followed by two smaller peaks. From the experimental data it was concluded that peak one was due to $HgCl_2$, peak 2 to Hg^0 and peak 3 to Hg_2Cl_2. The occurrence of three vapourisation peaks for mercury has also been reported with

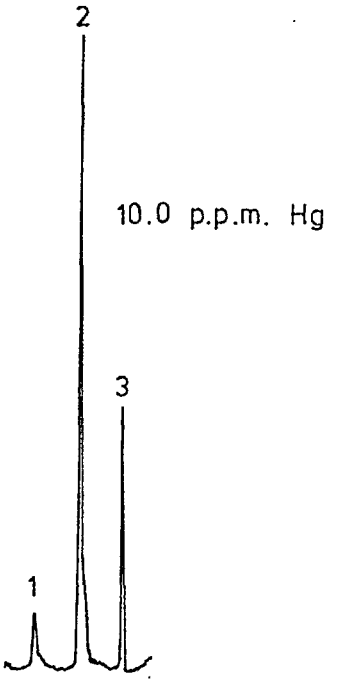


Fig.18. Multiple peak vapourisation of mercury.

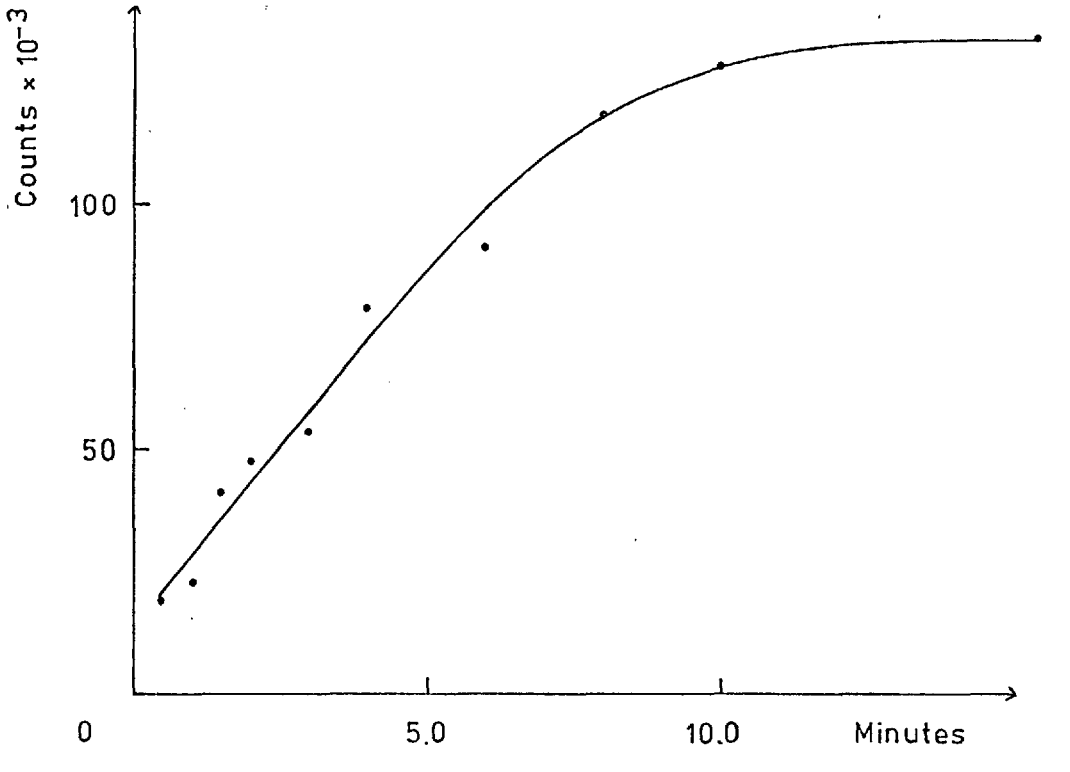


Fig.19. Adsorption of mercury vapour on platinum.

the Massmann furnace (91) and an R.F. furnace (92). When a system exhibits more than one emission peak and the peaks cannot be integrated by rapid heating, then an integral signal measuring technique must be employed in order to obtain linear calibration graphs.

3.7.2. Signal Enhancement by Analyte Adsorption on the Platinum Surface.

During the work on mercury it was noticed that when the system was not used for a few minutes a mercury signal was obtained on firing of the loop. This was attributed to the adsorption of mercury vapour - present in the gas flow system - onto the platinum surface. The effect was particularly strong when the apparatus was first in use and gradually disappeared during the course of a typical seven-hour working day. The mercury obviously originated from airbourne vapour in the laboratory and a check with a safety meter indicated a general level of approximately 3 micro g. m^{-3}.

To ascertain if quantitative analytical use could be made of the adsorption process, the loop was placed in a tube through which air was flowing and then emission signals recorded after different exposure periods. The measurements were made using the photon counting technique (see chapters four and five) and hence the emission intensity was recorded in 'counts'. The results are plotted in Fig.19 and do show that a uniform curve exhibiting linearity over the first stage can be obtained. Curvature of the graph above 100,000 counts may be due to a decrease in the rate of adsorption, but may also be partly due to the onset of pulse pile up in the counting system. The signal enhancement obtained for an exposure time of six minutes compared with one minute was about five times, indicating that levels below 1 micro g. m^{-3} are detectable after moderate exposure. There can be

little doubt that extremely low levels could be detected with long exposure times, but calibration in concentration units would be a major difficulty.

Having established that absorption on the platinum occurred in the vapour phase, it remained to ascertain whether the process occurred in aqueous solution. Solutions of mercuric chloride - first reduced with ascorbic acid - were chosen for the investigation. A 1.0 cm platinum coil exposed to a 1 p.p.m. solution for periods of 0.0 to 30.0 minutes yielded a curve similar in shape to the one shown in Fig. 19. Once again curvature of the graph occurred at high signal levels. The normal detection limit for mercury was ca 0.1 p.p.m., but it was found that a five-fold increase in the mercury emission at this level could be obtained by allowing the loop to remain in the reduced solution for ten minutes. This suggested a new detection limit of 0.02 p.p.m. and indeed a solution of this concentration was detected after an exposure period of ten minutes. The precision of these results was of course very poor (50% at the detection limit), but this method of sample concentration could prove of value when low levels of mercury exist and only micro litres of the sample are available for analysis.

An investigation is at present being carried out to determine whether the technique will work for other metals such as Ag, Cu and Au. These elements were chosen as they are reduced by ascorbic acid, which being an organic is unlikely to form thermally stable compounds and thus cause interference.

3.8. CONCLUSIONS

The results presented in this chapter show that the microwave plasma has much to recommend it as an excitation source in atomic

emission spectrometry. Coupled to a platinum loop sampling and vapourisation device it forms a versatile analytical system ideally suited to trace analysis, particularly when small samples only are available. The limited number of interferences suggests that the technique could find application where the sample is contained in a complex matrix e.g. in biological systems such as blood plasma.

An adaption of the plasma system is in use (93) for the monitoring of volatile elements vapourised from rock samples. The rock is either cut to a convenient size or powered with a graphite matrix and then placed between the coils of a 1 KW induction furnace. Argon is flushed over the sample and carries the volatilised elements into the plasma for spectral excitation. Low levels of elements such as Cd, As, Hg and Se have been detected and once again varying oxidation states have been observed by their different vapourisation temperatures. The plasma with its ability to excite a large range of elements is particularly valuable in this type of study where qualitative and semi-quantitative information about a complex and unknown sample is required.

Other uses that the system has been put to include (94) the monitoring of metallic halides released from a reaction vessel during a metallurgical conversion. Recent work in our own laboratory (58) has shown the plasma capable of exciting spectral lines in the vacuum U.V. e.g. Hg 184.9 nm, I 183.0 nm and S 180.7 nm. A technique capable of measuring low levels of sulphur could certainly find application in the analysis of oils. All oils contain sulphur but it is an undesirable constituent, because on combustion it forms corrosive compounds such as SO_2 and H_2SO_4 and lachrymatory organics.

Having pointed out the merits of microwave plasmas it is

appropriate to conclude this chapter with a discussion of the disadvantages involved in their use and to suggest how these might be overcome.

Certainly the major problem encountered is that of sample introduction and before plasmas can become established as a routine analytical method, techniques for continuous and automated one shot sampling must be found. Two approaches to sampling can be adopted, to introduce the sample to the plasma in the liquid phase or to evaporate the solvent first and introduce the sample in the vapour phase. The second method is preferable for the reasons given earlier, but difficulties arise when the sample contains compounds of high thermal stability that are not easily vapourised and therefore contaminate the sampling device. Practical difficulties arise in designing a continuous sampling device of the second type, because a means of introducing low rates of sample to the vapouriser must be found. One suggestion that might be practical is a continuous wire that picks up a surface tension film of solution, and is then electrically heated power being drawn from two knife edge electrodes. Another, that could provide an answer is to use two plasmas in series; aqueous sample on a continuous wire or from a fine silica capillary is introduced into the first one, and the second is used only for exciting the vapour produced.

Introduction of sample in the liquid phase depends on finding a means of nebulising solutions at extremely low flow rates, i.e. less than 1 micro l sec^{-1}. Pneumatic nebulisers produce quantities several orders of magnitude above this and cannot be considered suitable for this application. Ultrasonic devices have been used as nebulisers (95,96) and could possibly be adapted for use with plasmas.

Two types have been investigated, aerosol generators and individual drop generators. The former function function by focussing an ultrasonic wave at the liquid gas interface where a droplet cloud is produced. Problems arise with sample interchange, variation in droplet size and maintaining an accurate focus. The latter type form droplets (down to 25 microns diameter) by vibrating at high frequency a capillary (up to 0.25 mm diameter) through which the sample is flowing. The jet formed at the capillary orifice then breaks up into uniform droplets whose rate can be controlled by selective charging and electrostatic focussing of the droplet beam. The device is elegant in its mode of operation but is probably too complicated and costly for routine analytical application.

The reproducibility of the plasma system was not sufficient to allow high precision analysis (i.e. 2%) from a single sample. Instability of the plasma was considered a major factor in this, and therefore some consideration should be given to the underlying causes viz.

(i) power stability

Stabilisation of the power coupled to the plasma was more difficult than expected because even if the output from the magnetron valve is constant, a number of factors can affect the actual power dissipated in the plasma. Cavity tuning is the most critical factor and this in turn is affected by changes in the cavity temperature, in the plasma dimensions and frequency drift in the magnetron valve. The work reported here utilised the early Microtron 200 unit which does not include current stabilisation of the magnetron (as do later models) and therefore source power fluctuations were added to those caused by variable tuning. The total r.m.s. power fluctuation was estimated to

be 5% at 40 watts.

(ii) stability of the gas stream.

Standard cylinder pressure heads and needle valves were used for controlling the argon flow rate and together with a smoothing reservoir of one litre kept flow rate fluctuations to about 1%. Air currents within the laboratory probably contributed to plasma flicker and an improved design would employ argon shielding around the plasma, to yield better stability and lessen the background radiation caused by entrained nitrogen.

Variation in the quantity picked up by the loop was another factor contributing to the loss of analytical precision. The loops were formed by wrapping the wire round a steel needle and then twisting the side arms once. The twist in the loop may have caused sampling error and an attempt was made to spot weld the wire, however the welds tended to break on heating.

Noise from the electronics also added to the overall variance but this has already been dealt with briefly and will be examined closely in the chapters dealing with photon counting.

oooOOOooo

CHAPTER IV

PHOTON COUNTING, A SIGNAL MEASUREMENT TECHNIQUE FOR ANALYTICAL ATOMIC SPECTROMETRY

4.1. INTRODUCTION.

The experience gained using the d.c. amplifier/integrator showed that such devices are limited at low light levels by baseline drift. The problem was not too severe for the short duration pulses encountered with the plasma system, but undoubtedly would have been a serious drawback had longer period integration been required. The demand for lower detection limits has led to the investigation of integral techniques as a means of measuring weak radiation signals with greater precision. Photon counting offers an alternative to capacitative integration and unlike the latter it should not be unduly subject to drift problems. It was therefore decided to investigate the technique as a means of integrating and measuring weak radiation signals of the type obtained in analytical spectrometry. The aim therefore, was to produce a photon counting system capable of measuring extremely low levels of radiation, rather than one that could cover a large intensity range. This distinction is important because certain features of system design are affected by the type of signal to be measured; further discussion of this point is postponed until section 4.6.1.

Photon counting involves the direct digital recording of the current pulses resulting at the anode of a photomultiplier, caused by photon impact at the photo-cathode. Provided that the rate of photo-electron emission and pulse-pair resolution of the electronic system are such that individual pulses are resolved, the measurement affords a direct digital analysis of the radiation intensity.

The photomultiplier remains at present the prime detector of radiation in the U.V., visible and infra-red region of the spectrum. The extremely high internal gain, affording low noise signal amplification of up to x 10^8 and the linearity of the device over several orders of

signal magnitude make it the universal choice for low intensity radiation measurement. Undoubtedly in the future photo-diodes and photo-transistors (97 - 99) having unit quantum efficiency over a wide spectral range will replace the photomultiplier, but to date the gain of these devices has been too small to make them a viable alternative.

Photon counting is best suited to the measurement of low levels of radiation and hence its application in analytical atomic absorption, emission and fluorescence is obvious. The current trend in atomic spectrometry towards the use of non-flame atom reservoirs (53 - 56) producing weak and transient radiation signals, requires that close attention be given to the response characteristics of the detection system used. All counting techniques effectively integrate the signal and as will be demonstrated, this can be of particular value for transient signals and signals having certain kinds of noise component. Furthermore, the direct digital output of photon counting makes it ideal for interfacing with modern computerised data handling systems.

4.2. THE INTEGRAL TECHNIQUE OF SIGNAL MEASUREMENT.

Radiation signals in atomic spectrometry can be divided into two basic types for the purpose of theoretical analysis. The most common are the steady state signals where the analytical signal is essentially constant with time. Such signals are obtained from conventional pneumatic nebulisers supplied as standard equipment with most commercial atomic spectrometry instruments. Arc and spectrophotometric studies can also produce steady state signals. The other type of signal is the transient signal in which the radiation intensity is a function of time. Transient signals have become more common in recent times with the development of non-flame cells for

atomisation e.g. the platinum loop atomiser (56), West type filament (55), Massmann furnace (53) and L'Vov furnace (54).

The only theoretical analysis of analytical signals in atomic spectrometry is that by Professor L'Vov (23) and although there are certain departures from reality in the mathematical treatment, they are not serious and valid conclusions can be drawn. The Theory derives expressions for pulse shapes of both steady state and transient analytical signals. It shows that there are three basic parameters that can be measured in order to estimate the concentration of the analyte; the equilibrium value (steady state signals only), the peak value (transient signals only) and the integrated area under the curve (steady state and transient signals). For both types of signal it is shown that the integral measurement yields the highest sensitivity and that this sensitivity is in proportion to the time that the analyte atoms spend in the analytical cell. Furthermore and perhaps most important, the theory demonstrates that the result obtained by integral measurement is independent of the rate of sample introduction into the cell. This is of particular importance for signals of variable duration or where two samples contain similar amounts of analyte, but the matrix causes a different rate of introduction into the analytical cell.

Generally equilibrium values are the easiest to measure because any d.c. or a.c. current measuring circuit (assuming the prime detector to be a photomultiplier) will effectively monitor a steady signal. Peak measurement is usually accomplished with d.c. systems and it can be shown that circuit time constants must be kept short (100) if distortion of the analytical pulse shape is to be avoided. Integral measurement has in the past been achieved by capacitative charge

integration, but in this chapter it will be domonstrated that photon counting can be an excellent alternative technique.

4.3. THE PRINCIPLES OF PHOTON COUNTING.

4.3.1. The Photomultiplier Tube.

The single most important item in a photon counting system is the photomultiplier tube (PMT) whose mode of operation is fundamental to the technique of photon counting. The mechanism of the device is well known but a brief description will be given in order to point out which factors are of importance in relation to photon counting.

(i) Structure.

The structure of a typical photomultiplier of the venetian blind type is shown in Fig. 20. When the tube is to be used for atomic spectrometry requiring wavelength coverage from 170 - 600 nm the envelope is made of quartz and the photo-cathode is generally of the S-11, S(EMI only) or bialkali type. Three dynode structures are commonly employed; the venetian blind structure which yields high gain, high gain stability and low noise performance; the fast linear focussed structure yielding high gain, fast pulse rise times but inferior noise and gain stability characteristics to the venetian blind type; the box and grid structure which offers moderate performance at moderate cost. For detailed information about the various types of PMT available see references (101, 102).

(ii) Mode of Operation.

The first dynode is biased positive with respect to the photo-cathode and each subsequent dynode biased more positive with respect to the previous one. The biasing voltages are obtained by potentiometrically dividing down the output of a well stabilised EHT supply (101). Typical interstage voltages are in the range 150 - 500 V and the

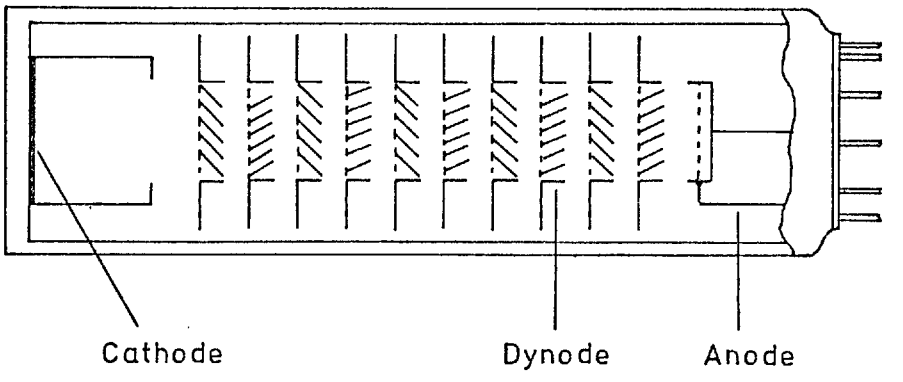


Fig.20. Venetian blind photomultiplier.

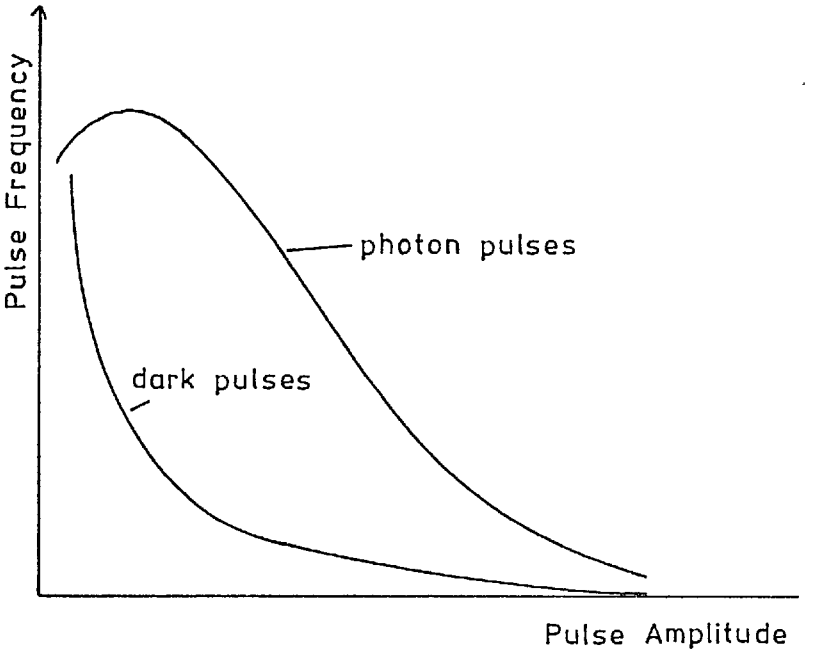


Fig.21. Photomultiplier pulse amplitude distributions.

number of stages varies between nine and fifteen, so that in general a 3 KV supply is adequate (5 mA). A photon striking the photo-cathode causes the emission of a photo-electron with a probability ϕ known as the quantum efficiency. The photo-electron is accelerated by the electric field and strikes the first dynode where it causes the ejection of a number of secondary electrons. The number of secondary electrons released δ is a statistical quantity which under ideal conditions has a Poisson distribution characterised by the mean $\bar{\delta}$. The secondary electrons released from the first dynode are accelerated into the second dynode and there result in further secondary emission. The multiplication continues down the dynode chain which typically may have an overall gain of $10^5 - 10^8$. Because the multiplication process is statistical, the pulse resulting at the anode varies in magnitude and when the dynode statistics are Poisson the distribution of pulse magnitudes is also Poisson (see Fig. 21). It can be shown that the resulting variance in single photo-electron pulse magnitude is given by (102)

$$\sigma_G^2 = (G)^2 \left(\frac{\sigma_1^2}{\bar{\delta}_1^2} + \frac{\sigma_2^2}{\bar{\delta}_1 . \bar{\delta}_2^2} + \cdots + \frac{\sigma_k^2}{(\bar{\delta}_1 . \bar{\delta}_2 \cdots \bar{\delta}_{k-1}) \bar{\delta}_k^2} \right)$$

where σ_G^2 is the variance in the overall gain G

σ_i^2 is the variance associated with the i_{th} dynode

$\bar{\delta}_i$ is the average gain of the I_{th} dynode

k is the number of dynodes.

which in turn shows that the largest contribution to the pulse height variance comes from the first stage. Now for a Poisson distribution σ_1^2 is equal to $\bar{\delta}_1$ so that the variance in the overall gain can be significantly reduced by making the first stage gain as large as possible. Indeed when this is done the signal to noise ratio for the whole chain

can be approximated to:-

$$\frac{G}{\sigma_G} \doteq (\bar{\delta}_1)^{1/2}$$

The statistics for dynode chains vary between the Poisson and the Exponential distributions (102); Poisson statistics have the advantage that for a given gain G, the overall variance σ_G^2 is less than that for Exponential statistics. The result is that the pulse height distribution is narrower and the dynode chain signal to noise ratio greater. The ability of a PMT to produce a narrow range of pulse magnitudes for single photon inputs is of importance for both photon counting and current measuring techniques. This will become apparent in the sections dealing with shot noise and pulse discrimination.
The gain of the photomultiplier can be expressed in the form

$$G = \eta\ (p\ \bar{\delta})^k$$

where η is the first dynode collection efficiency

and p is the inter-dynode collection efficiency

To measure each parameter separately is difficult and therefore manufacturers use a standard intensity source and measure the photocathode sensitivity S in micro amps per lumen, the overall sensitivity M (at a given operating voltage) in amps per lumen and specify the gain as

$$G = \frac{M}{S} \quad x \quad 10^6$$

The electrons which traverse the dynode chain do so over different paths and therefore arrive at the anode at different times. It has been shown (103) that the time distribution of electron arrival at the anode is Gaussion so that the current pulse can be expressed in the form

$$i_a = \frac{Ge}{\sigma\ (2\pi)^{\frac{1}{2}}} \cdot \exp - \left(\frac{t^2}{2\sigma^2} \right) \qquad \ldots.4.1.$$

where c is the charge on the electron

σ is the standard deviation

and t is the time.

The pulse width is therefore specified by the width at half maximum amplitude which corresponds to 2.36σ . Typical values of the pulse width are 15 nS for a venetian blind tube of 13 stages and 2.5 nS for a fast focussed tube of 14 stages. The width of the pulse is an important consideration in photon counting, because the technique depends on time resolving individual pulses when the average rate of pulse arrival is high. Tubes producing narrow pulses are therefore superior for use in photon counting systems.

4.3.2. Photomultiplier Dark Current.

A photomultiplier placed in absolute darkness will still generate current pulses. These pulses are sometimes incorrectly referred to as dark current noise. A steady signal, no matter what its origin might be, does not constitute noise, because a well defined signal can be subtracted from a result without loss of precision. It is the random or correlated fluctuations in the signal that constitute noise and cause the signal to noise ratio to be finite. The sources of dark current will now be considered.

(i) Thermionic emission

For most PMTs thermionic emission from the photo-cathode is the major contributor to dark current. Thermal dark current approximately obeys Richardson's Law:-

$$I = 1.2.10^{2}\ T^{2} \exp - \left(\frac{1.16.10^{4}\ \phi_{T}}{T} \right)$$

where T is the temperature

and ϕ_{T} is the thermal work function.

The temperature occurs twice in the expression and it is generally found that cooling a PMT to about -40 °C is sufficient to reduce the thermal dark current effectively to zero. The resulting anode pulses are undistinguishable from photon pulses because they experience the full gain of the dynode chain. Thermionic emission can also occur from the dynodes although with less frequency, because the thermionic work function of the metal dynode surfaces is higher than that of the semi-conductor photo-cathode surface. Thermionic pulses from the dynode chain can be distinguished from photon pulses because in general they experience less gain and are therefore smaller. When it is not convenient to cool the PMT, a specially processed photo-cathode having a higher than usual thermal work function can be employed e.g. the EMI 'S' type photo-cathode.

(ii) Pulses originating from radioactive sources.

The glasses used in photomultiplier manufacture contain residual amounts of natural K^{40} isotope which emits β particles that result in bursts of Cerenkov photons from the glass. Cosmic particles can also cause dark pulses by secondary emission from the photo-cathode and dynode surfaces, Cerenkov mechanism and residual gas ionisation. Finally glass fluorescence may occur when the tube is used in the presence of γ radiation sources. Generally pulses derived from radioactive sources are larger than photon pulses, because a burst of photons or electrons is generated in a time that is short compared with the anode pulse width.

(iii) Cold field emission and residual gas ionisation.

Pulses from these sources are not important when the PMT is run at the recommended operating voltage, but they are the major dark current component at higher voltages.

(iv) Ohmic leakage.

Small d.c. currents always exist in PMTs because some of the electrons miss the dynode chain and drift to the anode independently of the main electron avalanche. However, these unpulsed currents do not contribute to the count in photon counting.

It may also be mentioned that any metallic components touching the envelope not at the cathode potential, and electrostatic and magnetic fields can affect the force field in the PMT and cause large increases in the dark current. Mu-metal shields are often used to protect the PMT from external influences. A typical dark pulse amplitude spectrum is shown in Fig. 21. The spectrum has proportionately more large pulses - from radioactive origin - and more small pulses - from pulses originating along the dynode chain - than the photon pulse spectrum.

4.3.3. Pulse Pile-up in Photon Counting.

Pulse pile-up is the term given to the situation that occurs when the photo-electron pulses are not fully time resolved by the counting circuitry. Before describing the mechanism of pulse pile-up it is necessary to indicate that the pulse width at the point of counting is a function of the entire electronic circuitry and not just the photomultiplier, so that in this discussion it is the final pulse width that is being considered and not the anode pulse width. Furthermore, every counting system has a counting threshold which the pulse amplitude must exceed, in order to trigger the counting circuit to place a one in the register. Most modern logic devices are edge triggered and respond to either a positive or negative going edge, exceeding some pre-determined value.

The normal sources (not lasers) encountered in analytical atomic

spectrometry emits photons randomly in time (in the limit of considering only a few photons), that is to say that the emission of one photon in no way affects the time of emission of the next. Under these circumstances photon emission can be considered as a Poisson process, which means that even at the lowest photon arrival rates there is still a finite probability that two photons will arrive almost simultaneously.

Two pulse pile-up mechanisms can occur and these are depicted in Fig. 22. In the first, two pulses overlap so that the resulting waveform does not drop below the threshold level until after both pulses have passed through the counting network. The result is that a 1 is placed in the register instead of 2. This type of pulse pile-up dominates at high photon arrival rates and as a result the count rate versus intensity curve bends towards the abcissa. Before describing the second mechanism it is necessary to mention the concept of pulse amplitude discrimination which will be further dealt with later in this chapter. Morton (104) in a review of the fundamentals of photon counting pointed out that because the pulse amplitude distributions of the photon and dark pulses are different it is possible to discriminate against dark pulses. It was suggested that the ideal system would use window counting i.e. having a lower threshold to reject dark pulses originating from dynodes other than the first and an upper threshold to reject large pulses of radioactive origin. When a discriminator is used, the other pulse pile-up mechanism may operate i.e. two small dark pulses that should not be counted may add algebraically and result in a large pulse that is counted. This mechanism can lead to error when the photon flux is low.

Pulse pile-up resulting in count loss is the mechanism of most importance in analytical studies (see later sections) and therefore an

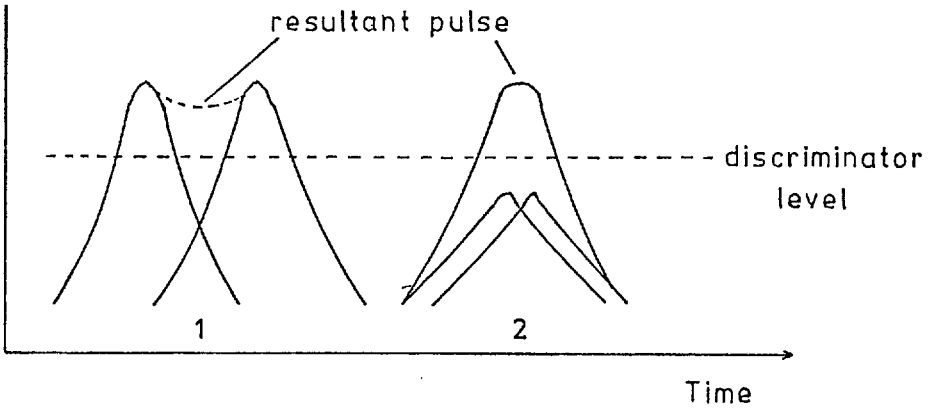


Fig.22. Pulse pile-up mechanisms in photon counting.

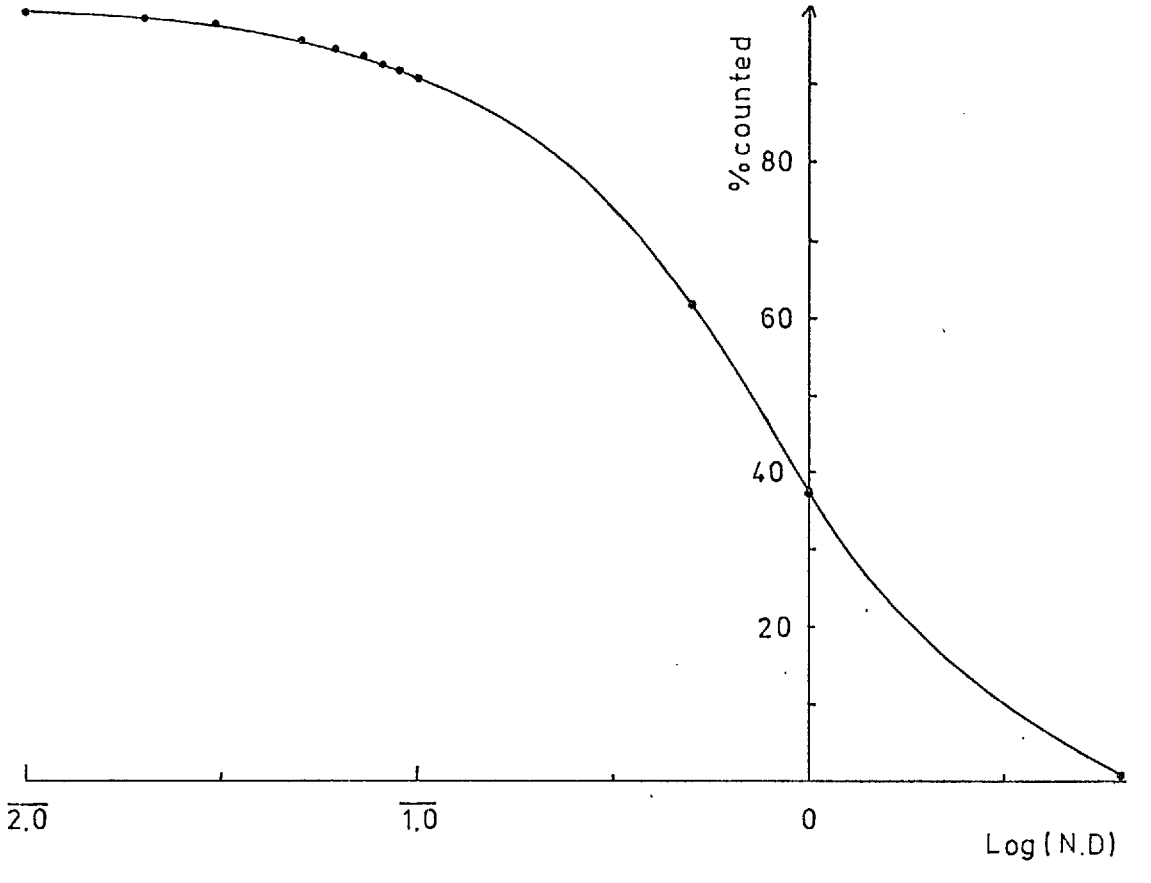


Fig.23. Percentage of photons counted as a function of the product N.D.

investigation of the effect of pile-up on a counting experiment was carried out. Rather than use a practical counting system which would have a number of unknown parameters it was thought that more information could be obtained by simulating the experiment on the College IBM 7094 digital computer.

The limiting factor in a counting experiment carried out at a high photon arrival rate, is the ability of the counting circuitry to resolve two closely spaced pulses. For the purpose of simulation, this ability can be represented by specifying for the counting system a 'dead time'. The dead time is the period that must elapse, following the arrival of the first pulse, before another pulse can be counted. Any pulse that arrives during the dead time is not counted and therefore the effect is that of the first pile-up mechanism. Thus the experiment can be represented by considering three variables

(i) the average rate of photon arrival (N)

(ii) the counting system 'dead time' (D)

(iii) the count period (T)

A stable, thermal radiation source emits photons that are Poisson distributed in time, so that the probability of r events occurring in unit time is given by

$$P(r) = \frac{e^{-N} N^r}{r!} \qquad \ldots.4.2.$$

where N is the average number of events per unit time.

Now for events that are Poisson distributed in time, the times between events follow the Negative Exponential Distribution whose probability density function is

$$f(t) = N \exp -(Nt) \qquad \ldots.4.3.$$

Thus photon arrival was simulated by using the library routine RNIST(X)

which generates random numbers in the interval 0 - 1, and taking the time of arrival of the next photon as the product of the average time between photon arrivals and the negative natural logarithm of the next random number. The program then operated in the following manner. The first photon arrives at some time t and a 1 is placed in a count register. After the arrival of the first photon the next one cannot be counted until after the time t + D. Thus if the next photon arrived after the time t + D the count register was raised to 2 but if it arrived before t + D the register remained at 1, and so on. Rather than forget the photons not counted it was decided to place them in a series of registers corresponding to 1,2,3 ..... or n photons missed during a dead time. Therefore, for a given set of variables, N, D and T the following information was obtained.

(i) the total number of photon arrivals in the time T

(ii) the number and percentage of photons counted

(iii) the number of photons not counted

(iv) the number of times that 1,2,3, ... or n photons were not counted during all the dead times.

A complete transcript of the program is presented in Appendix I . The results from the program can be obtained from equations 4.2 and 4.3, but the simulation technique is a more elegant method because it approximates to a real experiment.

Fig. 23 shows the percentage of photons counted as a function of the product N.D. Clearly if the system is to be used as an absolute radiation intensity measuring device, with less than 1% error due to pile-up loss, then the count rate should not exceed 0.01 times the reciprocal system dead time. Indeed when the system dead time equals the average time spacing of the photons only ca 37% of the photons are

counted. From Fig.23 a log-log curve of photon arrival rate versus count rate i.e. an analytical curve (linear portion only) can be obtained by plotting the same abscissa values (see Fig.24) versus the sum of the abscissa values and the log of the corresponding curve ordinates. Such a graph is shown in Fig.24 where it can be seen that the curve is approximately linear over the first portion, but tails off at high photon arrival rates i.e. radiation intensity, eventually having a negative gradient. As will be seen, practical count versus intensity curves approximate to this shape although real analytical signals rarely correspond to Poisson statistics. Furthermore,it is unusual to increase the intensity above the initial curvature point, because this adversely affects the PMT dark current and excessive intensities may damage the PMT.

The frequency distribution of missed counts also depends on the product of the average photon arrival rate and the counter dead time. This is illustrated in Fig. 25 where the distributions for N.D = 1 and N.D = 50 are shown. When N.D = 1 the area under the distribution should approximate to 73% of the total photon number, viz Fig.23 , whereas when N.D = 50 the area under the distribution includes nearly all the photons since only a few are counted.

The conclusions established by the simulation relate to an ideal system, but they do indicate how pulse pile-up affects counting experiments.

4.4. A PRACTICAL PHOTON COUNTING SYSTEM.

4.4.1. Design Considerations.

Having decided that photon counting could be an alternative to capacitative integration the need arose to construct a practical system. Two photon counter designs had appeared in the literature (105, 106),

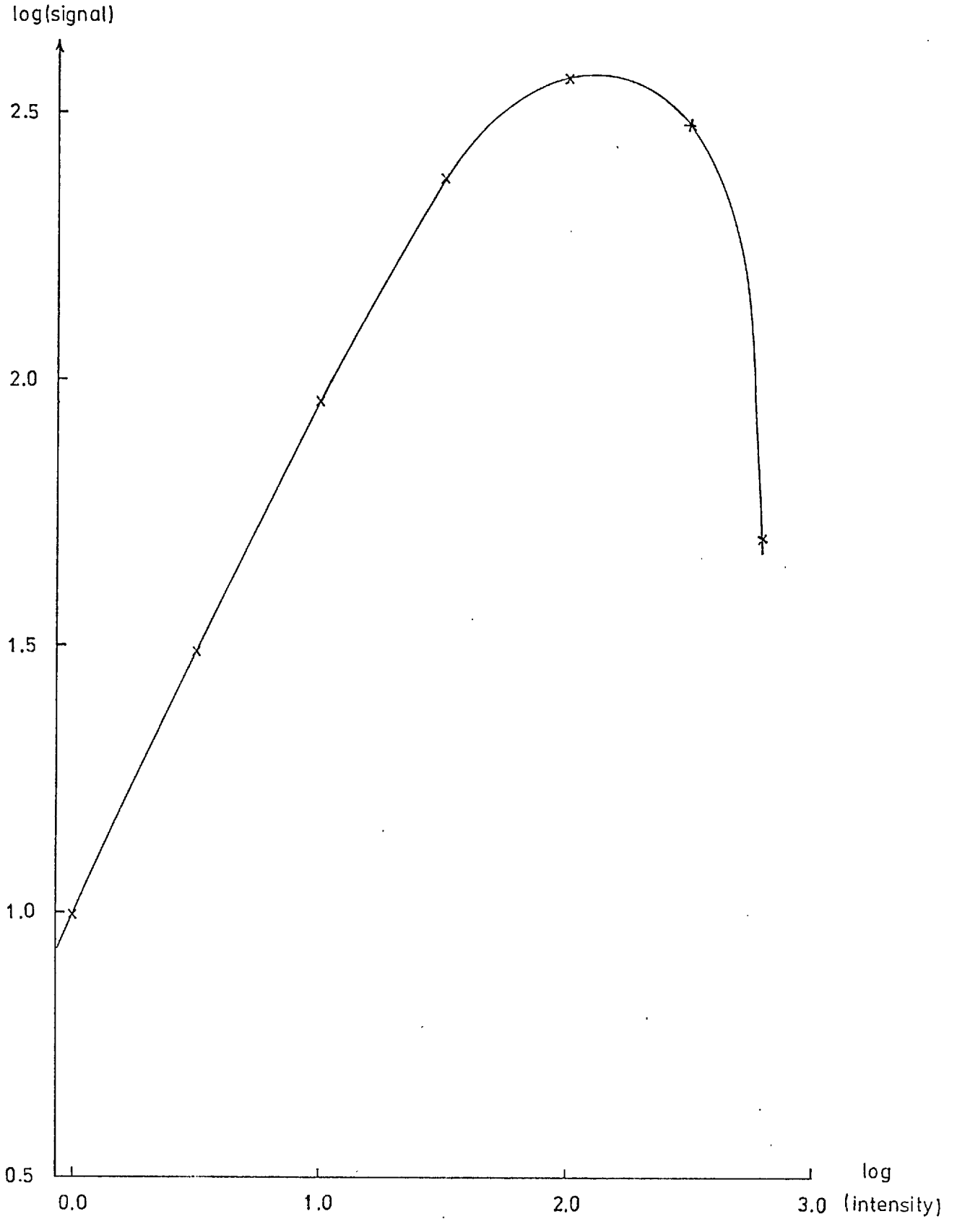


Fig.24. Computed count rate versus radiation intensity curve.

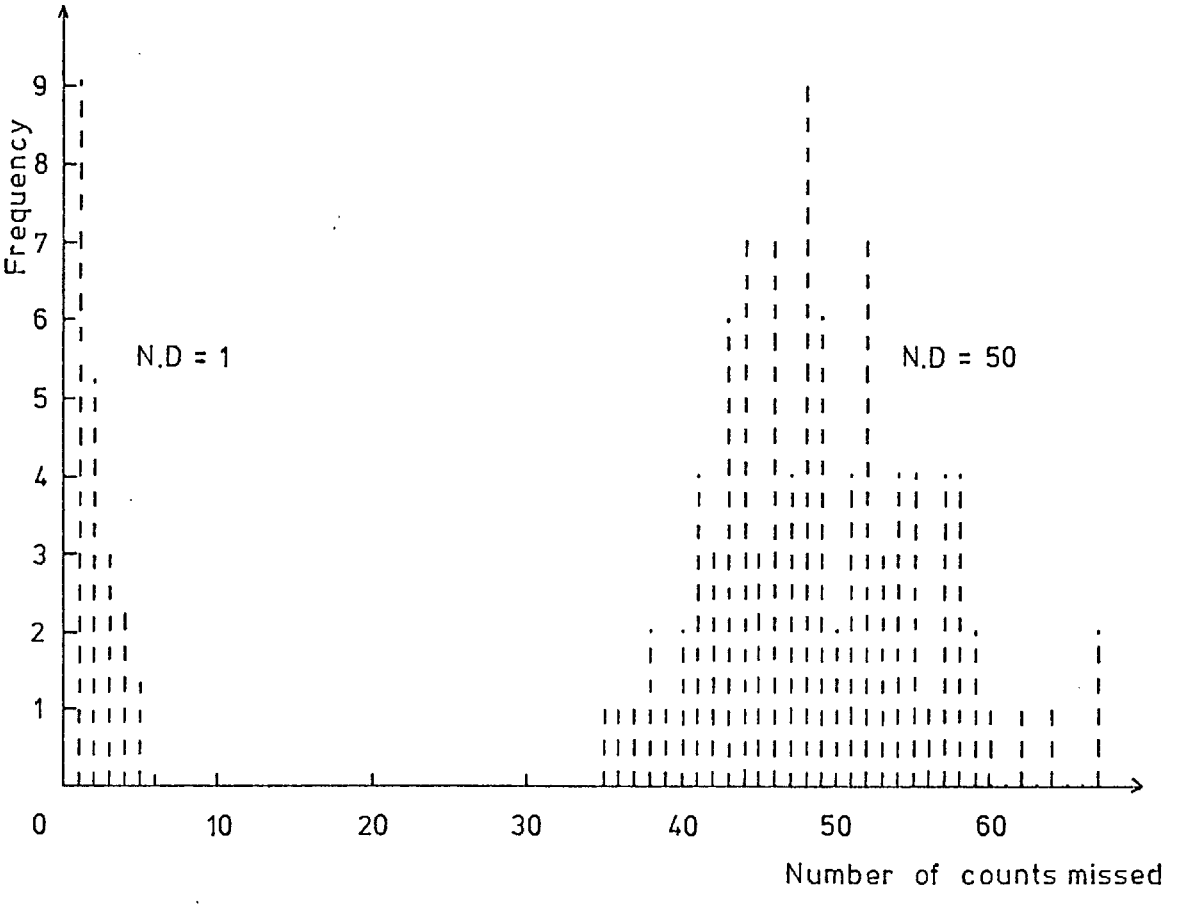


Fig.25. Frequency distribution of missed counts.

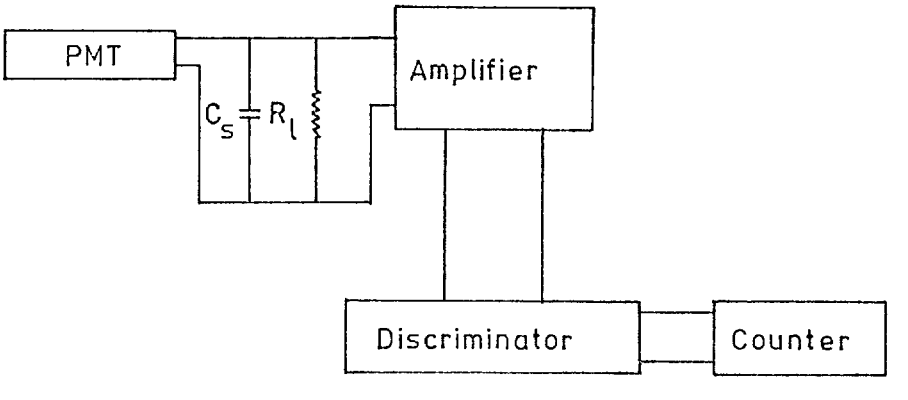


Fig.26. A typical photon counting system.

both comprising five major components i.e. the PMT, an anode load resistor, a pulse amplifier, a pulse amplitude discriminator and a pulse counter or frequency meter. The decision was made to follow this design scheme and therefore a schematic diagram of the circuit is shown in Fig. 26. The basic design criteria for photon counting systems are that pulse pile-up (unless otherwise stated pulse pile-up will refer to the first mechanism only) should be reduced to a minimum and that the system be of low noise character. The noise in a system can be equated to the standard deviation of the signal level, which represents the root mean square deviation about the mean. In d.c. circuits noise is considered as the standard deviation of the current level, but in counting systems a different appraisal is necessary. Consider the case of a steady radiation signal producing N photo-electron pulses per second from the PMT and the counting system producing N_d dark pulses per second. If both pulse trains were Poisson distributed in time, then the mean and variance of each distribution would be N and N_d respectively. Now for independent variables the total variance of the system is given by the sum of the individual variances i.e.

$$\sigma^2 = N + N_d \qquad \ldots.4.4.$$

where σ^2 is the total system variance.

However in measuring N it is necessary to make a separate measurement of N_d, with the result that an additional variance term of N_d is introduced into equation 4.4 which then becomes

$$\sigma^2 = N + 2N_d$$

Now since the noise is given by the standard deviation which is equal to the square route of the variance, the signal to noise ratio of the

measurement becomes

$$\frac{N}{\sigma} = \frac{N}{(N + 2N_d)^{\frac{1}{2}}} \qquad \ldots.4.5.$$

Thus the signal to noise ratio is degraded by the number of system dark pulses which should therefore be kept to a minimum.

The minimisation of pulse pile-up is achieved by designing the system to have optimum pulse pair resolution. This parameter is not often specified for amplifiers, frequency meters etc., however their suitability can still be determined from the frequency response and bandwidth of the device. The minimum pulse rise time T_r for a system having an upper 3dB point of F Hz. is

$$T_r = 0.35 / F \qquad \ldots.4.6.$$

Equation 4.6 shows clearly that the higher the frequency response of the system, the narrower the pulse width and therefore the better the pulse pair resolution. Unfortunately high frequency response, low noise and high gain (sufficient to raise the mean anode pulse amplitude above the trigger level of counter) tend to be mutually exclusive for devices such as amplifiers and discriminators. It is therefore necessary to choose an amplifier having sufficient gain, and then seek the best frequency response and noise characteristics compatible with that gain.

The photomultiplier anode circuit comprising the anode load resistor R_L in parallel with the total stray capacitance C_s is also of great importance in minimising pulse pile-up. Generally C_s is fixed for a given system (C_s is minimised) leaving the optimum value of R_L to be determined. A detailed analysis of the effect of the values of R_L and C_s is given later in this chapter, this work had not been carried out at the time of building the first system. It was known

however (106) that in order to optimise pulse pair resolution the circuit time constant $R_L C_s$ should be kept to a minimum, but that decreasing R_L too much lowered the mean pulse amplitude to the point where it was insufficient to trigger the pulse counter. The final value of R_L was therefore determined experimentally and the method of achieving this will be described later in this section.

4.4.2. Experimental Equipment.

The photon counter was to be used for analytical studies and therefore had to be interfaced with a monochromator. No well-suited instrument was available and so a Unicam SP900 was adapted for the purpose. The SP900 has the disadvantage when used for photon counting, that the PMT is located in a housing inside the light tight compartment. This made it virtually impossible to cool the tube, and to reduce the length of the signal output cable below about 9 inches which greatly contributed to the total stray capacity of 40 pF(coaxial cable has a distributed capacitance of about 25 pF per foot which adds to the stray capacity, it is therefore desirable to keep the cable linking the PMT to the amplifier as short as possible). The PMT employed was an EMI 9601B which is fitted as standard equipment to the SP900. The 9601B is an eleven stage box and grid tube, having an S-11 photo-cathode, typical gain of 4.10^6 and an anode pulse width (2.36σ) of 38 nS. Photo-electron pulses from the PMT were amplified by a wideband a.c. amplifier (AIM electronics type ACA 123 powered by module PSU 101) having a variable gain (in 5 stages) from 1000 to 30 dB down on 1000. The bandwidth of the amplifier at X1000 was 0.6 Hz. - 4.5 M.Hz. and at 30 dB down 0.6 Hz. - 6 M.Hz. (when terminated correctly in 4.7 K ohms). The amplified pulses were counted using a 40 M.Hz. frequency meter (Venner Electronics type TSA 6636/3) having a 10 mV counting threshold

and 6 digit read-out. This particular frequency meter had an internal pulse height discriminator which proved to be adequate for photon counting experiments.

4.4.3. Operation and Evaluation of System.

Three system variables namely the amplifier gain, the discriminator level and the value of the anode load resistor required optimisation. Initially a 4.7 K ohm load (the impedance of the amplifier) was chosen in order that the optimum gain and discriminator settings could be determined, this was accomplished as follows. The entrance slit of the SP900 was illuminated with a tungsten filament lamp operated from a stabilised d.c. supply. The wavelength control was set to 550 nm and the slit width adjusted to yield an output current from the PMT of about 10 nA (in the current mode PMT anode pulses are integrated by the large circuit time constant and therefore merge to form a quasi steady current). The current was measured by connecting the output of the PMT to a servoscribe potentiometric recorder having a 20 K ohm load resistor across its input terminals. Gain and discrimination levels were then varied independently and the settings yielding the maximum signal to noise ratio determined by application of equation 4.14 (both tungsten lamp and dark pulses approximate to a Poisson signal, see later in this section). The optimum values were, gain 12 dB down (i.e. x 76) and discriminator level scale mark 1 (no discriminator calibration was available). It was found that at low discriminator levels the dark count completely saturated the system, yielding count rates in excess of 10^6 c.p.s. (counts per second). This large count was traced to small pulses generated internally by the amplifier. The discriminator was not therefore being used to differentiate between dark PMT pulses and photo-electron PMT pulses,

but to remove pulses generated by the amplifier. At the optimum discriminator level dark pulse rate was reduced to 450 c.p.s.

The sensitivity and linearity of the photon counting system is best tested by plotting a count rate (dark count is first subtracted) versus light intensity curve and comparing this with a reference curve. The output current of a PMT varies linearly with radiation intensity over the entire working range, typically 1 nA - 1 mA. It is therefore possible to plot the abcissa directly as d.c. current and avoid the necessity of intensity calibration of the optical system. The reference curve is plotted from the manufacturers gain specification of the particular tube. For example, a signal resulting in an average of N photo-electrons per second, impinging on a tube of gain G should yield an average output current i_a of:-

$$i_a = N.\ e.\ G_k \text{ amps}$$

where the symbols have their usual meanings.
For the particular tube employed, the actual gain figure was not available and therefore the nominal gain of 4.10^6 at 1 KV was used to calculate the reference curve which is shown in Fig. 27.

Three count rate versus current curves for three different load resistors i.e. 4.7 K ohms, 470 and 50 ohms are also shown in Fig.27 . The curves were obtained in the following manner. The tungsten lamp was adjusted so that with the slit width set at 0.15 mm, about 5.10^{-6} A was drawn from the PMT. This procedure ensured that the radiation intensity could be easily adjusted with the slit width control of the monochromator. The slit width was then reduced until the minimum measurable d.c. current was found. Beginning at this slit width, the radiation intensity and hence the PMT current was increased until it was clear that the count rate was no longer increasing in proportion

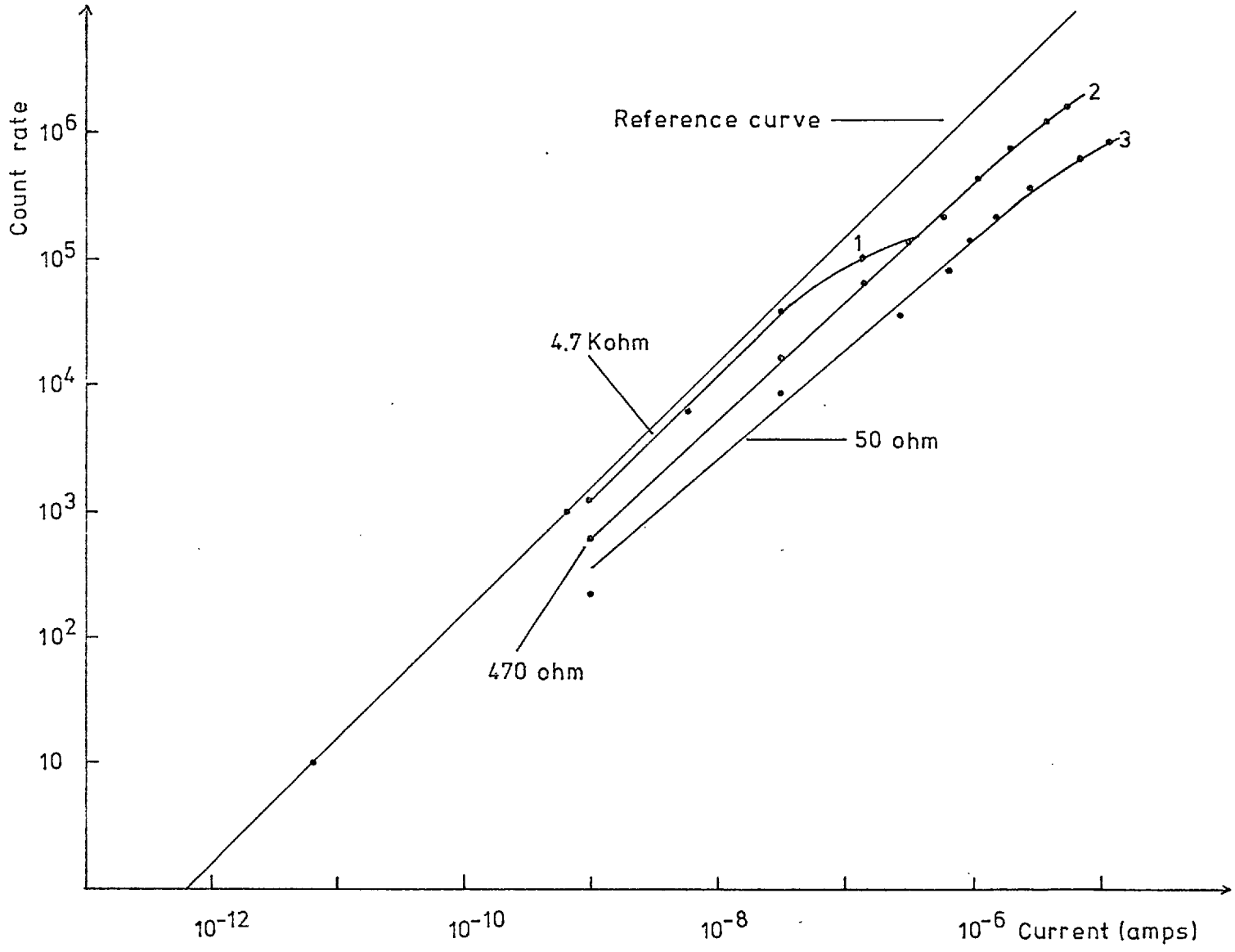


Fig.27. Count rate versus d.c. current curves (amplified system).

to the current. A Tektronix oscilloscope was used to check that no significant baseline shift occurred due to pulse overlap. At a PMT output of 3.10^{-6} A a shift of 5% was measured which was considered insufficient to seriously alter the effective discrimination level, particularly as this current is an order of magnitude above that normally encountered in photon counting experiments.

The experimental curves indicated that the range of linearity and the count rate at a given radiation intensity varied with the load resistor chosen. The curve shapes can be explained on the basis of the known facts about the effect of the values of R_L and C_s (see section 4.7). As R_L is increased the average pulse height increases, so that for a given photon flux more pulses exceed the discriminator level and are therefore counted. However, as the product $R_L C_s$ increases the pulses are stretched and therefore pulse pile-up sets in at a lower radiation intensity. The fact that both curves 2 and 3 tailed off at approximately the same count rate was taken as evidence that in these cases it was the amplifier and not the PMT anode circuit that was responsible for the onset of pulse pile-up.

With the 4.7 K ohm load resistor counting was achieved at 80% of the nominal theoretical value for the tube. The existence of small pulses occurring in the tail of the pulse amplitude distribution (which are too small to exceed the discriminator level) and the presence of d.c. drift currents in the tube makes the separation of the reference and practical count curves inevitable. However, the closeness of the two curves in Fig. 27 indicated that the photon counting system was achieving acceptable counting efficiency. The 50 ohm load was chosen for the following investigations in order that analytical curves extending over a reasonable concentration range could be obtained.

4.5. ANALYTICAL RESULTS OBTAINED WITH THE PHOTON COUNTING SYSTEM.

Before presenting the analytical results obtained with the photon counter the following paragraph is included to indicate how the quoted limits of detection were arrived at. The limit of detection is defined as the concentration or mass of the analyte that yields a signal to noise ratio at the detector, of 2. If analytical signals conformed to Poisson statistics then equation 4.5 could be used to calculate the detection limit directly (background radiation count can be added to the dark count term N_d). Unfortunately analytical signals do not conform to this simple pattern as the results in Table 6 show. Except in the case of the dark count, the measured standard deviations (from thirty consecutive readings) are significantly greater than those predicted by Poisson statistics. The deviation from Poisson statistics reflects the instability of the source due to variations in operating conditions i.e. power, temperature, gas flow, etc. The variance over and above that due to Poisson noise is known as Flicker Noise, although in certain instances other variance terms due to instability in the measuring circuit itself may be important. A full discussion of noise in photon counting experiments is given in chapter V. The results of Table 6 are quoted here to indicate that in determining the detection limit, noise must be measured experimentally from repetitive observations and cannot be calculated directly from equation 4.5.

Table 6. A comparison of Noise Figures determined Experimentally and by Poisson Statistics.

Photon Counting System	Average Count (sec^{-1})	Standard Deviation: Experimental Value	Standard Deviation: Poisson Statistics
Typical Dark Count	468.7	20.33	21.63
Typical Count from Tungsten Lamp	26654	218.9	166.1
Typical Count from Microwave plasma at 228.8 nm	81019	661.4	290.9

4.5.1. Results with the Microwave Plasma System.

Photon counting was used to detect and measure the transient emission signals obtained from the microwave plasma system described in the previous chapter. Cadmium sulphate solutions were employed for the investigation and the emission at 228.8 nm monitored. It was found that a solution containing 0.01 p.p.m. yielded a signal of approximately 250 m.sec duration which increased to 500 m.sec when the concentration reached 1.0 p.p.m. A one second count period was therefore chosen (the counter had pre-set gating times of 10, 1, 0.1 ... 10^{-6} seconds) which enabled the vapourisation process and count period to be manually synchronised without excessive error. The 0.01 p.p.m. solution was then used to optimise the slit width, which was accomplished by measuring signal to noise ratios at various slit widths between 0.02 and 0.15 mm. The optimum was found to be 0.06 mm, compared with 0.1 mm for the d.c. amplifier/integrator.

An analytical curve was then constructed for cadmium, the detection limit for a measured signal to noise ratio of 2 was 2.10^{-13} g (the same as for the d.c. amplifier/integrator)and the linear range extended to 3 p.p.m. corresponding to a count rate of ca 3.10^{5} c.p.s. The photon

counter therefore yielded equal sensitivity to the amplifier/integrator at nearly half the slit width. Indeed had the count period been accurately synchronised with the signal duration, the results by photon counting would have been slightly better than those obtained by capacitative integration. The importance of correct count period timing for transient signals is discussed fully in chapter V, although the simple expression in equation 4.5 shows that amassing unnecessary background counts will degrade the signal to noise ratio. Although photon counting has proved suitable for transient signals of milli-second duration, it would not be successful for short pulses of nano-second duration. Even a very weak pulse of 10 photo-electrons in one nano-second is equivalent to 10^{10} c.p.s. which is far in excess of the linear counting range.

4.5.2. Results with a Non-flame Atomic Fluorescence System.

The non-flame system used for atomic fluorescence measurements is shown in Fig. 28. The device was essentially the same as the microwave plasma system except that excitation was achieved by an EDL, focussed just above the open end of the tube. Cadmium was chosen for the investigation because an intense stable EDL was available and cadmium salts are easily vapourised. The first task was optimisation of the argon flow rate. Samples containing 0.1 p.p.m. Cd were vapourised from the loop and it was found that the largest signal occurred when the flow rate was 1.0 $l.min^{-1}$.

In the absence of spectral interferences the widest possible slit width should result in maximum sensitivity for atomic fluorescence. Practically however, it becomes difficult under these conditions to prevent radiation from the source being reflected directly into the monochromator without passing through the atomic cloud. Furthermore,

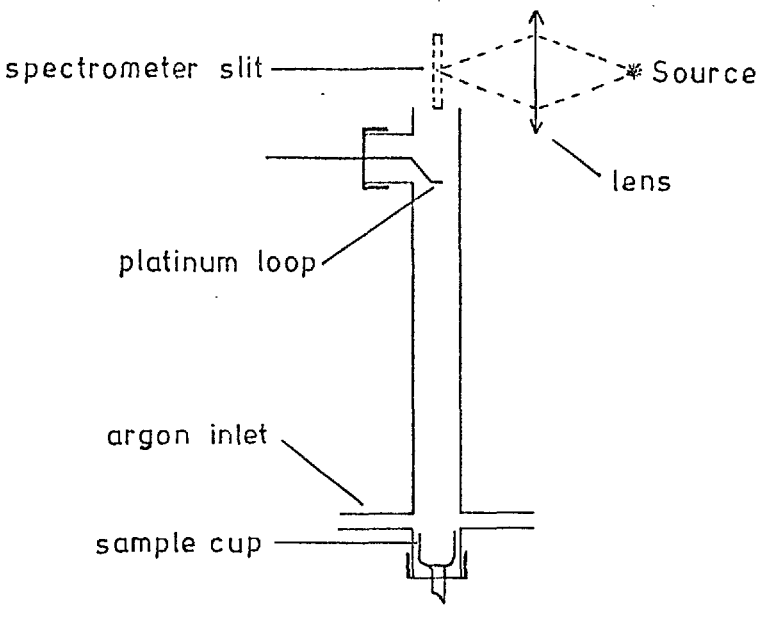


Fig.28. The non-flame atomic fluorescence system.

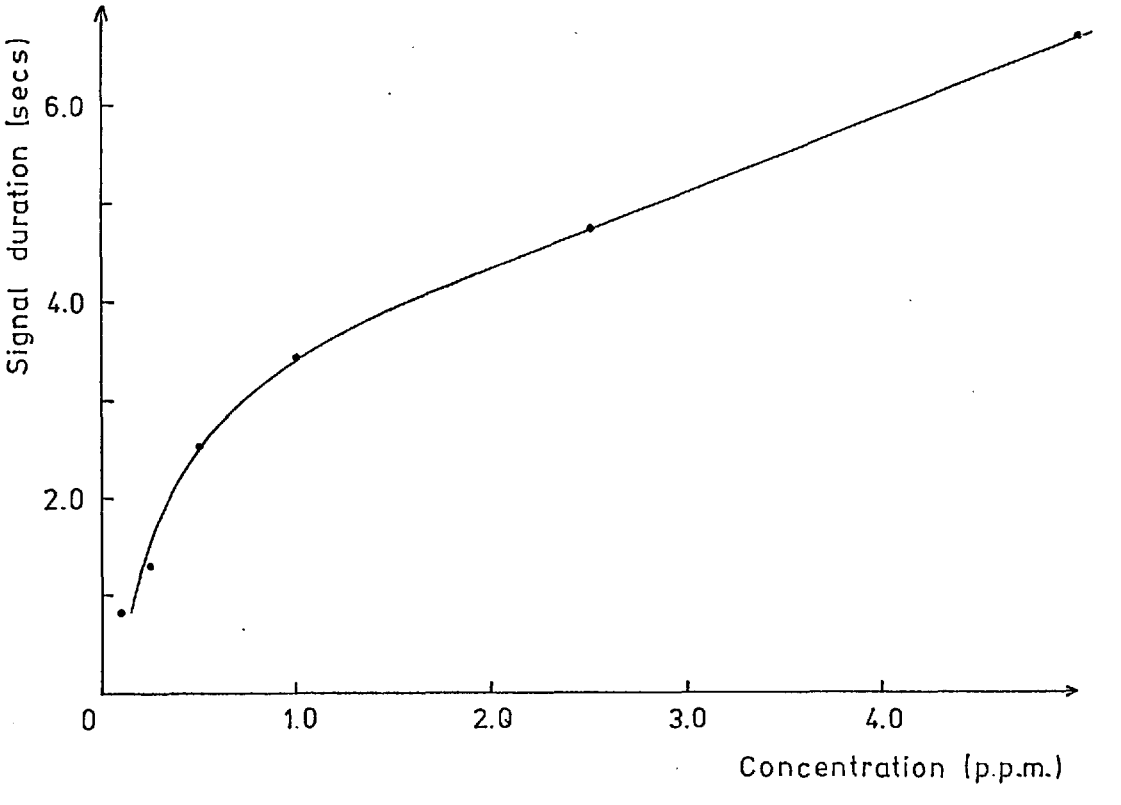


Fig.29. Variation of signal duration with concentration.

because photon counting is limited at high intensity levels by pulse pile-up, working with a high background severely limits the analytical range. Consideration of these two factors resulted in a slit width of 0.1 mm being selected, which gave a background of 4500 c.p.s.

Following optimisation of gas flow and slit width, an investigation of signal duration was carried out in order that a suitable count period be determined. Fig. 29 shows a plot of signal duration versus cadmium concentration. The large range of signal duration was attributed to cadmium vapour being adsorbed on the cell walls and then re-vapourised by radiant heat from the loop. If concentrations above 10 p.p.m. were used, chemical washing of the cell was required to remove a persistent memory effect. From the information in Fig. 29 . it was decided to employ a one second count period for concentrations of less then 0.1 p.p.m. and a ten second count period for concentrations above this level.

Analytical curves for cadmium were then constructed by both photon counting and d.c. measurement, these curves are shown in Fig. 30 . The detection limit by photon counting was 2.10^{-13} g and by d.c. measurement 10^{-12} g. Furthermore, the photon counting curve was linear up to ca 0.5 p.p.m. whereas the d.c. curve exhibited a distinct change of slope. Thus integration of the signal yielded both higher sensitivity and greater linearity of the calibration curve. The deviation from linearity of the d.c. curve resulted from distortion of the signal pulse shape by the time constant of the d.c. circuit (RC = 0.7 seconds). Indeed when the analytical pulse shape is non-reproducible or varies with concentration, integration provides the only method of precise signal measurement.

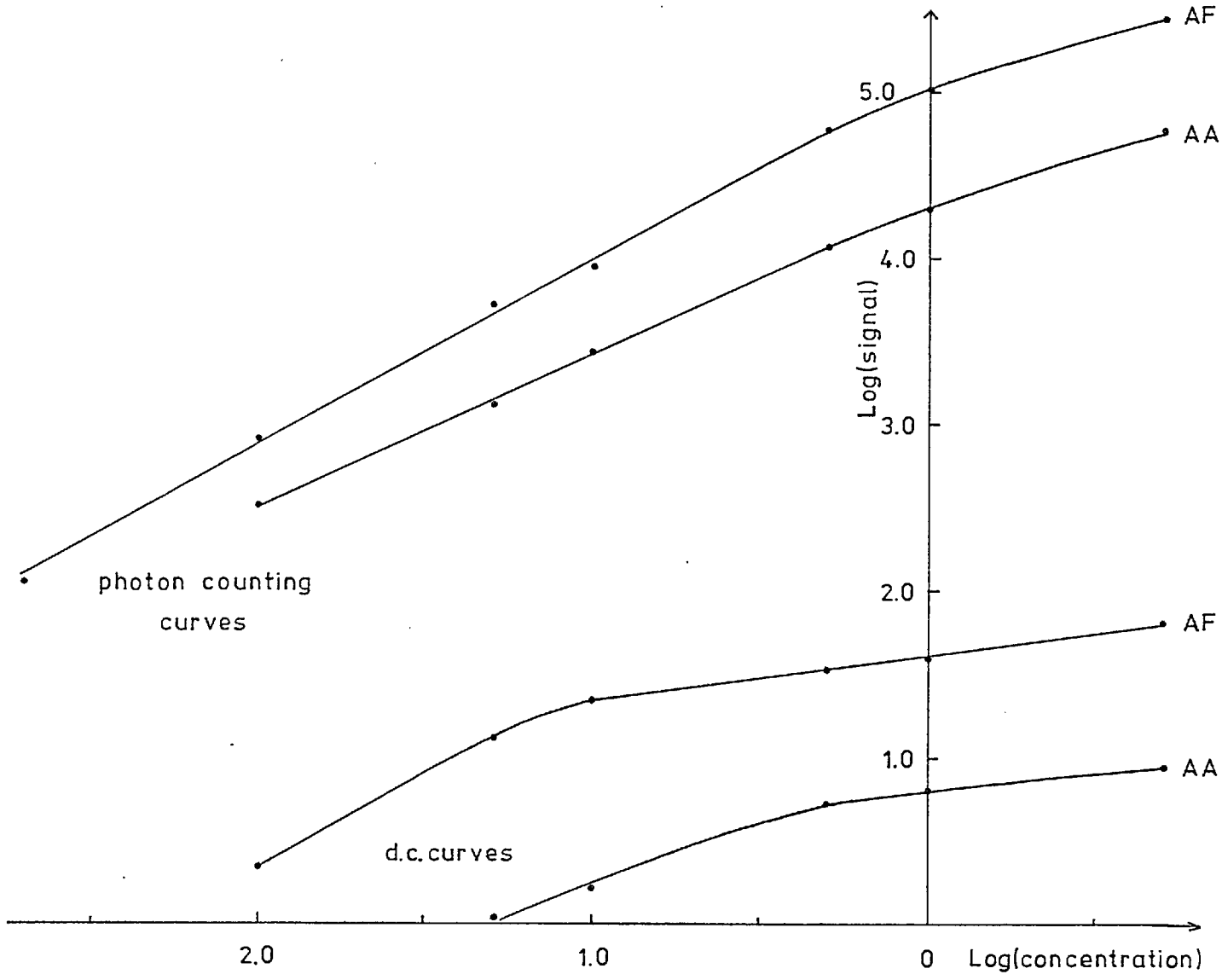


Fig. 30. Analytical curves by photon counting and d.c. measurement.

4.5.3. Results with a Non-flame Atomic Absorption System.

The apparatus used was the same as that described in the previous section for AF, except that a hollow cathode lamp instead of an EDL was used for excitation. The cadmium HCL was powered by the lamp supply of a Perkin Elmer 290 atomic absorption instrument and was therefore modulated at 50 Hz. This was of no consequence for photon counting detection where integration over 50 and 500 cycles was being taken, however the time constant of the d.c. system was insufficient to completely integrate the modulation with the result that a small ripple appeared on the signal.

Optimisation of the slit width required different criteria from those for AE and AF. In AA it is generally the absorption (α) that is measured i.e.

$$\frac{1}{\alpha} = \frac{I_o}{I} \qquad \ldots.4.7.$$

where I_o is the intensity of the incident beam

and I is the intensity of the transmitted beam

Writing equation 4.7 in terms of the count rate and including the count period yields:-

$$\frac{1}{\alpha} = \frac{N_o t}{Nt}$$

where N_o is the count rate of the incident beam

N is the count rate of the transmitted beam

t is the count period

Now the propagation of statistical error in $(1/\alpha)$ is given by:-

$$\left(\frac{\sigma_{1/\alpha}}{1/\alpha}\right)^2 = \left(\frac{\sigma_{N_o t}}{N_o t}\right)^2 + \left(\frac{\sigma_{Nt}}{Nt}\right)^2 \qquad \ldots.4.8.$$

where σ is the standard deviation

In general σ does not increase at the same rate as the count rate ($\sigma \propto (N)^{\frac{1}{2}}$ for Poisson signals) and therefore the precision in $(1/\alpha)$ is increased by making N_o as large as possible or by increasing the count period. Equation 4.8 relates only to steady signals because for transient signals N is an unknown function of time. However the terms Nt and $N_o t$ in equation 4.8 can be replaced by expressions of the type:-

$$Nt = \int_0^{\tau} N(t).dt = N_o\tau - N_a$$

and $$N_o t = N_o \tau$$

where τ is the integration period which depends on the concentration

and N_a is the total number of photons absorbed.

Thus the slit width was adjusted so that N_o was approximately 2.10^5 c.p.s., the upper limit to N_o being set by the onset of pulse pile-up. Having chosen N_o, pulse pile-up is not a problem associated with AA because during the signal period the number of photons arriving at the detector is actually decreased.

Two calibration curves for AA, by photon counting and d.c. measurement are shown in Fig. 30. In each case the absorbed intensity i.e. N_a rather than the absorption was plotted, so that the ordinate axis for the photon counting results could be plotted directly as counts absorbed. Once again the use of photon counting demonstrated the ability of the integration technique to yield precise measurements on variable signal profiles. The detection limits were photon counting 10^{-12} g and d.c. measurement 5.10^{-12} g.

4.5.4. Results with a Cool Flame Atomic Fluorescence System.

In this study the atomic fluorescence from mercury nebulised into a slightly fuel rich, pre-mixed air-propane flame was measured. A mercury EDL was employed to excite emission from the Hg 253.7 inter-

combination line. The slit width yielding the maximum signal to noise ratio was determined independently for both photon counting and d.c. techniques. For d.c. the optimum slit width was found to be 0.25 mm and for photon counting 0.05 mm.

Calibration curves were then constructed for each technique, the points representing the average of five readings taken at each concentration (one second count periods). The results from the curves are summarised in Table 7 . Once again photon counting yielded a slightly improved detection limit at a greatly reduced slit width and a much lower linear working range.

Table 7 . Comparison of Photon Counting with d.c. Measurement in Atomic Fluorescence.

Measurement technique	Slit Width (mm)	Detection limit (p.p.m.)	Linear Range (p.p.m.)
d.c.	0.25	1.0	1.0 - 300
photon counting	0.05	0.5	0.5 - 50

4.5.5. Results with a Cool Flame Atomic Emission System.

A comparison of the two detection systems was carried out for the thermal emission of sodium in the air-propane flame, at the unresolved 589.0;589.6 nm doublet. The results are summarised in Table 8 where it can be seen that photon counting yielded a significantly lower limit of detection than d.c. at 1/25th of the slit width. However, pulse pile-up once again severely limited the linear working range.

Table 8 . Comparison of Photon Counting with d.c. Measurement in Atomic Emission.

Measurement technique	Slit Width (mm)	Detection limit (p.p.m.)	Linear Range (p.p.m.)
d.c.	0.75	0.05	0.05 - 6.0
photon counting	0.03	0.005	0.005- 0.4

4.5.6. Summary of Results.

The results obtained in the previous sections enable certain conclusions to be drawn about the application of photon counting to analytical spectrometry. The sensitivity obtained with photon counting was excellent, particularly for the low background non-flame AF system and the flame AE system where the background was effectively reduced by the narrow slit width, (line intensity approximately $\propto$ slit width, background intensity approximately $\propto$ (slit width)^2). The L'Vov theory (23) demonstrates clearly that integral techniques should yield greater sensitivity but the effect of background is not taken into account. Certainly excessive background degrades the signal to noise ratio (see equation 4.5 and chapter V), limits the linear counting range and when caused by a large spectral band pass may be associated with spectral interference. The degradation of signal to noise ratio by background radiation can be reduced in AA and AF (steady state signals) by the use of a.c. techniques, and therefore it is to be expected that photon counting will yield maximum sensitivity only for low background devices e.g. non-flame AF or where signal modulation is not possible e.g. AE.

The situation for transient signals particularly those of variable profile is somewhat different, because integration may be the only method of producing linear calibration curves. A fully optimised photon counter should yield better results than capacitative integration because the technique is not prone to drift. However, unlike with the d.c. amplifier/integrator it is not possible to back-off background radiation in photon counting, so that once again high background systems may severely limit both sensitivity and linearity of the counting technique. AA is a high radiation level technique but because no problem with pulse

pile-up occurs, photon counting can provide a useful method of integrating the negative ordinate signal profile derived from AA.

4.6. AN IMPROVED AND SIMPLIFIED PHOTON COUNTER.

4.6.1. Equipment and Performance.

The photon counter described previously performed satisfactorily, but appeared to be limited both in dark count and linear range by the amplifier. It was therefore decided to ascertain whether or not pulse amplification was in fact necessary. In the absence of a pulse height analyser, measurement of pulse heights was accomplished with a Tektronix 547 oscilloscope fitted with a dual trace plug in amplifier (type 1A1) and a 10 M ohm, 7 pF, x 10 probe (type P6008). The probe was attached directly to the end of the nine inch PMT output cable. The statistical variation in pulse heights made it difficult to estimate their magnitude precisely and therefore three estimates were made at each value of R_L (see Table 9). The results obtained with the 1 K ohm load indicated that photon counting without the amplifier was possible, provided that the discriminator was set near to its minimum value. A count rate versus d.c. current curve was constructed with the discriminator set to its minimum value of 10 mV, and it was found that both increased ordinate values and an extended linear range (up to 5.10^5 c.p.s.) were obtained for the 9601B PMT.

Table 9 . Estimated Photomultiplier Pulse Heights.

Photomultiplier	Anode Load Resistor (ohms)	Approx. Minimum Pulse Height (mV)	Maximum Observed Pulse Height (mV)	Most Probable Pulse Height (mV)
EMI 9601B	50	5	5	5
	1K	60	110	75
EMI 6256S	50	10	30	18
	1K	100	250	135

The measurements made on the 9601B encouraged the building of a new photon counter, based on the principal of counting PMT anode pulses, without further amplification. A Hilger Watts D330 monochromator was chosen, because for this instrument the PMT is mounted externally in a housing bolted to the exit slit mounting. This enabled easy cooling of the PMT and furthermore the cable linking the PMT to the frequency meter could be reduced to 6 inches. The PMT selected was an EMI 6256S, having 13 venetian blind dynodes yielding a gain of 4.10^7 at 1.22 KV, an S-type photo-cathode (specially processed for low thermionic emission) and an anode pulse width of 15 nS. It was anticipated that the high gain, narrow pulse width and low background rating of this tube would make it ideal for photon counting.

Pulse height measurements were made on the 6256S tube for loads of 50 and 1 K ohm (measured stray capacity 40.82 pF). The results are shown in Table 9 and indicate that the higher gain of this tube yielded ample pulse amplitudes to trigger the 10 mV counting threshold of the frequency meter. The reported function of the discriminator (104, 108) is to selectively exclude dark pulses from the count register and therefore improve the signal to noise ratio. It will be demonstrated later in this chapter, that because the majority of dark pulses (i.e. pulses of thermionic origin) have exactly the same pulse height distribution as the photo-electron pulses, this form of discrimination is only applicable to detecting extremely low photon fluxes and is unlikely to be of importance in analytical spectrometry. However, recent studies (107) have shown that the discriminator (lower level) can be employed to extend the linear counting range, by clipping the base of the pulses and thereby reducing their effective width. For analytical spectrometry this is a far more valid application

of discrimination than attempting to increase the signal to noise ratio. The optimum discrimination level for extending the linear range was found to occur when approximately half of the photo-electron pulses were rejected. It must be noted, that under these conditions the sensitivity of the photon counter is reduced and will not therefore yield the lowest possible detection limits. For this reason it was decided to employ the minimum discrimination level (i.e. 10 mV) in the following studies, and attempt to count all the photo-electron pulses.

Fig. 31 shows three count rate versus current curves for the 6256S tube, with three different load resistors. The effect of the value of R_L on the onset of pulse pile-up is clearly demonstrated. It has been found (108) that for most PMTs the single photon anode pulse height distribution covers a range of ten fold and therefore the average pulse height must be well in excess of the discriminator level, if all the pulses are to be counted. The coincidence of the 1 K and 10 K ohm curves in Fig. 31 was taken as evidence that all photo-electron pulses, including most of the very small ones were being recorded by the counter. The lower position of the 50 ohm curve indicated that some of the pulses were below the 10 mV level and were therefore not being counted. Comparison of the 1 K ohm curve with the reference curve, shows that counting was achieved at 81.3% of the theoretical rate and therefore the 1 K ohm load was used in all subsequent experiments.

4.6.2. The Effect of Cooling the Photomultiplier.

The background count for the system at 22 ° C was ca 1200 c.p.s. and once again conformed to Poisson statistics having a standard deviation of ca 37. Cooling of the PMT was accomplished by surrounding

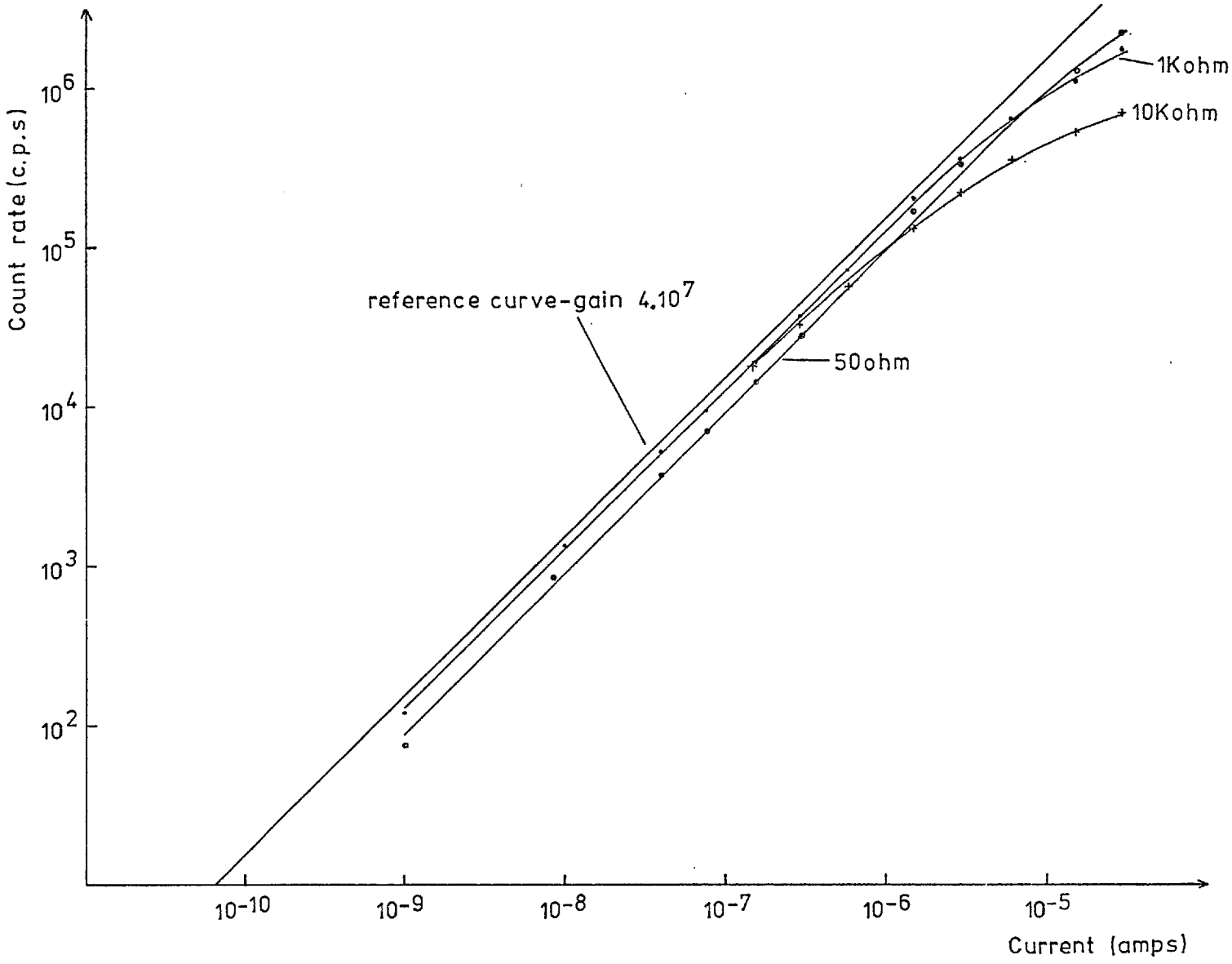


Fig.31. Count rate versus d.c. current curves for the EMI 6256S PMT.

the tube housing with a thermally insulated box, which was packed with solid CO_2. The PMT was mounted between foam rubber strips, inside a mu-metal shield and each pin was connected by a short flexible wire to the dynode chain potential divider. These precautions were necessary to aviod damage, due to thermal contraction of the tube envelope. Furthermore, the housing was packed with silica gel and the monochromator flushed with dry nitrogen to avoid condensation problems.

The effect of cooling on dark count is shown in Fig. 32, where it can be seen that a drastic reduction in dark count was achieved. After allowing one hour for thermal equilibration, the count from the tube was reduced to 30 counts per ten seconds with a measured standard deviation of 4.5. This represented a reduction in dark count noise of 30 times, compared with the uncooled tube. The minimum detectable Poisson signal therefore, assuming a 16% quantum efficiency and a 10 second count period is 10 photons per second, which corresponds to an extremely low radiation level.

Operation of the tube at low dark count rates showed that occasional bursts of counts occurred. These were attributed to radioactive sources, electrical pick-up from RF sources and mains spikes. The addition of an upper discriminator level to the system may well have removed most of these multi-count events. However, because experiments in analytical spectrometry usually involve background radiation levels of several 1000 c.p.s., cooling of the tube effectively reduced the dark count noise contribution to zero.

4.6.3. Application to Atomic Fluorescence Spectrometry.

The atomic fluorescence of mercury was studied, free atoms being produced by nebulising solutions of $HgCl_2$ into a hydrogen-argon diffusion flame. The flame was burned on a circular burner fitted to

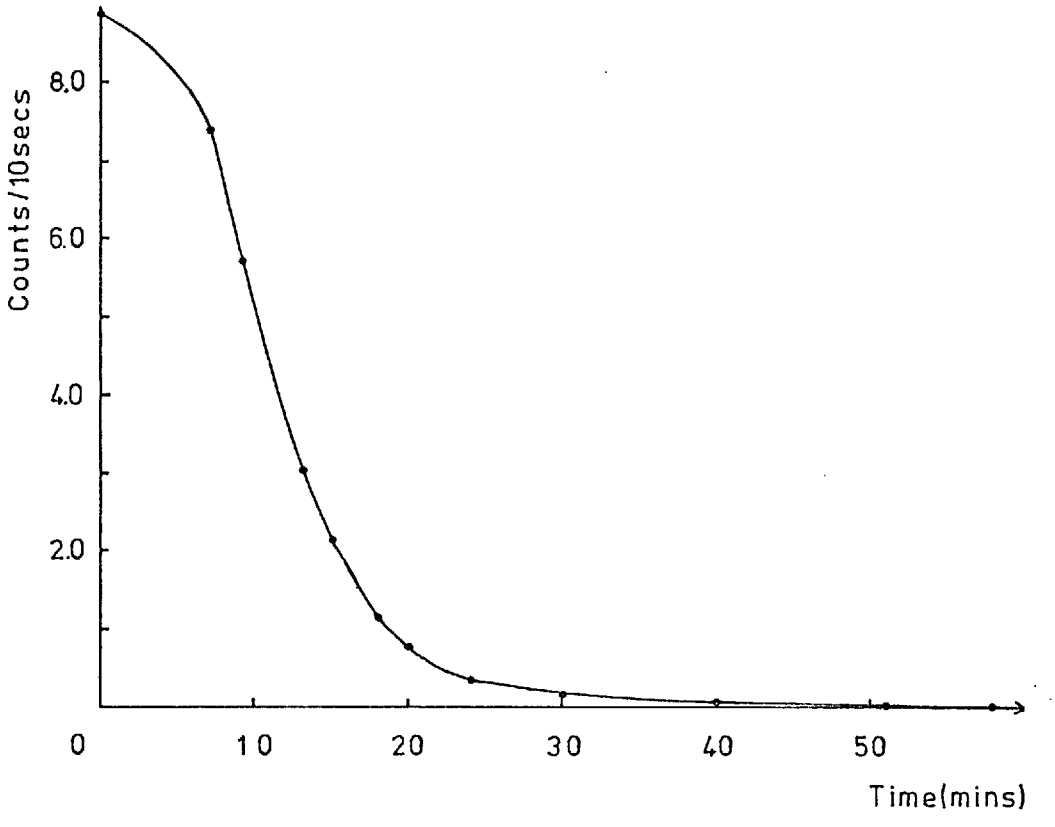


Fig.32. Effect on dark count of cooling the PMT.

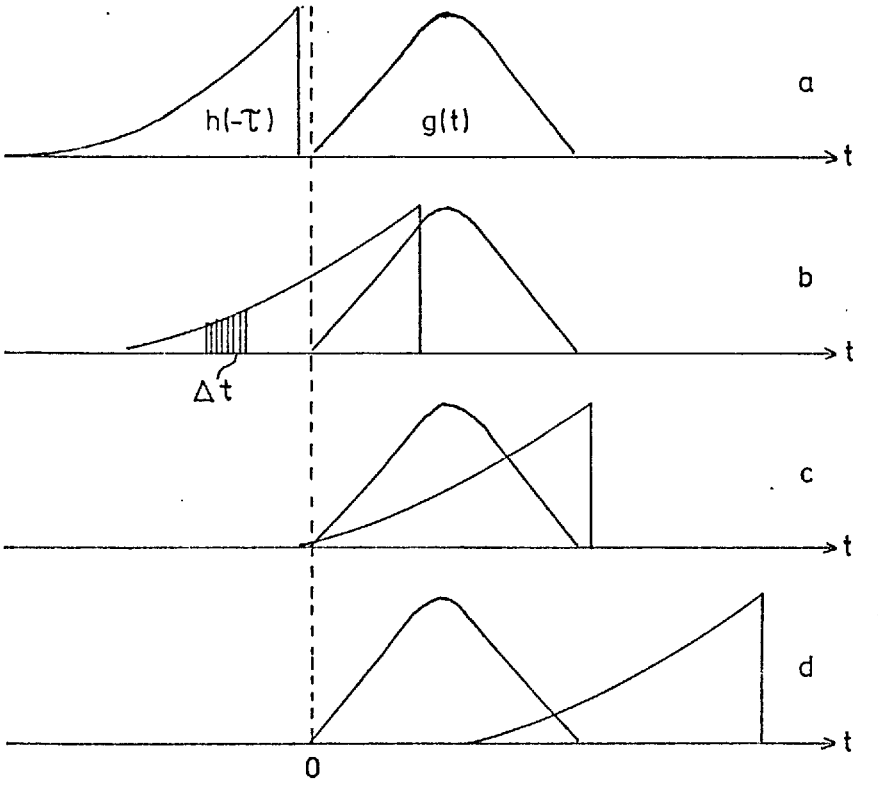


Fig.33. The convolution process.

the nebuliser of a Perkin Elmer 290B AA spectrometer; flow rates were H_2, 8.0 $l.min^{-1}$ at 3 p.s.i. and Ar, 4.0 $l.min^{-1}$ at 30 p.s.i. Excitation was achieved by focussing the radiation from a mercury EDL into the centre of the flame, 4 cm above the burner head. Fluorescence radiation was allowed to fall directly on the slit of the D330, which was set to pass the 253.7 nm intercombination line.

D.c. measurements - for comparison purposes - were made in the usual manner, with the PMT output loaded with 20 K ohms and the resulting voltage displayed on a Servoscribe potentiometric recorder. The optimum slit width of 0.1 mm (entrance and exit slits) was determined by spraying solutions containing 25 p.p.m. Hg into the flame and noting the slit width at which the maximum signal to noise ratio occurred.

An analytical working curve was recorded by d.c. measurement for concentrations of 1.0 - 1000 p.p.m. and was found to be linear over this range. The detection limit was 0.5 p.p.m. Cooling of the PMT reduced the measurable d.c. dark current noise to zero, but produced no observable decrease in the noise on the analytical signal.

Measurements made in the counting mode showed that at the 0.1 mm slit width, the count rate due to flame radiation, scattered source radiation and dark count amounted to 60,045 c.p. 10 s. This was considered to be an acceptable background and therefore the 0.1 mm slit width was also employed for the photon counting measurements. An AF working curve for Hg was constructed by taking the average of five 10 second counts at each concentration. The measured detection limit was 0.1 p.p.m. and the linear range 0.1 to 200 p.p.m. Thus as expected both the detection limit and the linear counting range were lower by photon counting.

Experiments were then performed to determine the effect on signal to noise ratio of cooling the tube. The results are shown in Table 10 and were obtained by taking 30 repetitive 10 second counts at each slit width, standard deviations being calculated from the normal formula viz:-

$$\text{noise} = \sigma = \left(\frac{\sum_{i}^{n} (x_i - x)^2}{n - 1} \right)^{\frac{1}{2}} \qquad \ldots.4.9.$$

where x_i is the value of the i_{th} reading

x is the mean or average signal

n is the number of readings taken.

Table 10. Signal to Noise Comparison for a Cooled and Uncooled Photomultiplier.

Slit Width (nm)	Concentration of Mercury (p.p.m.)	Signal to Noise Ratio Uncooled Tube	Signal to Noise Ratio Cooled Tube
0.1	1.0	9.9	19.4
0.01	5.0	12.4	23.3

Thus a signal to noise increase of two was achieved in each case, arising directly from the expected 30 fold reduction in the noise contribution of the dark count. It is to be expected that in high background radiation systems, cooling of the tube will be less advantageous, because the noise contribution of the dark count is then relatively small. However, the background as well as the signal are integrated by photon counting, and therefore effective reduction of the background yields a greater improvement in signal to noise ratio than for d.c. measurement.

4.6.4. Application to Atomic Absorption Spectrometry.

The experimental apparatus with regard to flame, nebuliser and counting system was the same as that for atomic fluorescence. In this case however, cadmium was studied, excitation of the 228.8 nm line

being achieved by a HCL operated at 3 mA from the lamp supply of a Perkin Elmer 290. AA spectrometer (50 Hz modulated). Radiation from the lamp was focussed into the centre of the flame 4 cm above the burner head and then refocussed at the entrance slit of the monochromator. All AA measurements were made with the PMT cooled by solid CO_2.

D.c. measurements made for comparison purposes were taken with the PMT output loaded with 100 K ohms and the recorder gain set so that the chart represented 0 - 100% absorption. Equation 4.8 applies equally well to d.c. conditions (when count rates are replaced by currents) and therefore the slit width was adjusted so that the reference beam yielded an output current of 10 micro amps, which was large but not sufficient to cause excessive dark current generation (due to thermionic emission) by the photo-cathode. This output current corresponded to a slit width of 0.05 mm. A working curve (absorption versus concentration) was constructed by d.c. measurement for concentrations of 0.05 - 10 p.p.m. Cd; the detection limit was 0.05 p.p.m. and the linear range 0.05 - 4.0 p.p.m. The concentration range studied was limited by the difficulty of making precise measurements at high absorption values (10 p.p.m. $\equiv$ 83% absorption), on a simple d.c. system. Modulation of the HCL resulted in a slight ripple on the d.c. signal but it was insufficient to seriously degrade the signal to noise ratio.

Photon counting measurements were made with the slit width adjusted so that at the longest counter gating time, the count nearly filled the 6-digit register. The reference beam count was therefore $8.97.10^5$ c.p. 10 s. which corresponded to a slit width of 0.03 mm. An analytical curve constructed by photon counting yielded a detection limit of 0.02 p.p.m. Cd and a linear range of 0.02 - 30.0 p.p.m. The lamp modulation was of no consequence in photon counting, indeed 30

consecutive 10 second counts of the reference beam yielded a relative standard deviation (i.e. 100 $\sigma / \bar{x}$) of 0.32%, which indicated that in terms of a 10 second count period the integrated output from the lamp was extremely stable. This stability was undoubtedly responsible for the improved detection limit and in the absence of pulse pile-up, photon counting also yielded an acceptable linear range.

4.7. A THEORETICAL ANALYSIS OF PHOTO-ELECTRON PULSE DISTORTION BY THE PHOTOMULTIPLIER ANODE NETWORK.

The results obtained with the two practical photon counting systems demonstrated the importance of pulse distortion by the PMT anode circuit. Recent work (109) has shown that pulse base clipping can extend the linear range of photon counting, and it is fairly certain that with the development of the technique more attention will be paid to the detailed shape of the photo-electron anode pulse. It was therefore decided to carry out an analysis of pulse shaping by the parallel RC anode network.

The analysis could have been performed in either the frequency domain or the time domain, but for individual pulses having a fairly complex frequency spectrum e.g. Gaussion pulses time domain analysis is usually easier. This was achieved by application of the convolution integral (109) which can be expressed in the form:-

$$i(t) = \int_0^t h(t - \tau)g(\tau)d\tau \qquad \ldots.4.10$$

where $i(t)$ is the output at time t

$h(t)$ is the circuit impulse response

$g(t)$ is the exciting pulse function

and τ is a dummy integration variable.

The impulse response of the circuit describes the output as a function of time following excitation by a δ function. The δ function

is defined as a pulse of infinitely narrow width enclosing unit area. For a parallel RC circuit, excitation by a current δ function yields an initial voltage of 1/C, which then decays according to the function exp -(t/RC). The physical significance of the Convolution Integral can now be described with the aid of the diagrams in Fig. 33. First the excitation function g(t) is plotted as a function of the new variable τ. The impulse response is plotted as a function of the variable $(-\tau)$ and is then slid along the abscissa to some point t, initially allowing t to be negative (which corresponds to the pulse not having reached the circuit Fig.33a). At all negative values of t there is no overlap of the two waveforms and therefore the output is zero. Once t becomes positive (Fig.33b) overlap does occur and the multiplication of ordinates yields a new curve. The output at the time t is then given by the area under the new curve integrated up to the point t.

Substituting the appropriate functions into equation 4.10 yields

$$i(t) = \int_0^t \frac{1}{C_s} \exp -\left(\frac{t-\tau}{R_L C_s}\right) \cdot \frac{Ge}{\sigma(2\pi)^{\frac{1}{2}}} \exp -\left(\frac{\tau^2}{2\sigma^2}\right) d\tau \quad \ldots.4.11.$$

Rearrangement can reduce equation 4.11 to a simple Gaussion integral of the type

$$i(t) = K \int_0^t \exp\left(f(t)\right) . \exp\ (-\gamma^2/C)\ d\gamma$$

where K and C are constants.

However, analytical solutions for finite ranges of t are not possible (tabulated values can be used) and furthermore the function has positive ordinate values in the abscissa range $-\infty$ to $+\infty$, which does not correspond to a real pulse where $f(t) = 0$ for $t \leqslant 0$.

Equation 4.11 was therefore solved numerically using the Imperial College C.D.C. 6400 computer, which enabled problems arising from the

finite pulse length to be avoided by application of a cut-off procedure. The first step in writing the program was to convert equation 4.11 into numerical form so that the answer could be given by a summation rather than an integral. This was accomplished by dividing each continuous function into a series of vertical segments (as in Fig.33b) each having a width Δt and an assumed constant ordinate in the range Δt (the method of choosing the value of Δt is given later in this section). Thus ordinate values for the functions $g(t)$ and $h(t)$ were calculated for a range of abcissa values and the answers placed in two arrays names EXCIT(I) and RESPO(K) respectively. For the Gaussian pulses the maximum value of t was decided on the basis of the area under the computed curve relative to a full curve, typically values of 90 and 95% were employed. The range of t for the impulse response was calculated on the basis of the ordinate value decreasing to 5% of its initial value i.e. $t/RC = 3$.

Having established the two arrays, the next step was to scan the RESPO(K) array through the EXCIT(I) array and at each new value of t (i.e. overlap) multiply ordinates point by point to produce a new curve. The ordinates of the new curve were placed in an array named CURVE(KK), and then the output at time t calculated by summing segments under CURVE(KK) up to the point t, the answer being placed in a final array CONVO(J). The operation can be described by writing three generating functions which are not strict mathematical expressions, but a formal statement of the solution for each overlap condition i.e. Fig. 33 b,c and d.

Let N be a running index

JK the number of segments in the EXCIT(I) array

and NK the number of segments in the RESPO(K) array.

For overlap condition (b)

$$CONVO(N) = \sum_{I}^{N} \left(RESPO(K)_{1}^{N} \cdot EXCIT(I)_{N}^{1} \right)_{N=1}^{JK} \quad \ldots.4.12.$$

Thus the first two terms i.e. outputs are:-

$$CONVO(1) = RESPO(1) \cdot EXCIT(1)$$

$$CONVO(2) = RESPO(1) \cdot EXCIT(2) + RESPO(2) \cdot EXCIT(1)$$

For overlap condition (c)

$$CONVO(N + JK) = \sum_{I}^{JK} \left(RESPO(K)_{N+1}^{N+JK} \cdot EXCIT(I)_{JK}^{1} \right)_{N=1}^{NK-JK} \quad \ldots.4.13.$$

and for overlap condition (d)

$$CONVO(N + NK) = \sum_{JK-1}^{JK-N} \left(RESPO(K)_{NK-JK+(N+1)}^{NK} \cdot EXCIT(I)_{JK}^{N+1} \right)_{N=1}^{JK-1} \quad \ldots.4.14.$$

These functions are written for the special case when NK > JK, but in the program provision was made for reversing indices so that calculation was performed equally well when JK > NK. A full transcript of the program is given in Appendix II.

Initial testing was carried out by convoluting the impulse response of the anode circuit, (R_L = 1 K ohm; C_s = 40.87 pF) with a square excitation pulse having the same width and total area (i.e. charge) as the PMT Gaussian pulses. The square pulse problem has a simple analytical solution that was used to calculate pulse distortion curves, which were then checked against curves computed by the program. It was found that provided Δ t was kept to 0.3 nS or less, the peak ordinate values of the two output curves did not differ by more than 3 mV. The same criterion was therefore used in deciding Δ t values for convolution of the Gaussian pulses.

Using the following constants C_s = 40.32 pF, Ge = $6.4.10^{-12}$ coulombs and σ = 6.356 nS the pulse shapes shown in Fig. 34 were computed for values of R_L from 50 to 2.2 K ohms. Allowing for measurement errors and inevitable uncertainties in the various system parameters,

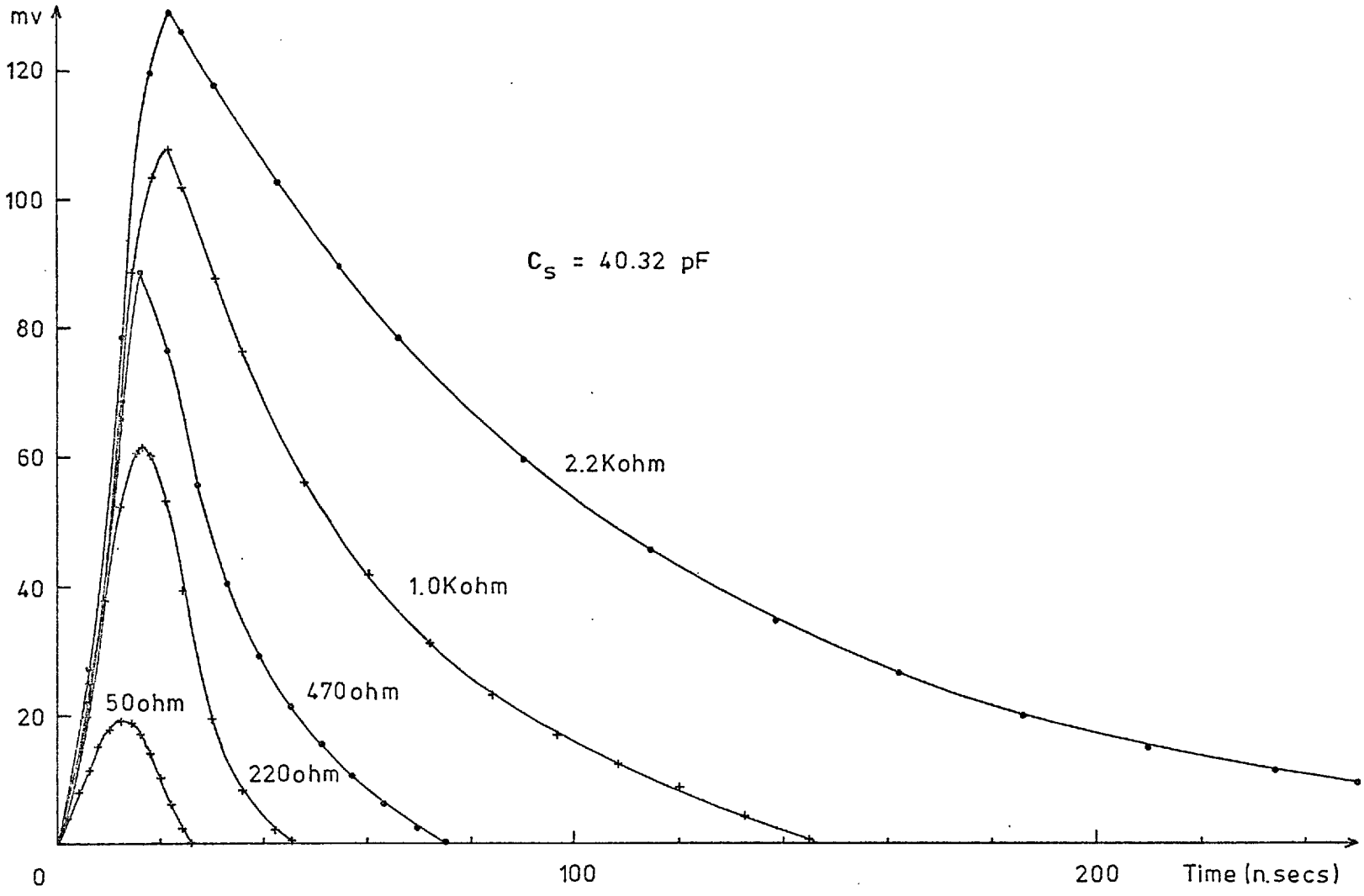


Fig.34. Computed pulse shapes for various values of R_L.

the computed pulse amplitudes agree quite well with those measured practically. The curves demonstrate clearly that increasing R_L increases both pulse height and pulse width. This is confirmation of the explanation given for the curvature of the count rate versus d.c. current curves. Furthermore, when $R_L C_s$ is large compared with 2.36σ e.g. $R_L C_s$ = 88.7 nS for R_L = 2.2 K ohm, the pulse shape is almost entirely that due to the RC network having an exponential growth and decay. However, when $R_L C_s$ is small compared with 2.36σ e.g. $R_L C_s$ = 2.0 nS for R_L = 50 ohm, the Gaussian shape and half width of the photo-electron anode pulses is preserved. Examination of eqation 4.14 and the curves in Fig. 34 shows that the total width of the resulting pulse is approximately equal to the sum of the widths of the convoluted pulses.

The pulse shapes drawn in Fig. 35 demonstrate the expected result (from inspection of equation 4.11) that the pulse half width is a function of σ and $R_L C_s$ only and therefore combinations of R_L = 500 ohms, C_s = 80.64 pF and R_L = 1K ohm, C_s = 40.32 pF yield the same half width, although the pulse amplitudes are different. Comparing the 1 K ohm curves in Fig. 35 shows that reducing the stray capacity in the ratio 3/8 practically doubles the pulse height, whereas it can be seen in Fig. 34 that a ten-fold change in R_L from 220 to 2.2 K ohms was required to produce the same result. This occurs because an extra capacity term of $1/C_s$ appears on the right hand side of equation 4.11. Thus in photon counting systems the optimum arrangement is to keep C_s as small as possible and then to increase R_L to yield sufficient pulse amplitude to trigger the counting circuits.

Making the assumption that by correct wiring technique the total stray capacity at the output of the tube housing could be reduced to

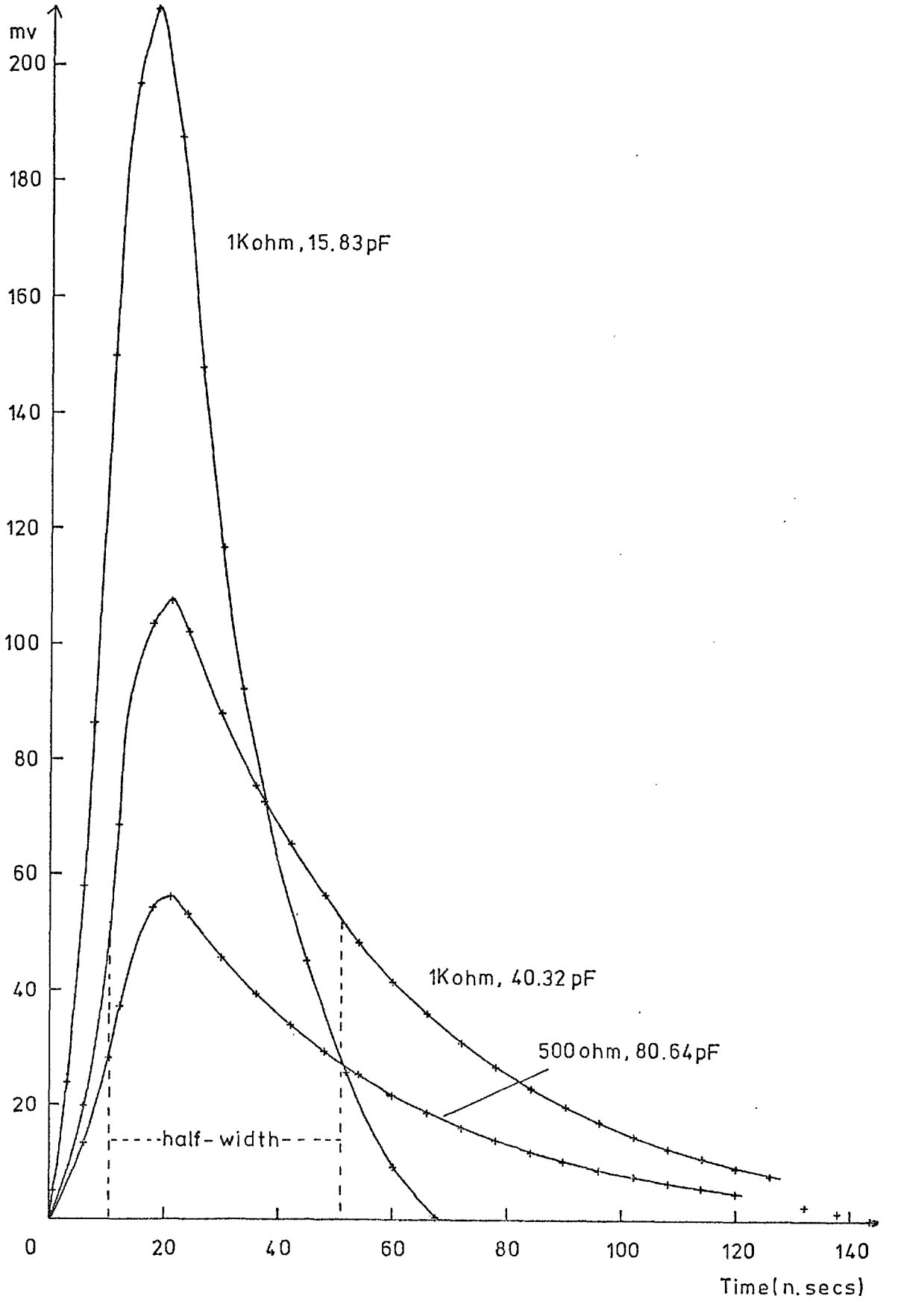


Fig.35. Computed pulse shapes for different values of R_L and C_s.

10 pF (EMI specify an anode to all dynode capacity of 8 pF), the program was employed to determine the minimum value of R_L required to yield pulse amplitudes sufficient to trigger the 10 mV level of the counter. Remembering that pulse amplitudes from the PMT may vary by a factor of 10, the minimum acceptable mean pulse amplitudes was taken as 100 mV. It was found that a load of 300 ohms gave a pulse half width of 15.8 nS and a pulse height of 112 mV. This would be ideal because the pulse width of the PMT is almost entirely preserved.

Transmission of this pulse to the counter without further distortion could be achieved by use of a matched line. The matched line (110) has a frequency band-width approaching infinity, which in time domain analysis is equivalent to the line having zero time constant. Thus by placing a 600 ohm load at the PMT anode and another at the counter input, the two could be joined by a 600 ohm line with the result that the net load on the PMT would be 300 ohms and no pulse distortion would occur. Unfortunately 600 ohm lines are uncommon, most cables currently in use being of the 50 ohm type. Matching to a 50 ohm line could be achieved by a simple impedance converter device (e.g. an emitter follower) mounted at the base of the tube and having a small gain of about x 10 to compensate for loss of pulse amplitude.

4.8. CONCLUSIONS.

The results presented in this chapter demonstrate that photon counting is a promising new technique for signal measurement in analytical spectrometry. The major disadvantage is the limited linear counting range, however this will be greatly improved in the future with advances in PMT and digital circuit design. Generally it can be concluded that photon counting is likely to be the preferred technique in low background systems, or where integration is essential because of

variable signal profile.

The fundamentals of circuit design have been investigated in order to identify limiting factors and to determine methods of system improvement. The concept of noise in counting measurements has been introduced and techniques of limiting noise, generated internally by the counting system described. In the final chapter the importance of signal noise in relation to photon counting will be considered and some further practical results analysed.

oooOOOooo

CHAPTER V

THE ANALYSIS OF NOISE IN PHOTON COUNTING

5.1. INTRODUCTION.

The practical advantages and disadvantages of photon counting have been demonstrated by the results presented in the previous chapter. It is now necessary to consider further the reasons why photon counting is more suitable in certain radiation conditions and to ascertain the factors limiting the measured signal to noise ratio. The concept of noise has been introduced but the equations related to 'Poisson noise' (i.e. the noise associated with Poisson signals), which was found to apply rigorously only to system dark count. It has been shown, that dark count noise can effectively be reduced to zero and therefore the limiting noise in most experiments is derived not from the measuring circuits but from the signal itself.

The first part of this chapter will identify the sources of noise likely to be of importance in photon counting and where possible express each noise component in terms of the count rate. For comparison purposes, noise in d.c. systems will also be considered and the results of a theoretical comparison between d.c. measurement and photon counting, recently presented by Ingle and Crouch (111), reviewed. Expressions for total noise will than be developed and the effect of integration period on signal to noise ratio investigated.

The chapter will be concluded with a discussion about the general applicability of photon counting to analytical spectrometry and the techniques which can be employed to further extend its field of application.

Before describing the various sources of noise encountered in photon counting, the following expressions are written to show how certain of the counting systems parameters cause the observed count rate to be less than the actual rate of photon arrival. It will be

assumed in all the derivations in this chapter, that count loss due to pulse pile-up is negligible.

The observed count rate N_{os}, resulting from a signal photon arrival rate of N_s is given by the expression:-

$$N_{os} = N_s \phi \eta A \qquad \ldots.5.1.$$

where A is the fraction of photon derived pulses, passed by the discriminator and the other symbols have their usual meanings (see chapter IV). The inclusion of the three system parameters ϕ, η and A alters the counting rate but has no effect on the time distribution of counts and does not therefore constitute a noise source. In general the required signal will be accompanied by unwanted background radiation of count rate N_b and a dark count of N_d. The observed count rates due to background (N_{ob}) and dark count (N_{od}) are given by:-

$$N_{ob} = N_b \phi \eta A$$

and $$N_{od} = N_d A'$$

A discriminator coefficient A' is written for the dark count, because the pulse amplitude distribution is different to that of the photon derived pulses, and therefore a different fraction of pulses will exceed the discriminator level. The total observed count rate N_{ot} is therefore given by:-

$$N_{ot} = N_{os} + N_{ob} + N_{od} \qquad \ldots.5.2.$$

Having established the basic efficiency of the counting process the source of noise can now be considered.

5.2. SOURCES OF NOISE IN PHOTON COUNTING.

5.2.1. Poisson Noise.

Poisson noise is a fundamental source of noise, associated with all random processes. The measured variance results from finite period

counting of events randomly distributed in time. Thus the variance in the count rate derived from a photon arrival rate of N_s is given by

$$\left(\sigma^2_{N_{os}}\right)_p = N_{os} = N_s \phi \eta A \qquad \ldots.5.3.$$

Similar expressions can be written for the background and dark count. The observed Poisson noise in the signal, background and dark count is in fact the result from a series combination of several Poisson processes e.g. random emission by the primary radiation source, random absorption and re-emission by the atom reservoir and random emission of photo electrons by the photo-cathode (note this does not imply that ϕ is noisy). In d.c. systems Poisson noise is usually referred to as 'Shot Noise' and is expressed in terms of the mean anode current i_a and the noise equivalent band-width Δf (see section 5.3) (101)

$$\left(\sigma^2_{d.c.}\right)_p = \sqrt{2eGi_a \Delta f}$$

5.2.2. Johnson Noise.

Electrons moving through a conductor continually exchange energy with the thermal vibrations of the lattice ions. As a result, random fluctuations in the charge density occur causing variations in the potential drop across the conductor. Johnson noise is therefore another fundamental source of noise and its variance is given by

$$\sigma^2_j = \frac{2k\Theta R}{t} \qquad \ldots.5.4.$$

where k is the Boltzmann constant

Θ is the absolute temperature

R is the resistance of the conductor

and t is the observation or integration period.

This equation shows that Johnson noise is most likely to occur in the load resistor R_L, where it may result in the generation of spurious

pulses. These pulses may either be counted directly (at very low discriminator levels), or can take part in producing pulse pile-up by either of the two pile-up mechanisms. Generally however, the variance term due to Johnson noise will be much less than terms due to Poisson and flicker noise, and will therefore be omitted from subsequent analyses.

5.2.3. Flicker Noise.

Having dealt with the two fundamental sources of noise, consideration will now be given to noise caused by non-ideal behaviour of the experimental system. This is generally known as flicker noise (111 - 117) and for convenience may be described under the following sub-headings.

(i) Signal and Background Radiation Flicker Noise.

Signal and background flicker in atomic spectrometry can result from power and temperature fluctuations in radiation sources, temperature fluctuations and gas turbulence in atom reservoirs, fluctuations in nebulisation rate and general external influences on the experimental system, such as vibration. The variance due to signal flicker may be written (111).

$$\left(\sigma^2_{N_{os}}\right)_f = \epsilon^2_s N^2_{os} = \left(N_s \epsilon_s A \phi \eta\right)^2 \qquad \ldots.5.5.$$

where ϵ_s is the dimensionless flicker factor for the signal (112) Likewise the variance due to background flicker is given by

$$\left(\sigma^2_{N_{ob}}\right)_f = \epsilon^2_b N^2_{ob} = \left(N_b \epsilon_b A \phi \eta\right)^2 \qquad \ldots.5.6.$$

In atomic spectrometry the flicker noise due to signal and background are independent, and therefore the associated variances can be added in quadrature to give the total flicker noise.

(ii) Flicker in the Counting System.

Flicker in the PMT gain, amplifier gain (if one is used), discriminator level and photo-cathode quantum efficiency etc., result in a broadening of the pulse height distribution. This does not in itself constitute noise, particularly when a low discriminator level is employed as was the case in chapter IV. (i.e. A and A' approach unity). However, as the discriminator level is raised the noise component due to variations in pulse amplitude increases, and reaches a peak when dN_0/dA i.e. the rate of change of observed count with discriminator level, is at a maximum. Even so, flicker noise from these sources is usually small compared with signal and background flicker and need not be considered further.

(iii) The Frequency Dependence of Flicker Noise.

Flicker noise is often found to be frequency dependent (111), exhibiting a 1/f power spectrum. Authors of papers on noise (111 - 117) in analytical spectrometry have noted this fact, but have usually ignored it in their derivations for the sake of simplicity. This may lead to error in the analysis for photon counting as the following argument shows. Equation 5.5 may be written:-

$$\left(\sigma^2_{N_{os}}\right)_f = \frac{F_s^2}{f^2} N_{os}^2 \qquad \ldots.5.7.$$

where the flicker factor ϵ_s has been split into a flicker constant F_s and the frequency f. Now the time required for one cycle of frequency f is t where

$$t = 1/f$$

Thus if t is equated to the integration period, it can be seen that the longer t, the lower the frequency component that will be able to contribute to the flicker noise. Unfortunately, no detailed frequency

spectra of flicker noise for various sources are available, and therefore it is not possible to say whether the spectrum has a low frequency cut-off. The frequency dependence of flicker noise will be further considered in the development of the total noise expressions.

5.2.4. Read-out Noise.

For the digital read-out there is always an uncertainty of ± 1 in the last figure, because the counting circuits are not synchronised with the photon derived pulses. This variance of one may be of importance at low count rates, but in general will be of no consequence in analytical spectrometry.

5.2.5. Total Noise in Photon Counting.

Each of the variance terms described in the previous sections were derived from independent variables and therefore add in quadrature to yield the total variance σ^2_{ot}. Thus for a typical analytical signal comprising a signal photon arrival rate N_s, a background photon arrival rate N_b and a dark pulse generation rate N_d, the total noise in the observed count rate is given by:-

$$\sigma^2_{ot} = \left(\sigma^2_{N_{os}}\right)_p + \left(\sigma^2_{N_{ob}}\right)_p + \left(\sigma^2_{N_{od}}\right)_p + \left(\sigma^2_{N_{os}}\right)_f + \left(\sigma^2_{N_{ob}}\right)_f$$

$$\text{i.e. } \sigma^2_{ot} = N_s\phi\eta A + N_b\phi\eta A + N_d A' + (N_s \epsilon_s A \phi\eta)^2 + (N_b \epsilon_b A \phi\eta)^2 \quad \ldots.5.9.$$

5.3. THE COMPARISON OF NOISE IN PHOTON COUNTING AND D.C. SYSTEMS.

The noise components associated with photon counting apply to d.c. systems, however a number of extra variance terms also apply. Noise in d.c. systems arises both from the time distribution of the signal photons and from the variation in amplitude of the individual photon

derived pulses. Noise in photon counting systems is mainly derived from the time distribution of the photons, and gives little weight to the amplitude variation of the individual pulses (especially at low discriminator levels). Thus in a counting experiment, any pulse having an amplitude above a certain level (all counting systems have a finite counting threshold) is counted and regardless of size a 1 is placed in the count register. This simple logic step accounts for the elimination of a number of noise components which apply to d.c. systems.

Secondary emission noise resulting from the statistical variation in pulse size, adds significantly to the d.c. noise particularly at low photo-electron fluxes. This can be described in terms of the variance in the overall gain of the tube which is usually given by (102):

$$\sigma_G^2 = \frac{G^2 (b\bar{\delta} + 1)}{(\bar{\delta} + 1)}$$

where b is the distribution shape factor (b = 0, Poisson distribution; b = 1 Exponential distribution). It can be shown that the variance in the d.c. current level resulting from secondary emission noise is (111);

$$\left(\sigma_{i_a}^2 \right)_{sec} = e i_c R_L^2 \sigma_G^2 / t$$

where i_c is the photo-cathodic current

and the other symbols have the same meanings as before.

Secondary emission noise also occurs in the dark count from the PMT, however the picture is more complex because the mean gain experienced by a particular pulse depends on the dynode of origin. This adds a further variance term which results in a considerable broadening of the pulse amplitude distribution particularly at the low amplitude end.

The work presented in the previous chapter demonstrated that photon counting could be achieved without the use of a pulse amplifier.

However, all modern d.c. spectrometric systems employ amplifiers, usually operational amplifiers of the current to voltage converter type. In this case the variance in the output voltage due to fluctuations in the amplifier gain can be expressed in the form:-

$$\sigma^2_{amp} = \left(R_f^2 (i_{rms})^2 + (v_{rms})^2 \right) \Delta f$$

where R_f is the value of the feedback resistor

i_{rms} and v_{rms} are the noise equivalent, rms input, current and voltages respectively, per unit band-width of the operational amplifier (these parameters are usually given by the manufacturer).

and Δf is the noise equivalent band-width.

It can be shown by use of the Fourier transform technique (102), that for the normal PMT - RC - amplifier combination, $\Delta f = 1/2t$ and that therefore lowering Δf is equivalent to increasing the integration period. However, amplifier noise often shows a 1/f dependence so that the apparent benefit of lowering Δf may be lost by the inclusion of extra low frequency noise components. In particular, some amplifiers exhibit strong 50 Hz noise components due to imperfect isolation from the mains frequency.

The gain variance introduced by the amplifier adds directly to the overall variance in d.c. measurement, whereas in photon counting its effect would be considerably reduced (if an amplifier is used). The same argument applies to all other sources of gain variance in the system e.g. PMT flicker, power supply flicker, etc. which broaden the pulse amplitude distribution but do not significanlty affect the time distribution of the signal.

The nature of read-out variance in photon counting has already been considered, and here again the counting technique exhibits superior performance to d.c. measurement. A number of read-out devices

may be employed in a d.c. system e.g. a meter, a chart recorder, or an oscilloscope and each of these has an associated variance which can be related to the signal magnitude and band-width of observation. Furthermore, a variance is introduced because of the resolution of the device, which relates to the ability of the operator to distinguish between two readings.

This section illustrates some of the ways in which the use of photon counting might be expected to improve the signal to noise ratio in the measurement of weak radiation signals. However, the improvement achieved depends largely on the nature of the limiting noise components in the system. Ingle and Crouch (111) have carried out a detailed analysis of the problem and conclude that under Poisson noise i.e. Shot noise limited conditions, photon counting should yield an improvement in the signal to noise ratio of between 5 and 22%. This is for the case where the integration period of the counting measurement is equivalent to the band-width of the d.c. system i.e. $t = 1/2\Delta f$. Generally shot noise limited conditions in analytical spectrometry are encountered when flicker contributions from the source and the atom reservoir are small. Such conditions are approached in low background AF systems e.g. non-flame AF and perhaps in low background AE systems. For flicker noise limited conditions e.g. AA, hot flame AF and AE and high concentration non-flame AF, Ingle and Crouch concluded that photon counting would not yield any measurable increase in the signal to noise ratio.

These results were obtained directly from the mathematical analysis, however practical considerations may somewhat alter the conclusions. For example, the freedom from drift exhibited by the photon counting systems described in the last chapter enables stable long period

integration which may yield signal to noise ratio improvements far in excess of those predicted on the basis of an equivalent integration period analysis. The ability to decrease the band-width in d.c. systems is invariably limited by the onset of system drift. This was encountered for quite short integration periods e.g. 1 second, with the amplifier/integrator described in chapter III, although the photon counting systems appeared to remain stable for several hours. The use of low discriminator levels contributes to drift stability since it can be expected that peak drift will occur when dN_o/dA is a maximum. Drift is difficult to analyse theoretically, because although it usually results from random variations in the temperature and supply voltage, the variations are often so slow that during a single integration period the drift is uni-directional.

Finally, it must be pointed out that photon counting is only applicable where the radiation intensity falls into the linear counting range. In certain systems, it may be that the maximum signal to noise ratio occurs when the radiation intensity is well in excess of this level. Where this is the case, reduction of the signal intensity for the purpose of bringing it into the linear range of a photon counter is unlikely to yield any increase in the precision of measurement.

5.4. SIGNAL TO NOISE RATIO EXPRESSIONS IN PHOTON COUNTING.

The analysis of photon counting measurement presented by Ingle and Crouch, was intended to show how the measured signal to noise ratio varied with input photon flux under a number of different noise limited conditions. However, the expressions derived related to integration periods compatible with the normal band-widths (e.g. 1 Hz $\equiv$ 0.5 seconds) employed in d.c. spectrometric systems. Photon counting can achieve stable integration over periods of several hours

if necessary, and therefore it is intended to derive expressions for the time related signal to noise ratio in order to ascertain what gains, if any, can be made by long period integration. Initially signals in AE and AF will be considered because the treatment is somewhat simpler than that for AA.

Before commencing the analysis it is worth considering which variance terms will be of importance and which can be ignored. This should enable simplification of the signal to noise ratio expressions and clarification of the time dependence. Reference to section 4.5.2 shows that even in low background systems i.e. non-flame AF, the background count rate is likely to be in excess of 10^3 c.p.s., e.g. in this case 4000 c.p.s. The minimum variance of this count rate is 4000 (for a Poisson signal) and therefore the variances due to dark count i.e. 3 (cooled tube) and read-out i.e. 1 can certainly be ignored. Furthermore, excess variance due to fluctuations in the counting system e.g. PMT flicker, gain flicker etc. are also likely to be extremely small in comparison, particularly when low discriminator levels are used. The variance terms of importance therefore, are those in the signal itself and only these will be considered in the analysis.

The noise expressions given in section 5.2 relate to the count rate i.e. the number of counts observed in one second, when the observation time is increased to t seconds the variance due to Poisson processes may be written generally

$$\left(\sigma^2_{N_o}(t)\right)_p = N_o t$$

and that due to flicker

$$\left(\sigma^2_{N_o}(t)\right)_f = \epsilon^2 N_o^2 t^2$$

These two terms represent the variances associated with Poisson and

flicker and the balance between them will determine the nature of the signal to noise ratio time dependence.

5.4.1. The Time-related Signal to Noise Ratio in Atomic Fluorescence and Atomic Emission Spectrometry.

Consider a steady state analytical signal derived from either an AE or AF system. Let the total photon flux N_t be composed of a signal flux N_s and a background flux N_b. Thus after a count period of t the following relation holds.

$$N_t t = N_s t + N_b t$$

Now the random fluctuations occurring in N_s and N_b do so independently and therefore the individual variances add in quadrature to yield the total variance. The total observed variance is therefore given by:-

$$\sigma^2_{N_{ot}}(t) = \sigma^2_{N_{os}}(t) + \sigma^2_{N_{ob}}(t) \qquad \ldots.5.10.$$

However, the variances in the signal and background are comprised individually of independent Poisson and Flicker components and thus

$$\sigma^2_{N_{os}}(t) = \left(\sigma^2_{N_{os}}(t)\right)_p + \left(\sigma^2_{N_{os}}(t)\right)_f$$

and $$\sigma^2_{N_{ob}}(t) = \left(\sigma^2_{N_{ob}}(t)\right)_p + \left(\sigma^2_{N_{ob}}(t)\right)_f$$

Remembering that a separate measurement of N_b has to be made in order to determine N_s, the total observed variance in the signal can be written

$$\sigma^2_{N_{ot}}(t) = \left(\sigma^2_{N_{os}}(t)\right)_p + \left(\sigma^2_{N_{os}}(t)\right)_f + 2\left(\sigma^2_{N_{ob}}(t)\right)_p + 2\left(\sigma^2_{N_{ob}}(t)\right)_f \quad \ldots.5.11.$$

The total signal is

$$N_{os} t \qquad \ldots.5.12.$$

Substituting into equations 5.11 and 5.12, the signal to noise ratio can be written in terms of the actual photon fluxes, i.e.

$$\frac{N_{os}t}{\sigma^2_{N_{ot}}(t)} = \frac{N_s t\phi\eta A}{(N_s t\phi\eta A + N_s^2 t^2 \epsilon_s^2 \phi^2 \eta^2 A^2 + 2N_b t\phi\eta A + 2N_b^2 t^2 \epsilon_b^2 \phi^2 \eta^2 A^2)^{\frac{1}{2}}} \quad \ldots.5.13.$$

Under shot noise limited conditions for example, a non-flame AF system employing a well stabilised source (possibly a continuum) the flicker factors tend to zero in which case equation 5.13 reduces to

$$\frac{N_{os}t}{\sigma^2_{N_{ot}}(t)} = \frac{N_s t^{\frac{1}{2}}(\phi\eta A)^{\frac{1}{2}}}{(N_s + 2N_b)^{\frac{1}{2}}} \quad \ldots.5.14.$$

This equation equation shows that the signal to noise ratio can be increased indefinitely in proportion to $t^{\frac{1}{2}}$ provided that drift can be avoided e.g. a 10 fold increase in the count period would yield an increase in the signal to noise ratio of $(10)^{\frac{1}{2}}$. Thus long period integration could be of considerable value in shot noise limited conditions, although the apparent gain is reduced because larger quantities of sample are required which normally might be subjected to preconcentration. Equation 5.14 also demonstrates the importance making ϕ , η and A as high as possible when seeking improved limits of detection.

When flicker noise dominates, for example in a hot flame AF or AE system, equation 5.13 reduces to

$$\frac{N_{os}t}{\sigma^2_{N_{ot}}(t)} = \frac{N_s}{(N_s^2 \epsilon_s^2 + 2N_b^2 \epsilon_b^2)^{\frac{1}{2}}} \quad \ldots.5.15.$$

Thus in this case the signal to noise ratio is independent of time and no benefit can be gained by long period integration. Indeed, if the flicker spectrum exhibits a 1/f dependence then extended period integration degrades the signal to noise ratio.

The frequency dependent flicker factor can be written (see section 5.2.3.)

$$\frac{F}{f} = Ft$$

Substituting into equation 5.15 for the time dependent flicker factor yields

$$\frac{N_{os}\,t}{\sigma^2_{N_{ot}}(t)} = \frac{N_s}{(N_s^2F_s^2 + 2N_b^2F_b^2)^{\frac{1}{2}}\,t} \qquad \ldots.5.16$$

Under these conditions the signal to noise ratio is improved by making t as short as possible, which effectively suppresses the low frequency flicker components. This can be achieved by synchronous photon counting (118), where the source or signal radiation is chopped and a two register counter, or counter with store facility employed to record successive short periods of signal and background. The equivalent method in the current measuring mode is the use of a.c. detection, which is commonly exployed in high flicker level systems e.g. hot flame AF.

The approximation of flicker domination is never fully met and the relative equations only serve as a guide to the situation. For example, it appears that the signal to noise ratio is independent of ϕ, η and A which clearly can never be the case. A general observation on all the signal to noise ratio expressions is that terms due to background variances always occur twice on the bottom line. The benefit of low background systems is thus clearly demonstrated and in photon counting where the linear counting range is limited, their use is invaluable.

Figure 36 shows log-log curves of the signal to noise ratio (N/σ) versus count period over the range 1.0 - 100.0 seconds, for a number of noise component conditions. The curves are based on observed count rates of $N_{os} = 10^4$ c.p.s. and $N_{ob} = 10^3$ c.p.s. and the conditions for each curve are as follows.

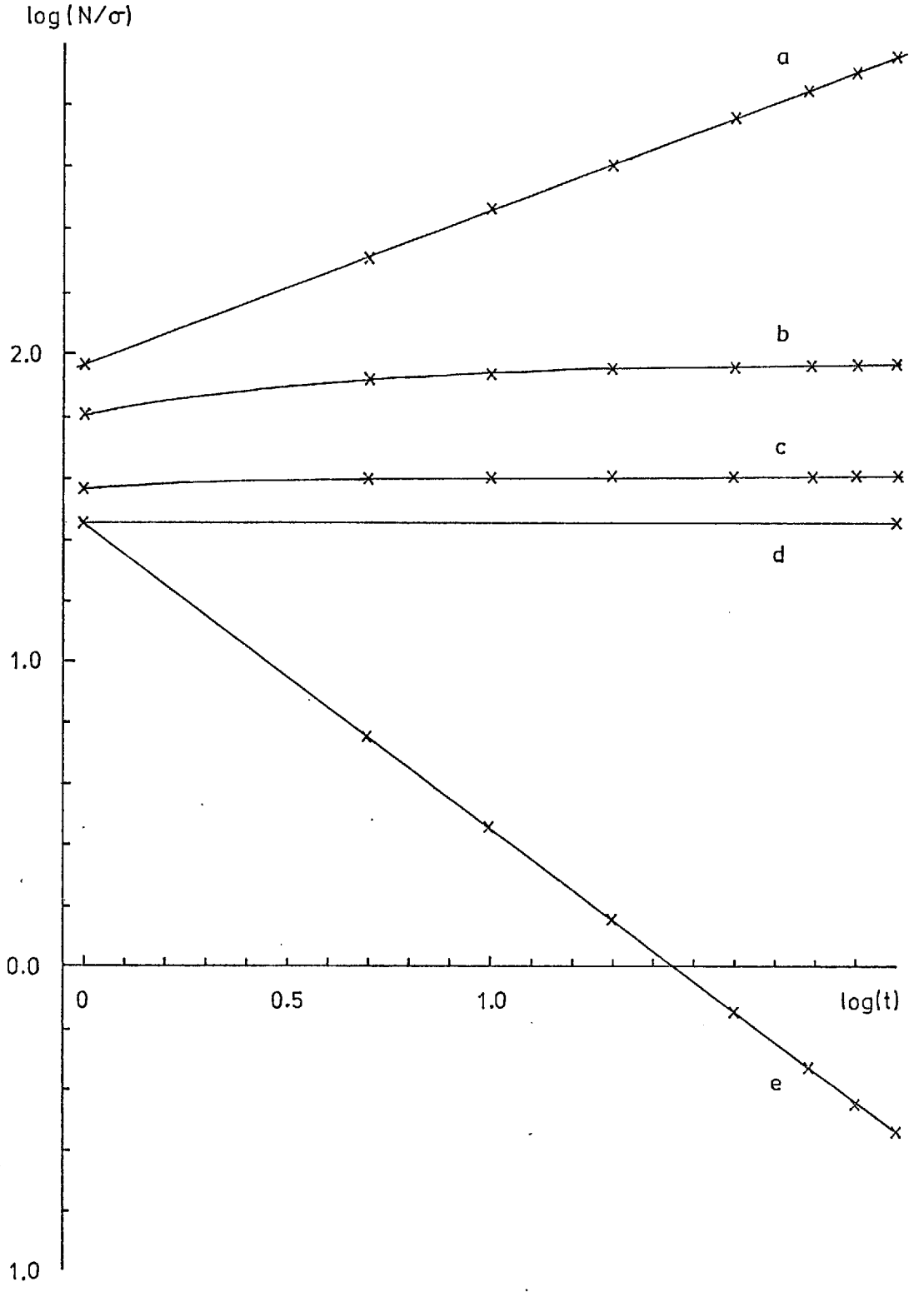


Fig.36. The effect of count period on signal to noise ratio.

Curve (a) Poisson noise limited case

$$\text{i.e.} \quad \epsilon_s^2 = 0 \; ; \; \epsilon_b^2 = 0$$

$$N/\sigma \propto t^{\frac{1}{2}}$$

therefore slope of the log-log curve $= \frac{1}{2}$

Curve (b) Poisson and flicker noise components of equal magnitude.

$$\text{i.e.} \quad \epsilon_s^2 = 10^{-4} \; ; \; \epsilon_b^2 = 10^{-3}$$

The signal to noise ratio is initially increased by a factor of about 0.5 but then rapidly approaches a horizontal asymptote.

Curve (c) Flicker noise components five times the magnitude of the Poisson components.

$$\text{i.e.} \quad \epsilon_s^2 = 5.10^{4} \; ; \; \epsilon_b^2 = 5.10^{-3}$$

The increase in signal to noise ratio is limited to 8% after which a horizontal asymptote is reached.

Curve (d) Flicker noise limited case i.e. flicker noise components ten times the Poisson components.

$$\text{i.e.} \quad \epsilon_s^2 = 10^{-3} \; ; \; \epsilon_b^2 = 10^{-1}$$

Signal to noise ratio independent of t, curve has constant ordinate value of 1.46.

Curve (e) Flicker noise limited case with 1/f flicker spectrum.

$$\text{i.e.} \quad \epsilon_s^2 = 10^{-3} \; ; \; \epsilon_b^2 = 10^{-1}$$

$$N/\sigma \propto 1/t$$

therefore slope of log-log curve = -1.

These curves show clearly the effect of long period integration for a number of noise component combinations. It can be seen that the larger the flicker components in the system the less that can be gained by integration. Indeed where the flicker exhibits a 1/f dependence, integration should be avoided because the signal to noise

ratio may be reduced below that required for the limit of detection i.e. 2. The curves are intended to illustrate general trends and cannot accurately predict the situation in all experiments because an infinite number of N_{os}, N_{ob}, ϵ_s^2 and ϵ_b^2 combinations are possible. Furthermore, other noise components may be present which are not taken into account in this treatment.

Consider the results of an experiment which was performed to test the effectiveness of long term integration in cool flame AF. The experimental apparatus was the same as that described in section 4.6.3, except that in this case the slit width was reduced to 0.01 mm in order to avoid overflow of the 6-digit register at the longer integration periods. A solution containing 5 p.p.m. Hg was nebulised continuously into the flame and 30 consecutive readings of signal and background count recorded at each count period. The standard deviation was then determined by application of equation 4.9 and the results compared with those predicted by equation 5.14 for Poisson noise limited conditions (see Table 11).

Table 11. The Effect of Increasing Count Period on Signal to Noise Ratio in a Cool Flame Atomic Fluorescence Experiment.

Count Period (sec)	Measured Signal to Noise Ratio	Signal to Noise Ratio from Poisson Statistics
1.0	17.84	15.00
10.0	23.73	48.72
100.0	23.97	144.7

The results for the one second count period appear to be Poisson noise limited but longer period integration reveals an increasing flicker contribution. The case of a white flicker frequency spectrum and a 1/f spectrum represent specific cases, and in practice each source will have a different frequency spectrum probably exhibiting some

characteristics of each type. For example, many radiation sources have 50 Hz (and higher harmonics) flicker components derived from the mains and in flames and nebulisers where the transport of fluids occurs, mechanical resonances may produce further intense narrow band components. It is difficult to account for this type of flicker in general noise expressions, because it is a function of the particular experimental system.

Further degradation of the signal to noise ratio can be caused by the occurrence of random interferences from external sources e.g. mains voltage spikes, RF sources, switching spikes etc. Many of these interferences may be Poisson distributed in time, however their time scale is no different to that of photon arrival that in terms of a single integration period they represent a unique event. Another difficulty associated with this type of noise is that each event results in a burst of counts which may or may not be significant in comparison with the signal count. The longer the integration period therefore, the more probable it is that random external interference will occur and once again this undermines the theoretical advantage of integration.

The results presented in this section lead to the conclusion that the value of integral measurement of continuous signals is dependent entirely on the nature of the signal. The variances which are most likely to limit the obtainable signal to noise ratio are those arising directly from system instability and therefore particular attention should be given to this aspect of instrument design. Equations can be developed which relate signal to noise ratio to measurable system parameters; however in general knowledge of the system is insufficient for the equations to yield reliable results. The calculation of signal

to noise ratio or precision (precision = 100 times the reciprocal signal to noise ratio) of photon counting results from AE and AF must therefore be accomplished by repetitive measurements on standard samples.

5.4.2. The Signal to Noise Ratio in Atomic Absorption Spectrometry.

Atomic absorption spectrometry usually involves the measurement of a ratio, rather than a diffenence as is the case in AE and AF. The equation for the time related signal to noise ratio is therefore more complex, although it can be calculated in the same manner as before. Rather than derive more theoretical calculations of an approximate nature, it was decided to investigate experimentally the signal to noise ratio and its relation to the count period for a specific case.

The experimental system employed was the same as that described in section 4.6.4. Solutions containing 1.0 p.p.m. Cd were nebulised continuously into the flame to enable repetitive readings of reference and transmitted beam count. The slit width as before was 0.03 mm which yielded a reference beam count of 896317 c.p. 10s. Although the source was 50 Hz modulated, it was extremely stable in terms of a 10 second count period, having a relative standard deviation of 0.32% (see section 4.6.4.). Thus in this case the source had a low magnitude flicker spectrum with one strong narrow band at 50 Hz.

The investigation of signal to noise ratio in relation to the count period was carried out on the absorbed intensity rather than the absorption, which simplified the calculations. Repetitive readings were taken for count periods of 0.1, 1.0 and 10.0 seconds respectively and the results obtained are shown in Table 12.

Table 12. The Effect of Increasing Count Period on Signal to Noise Ratio in a Cool Flame Atomic Absorption Experiment.

Count Period (seconds)	0.1	1.0	10.0
Signal to Noise Ratio	4.21	21.99	22.43

The table shows that the presence of the 50 Hz flicker component seriously degraded the signal to noise ratio at the 0.1 second count period. This occurred because the integration period was not synchronised with the flicker component and included only 5 cycles of amplitude variation. Once the integration period reached 50 times the modulation period, the effect of the 50 Hz component was completely nullified. Further increase in the count period yielded little increase in the signal to noise ratio, indicating a fairly flat or white flicker frequency spectrum. These results are interesting because they show that where narrow band flicker components are present, integration can yield significantly improved signal to noise ratio.

Many analysts when using AA convert absorption readings into absorbance A and often commercial AA spectrometers employ logarithmic amplifiers which perform this function automatically. Calculation of the signal to noise ratio or precision in absorbance can be achieved in two ways, either by repetitive recording of absorbance values or by application of the equation (106):-

$$\% \frac{\sigma}{A} = \frac{\log (1/\alpha + \sigma_{1/\alpha}) - \log (1/\alpha)}{\log(1/\alpha)} \times 100 \quad \ldots.5.17.$$

$\sigma_{1/\alpha}$ can in turn be calculated by application of equation 4.8. In order to test the applicability of equation 5.17 to photon counting results the error in absorbance was determined experimentally by both methods. For comparison purposes, precision measurements were made on

the absorbed intensity N_a and furthermore all results were calculated theoretically on the basis of Poisson noise limited conditions. The results are tabulated in Table 13.

Table 13. Comparison of Percentage Relative Standard Deviations

	Relative Standard Deviation (%) of N_a		Relative Standard Deviation (%) of absorbance value	
Count period (seconds)	1.0	0.1	1.0	0.1
Poisson Statistics	4.91	14.21	3.95	13.97
Experimental values	4.55	23.77	4.74	19.92
From Equations 4.8 and 5.17 and the Experimental Values of σ_{N_o} and σ_N	-	-	6.53	18.60

The agreement between the experimental values is quite good particularly in view of the fact that only 30 readings were taken in order to calculate the standard deviations. Once again the 50 Hz flicker component caused a serious degradation in the signal to noise ratio for the 0.1 second count period. This effect of course is not predicted by Poisson statistics and therefore the calculated values were better than those obtained experimentally.

Generally the precision obtained for the measurement of A (or α) was slightly better then that obtained for N_a. Calculation of N_a involves measurement of a difference i.e. $N_o - N$, whereas calculation of A involves measurement of a ratio i.e. N_o/N and therefore better precision can be expected in the A value, because the ratio is less sensitive to changes in N_o than the difference. Finally, equation 5.17 exhibits a shallow minimum at about 1.0 absorbance units and therefore,

where possible, measurements should be made in this region in order to obtain maximum precision.

5.4.3. The Signal to Noise Ratio For Transient Signals.

The work in chapter IV demonstrated the ability of photon counting to make precise measurements on transient signals of variable profile. Measurement is based on the principle that any transient signal whose profile encloses the same area will yield the same integrated count, provided that the count period extends over the entire duration of the signal. Thus for a transient signal $N(t)$ where $N(t) = 0$ for $0 < t < \tau$, the process can be represented by

$$\int_0^{\tau} N(t).dt = N_{os}$$

where N_{os} is the total observed count.

In nearly all cases $N(t)$ is unknown and furthermore may vary with concentration or sample matrix. Calculation of the precision or signal to noise ratio in N_o must therefore be carried out experimentally by repetitive readings, and cannot be predicted by simple equations.

The integration period employed is most important because inclusion of unwanted background can seriously reduce the signal to noise ratio. Consider some results obtained with the first photon counter, which had a Poisson distributed dark count of 469 c.p.s. A camera shutter was used to produce timed light flashes from a tungsten bulb (run from a stabilised d.c. supply) focussed onto the entrance slit of the Unicam SP900. Two shutter speeds of 8.0 and 40.0 m.sec. (longer shutter speeds tended to become non-reproducible) were employed and their accuracy checked with a storage oscilloscope. Thirty readings of the light flash intensity were then recorded for each shutter speed, by both photon counting and the d.c. amplifier/integrator system (see section 3.2.1). The only background count occurring in this

experiment therefore, was that due to dark count. The results obtained are summarised in Table 14.

Table 14. Integration of Transient Radiation Signals

Shutter Speed (m.sec)		Photon Counting			D.c. Amplifier/Integrator		
		Average Count (sec-1)	Standard Deviation	Relative Standard Deviation (%)	Average Signal	Standard Deviation	Relative Standard Deviation (%)
8.0	0.5	125.9	34.45	27.9	4.37	1.23	28.1
40.0	2.0	10781	225.1	2.09	40.31	0.94	2.33

It can be seen that in each case photon counting yielded an improved precision, in spite of the fact that integration was taken over several times the signal duration (the d.c. system integrates over the signal duration only). The improvement in precision achieved by photon counting was 0.7% for the 8 m sec. signal and 10.54% for the 40 m sec. signal, which is indicative that correct count period timing is essential for transient signals. Indeed in this case the unwanted variance due to excess background can be calculated, and when this is done for the 8 m sec. signal and subtracted from the total variance, it is found that the precision should increase to 21.3%.

Unfortunately precise timing is often difficult, because of uncertainty in the start and finish points of the profile. However, a device producing a variable count period which could be triggered by the start of the event would enable approximate synchronisation of the count period with resulting increases in precision. In high background systems particularly where the background is noisy, the provision of count period synchronisation is essential in order to avoid complete degradation of the signal to noise ratio by flicker components.

5.5. CONCLUSIONS.

Photon counting ultimately must be the most sensitive method of measuring light intensity because the measurement is made in units of the minimum known quantity of radiant energy i.e. the photon. The limitations of the technique are imposed purely by the current state of technology, as illustrated by the limited linear counting range. At present the linear range extends to about 10^6 c.p.s., but ultimately counting up to 10^8 c.p.s. will be required before the technique has the same useful range as current measuring devices. The practical and theoretical aspects of photon counting in analytical spectrometry have been investigated in the the previous two chapters, and therefore rather than repeat the conclusions drawn it is intended to discuss ways in which some of the limitations can be overcome and the field of application widened.

One method of extending the linear counting range by use of the lower discriminator level has already been described. Further improvement can be achieved by application of an upper discriminator level and some simple logic circuits (119). Pile-up pulses are nearly always larger than single photon pulses and therefore provision can be made for placing a 2 in the register, every time a pulse exceeding the upper threshold occurs. This undoubtedly improves the linear counting range but care is required at low photon fluxes, because noise introduced by the radioactive pulses etc. is effectively doubled.

Addition of a small on-line, dedicated computer to the photon counter would certainly give the instrument greater versatility. For example, the main conclusion of the previous chapters was that photon counting is best suited to the measurement of low radiation levels, and that the value of the inherent integration which counting yields

is entirely dependent on the time distribution of the signal to be measured. Automatic control of the photon counter to yield consecutive short period observations which could be stored, would enable a frequency spectrum of the analytical signal to be constructed. The principle harmonic noise components (if any) could be identified and filtering achieved by appropriate selection of the count period. The technique would be equivalent to the Fourier transform methods commonly employed in NMR and IR spectrometry. Other operations that could be simply carried out include time averaging of results, calculation of the standard deviation, rejection of spurious results, background count correction and possibly pulse pile-up correction. The ever decreasing cost of small laboratory computers will undoubtedly make them a common feature of future photon counting systems.

Many modern spectrometric systems employ double beam instrumentation which enables minimisation of errors due to drift. Photon counting can be applied to double beam instrumentation with great precision because the reference beam can be monitored for the total radiation emitted. The technique employed (107) is to preset the reference beam register, so that the signal or ratio is read out after a given number of counts has been amassed. Drift compensation is therefore achieved by automatic adjustment of the count period. In conclusion, the initial results obtained with photon counting are sufficiently promising to suggest that the technique will be increasingly employed in analytical spectrometry.

The results presented in this thesis relate to two new techniques which are receiving increasing attention in the field of analytical spectrometry. It is hoped that these studies will contribute in their assessment and encourage further investigation.

oooOOOooo

APPENDIX I

Program to simulate a photon counting experiment

Data Name List

NS - number of simulations

B - average time between photons

DEAD - system dead time

TLIM - count period

Program.

```
      DIMENSION KOUNT ( 252 )
      COMMON B, A, SECS
      READ ( 5, 1000 ) NS
 1000 FORMAT ( I3 )
      DO 11 J = 1,NS
      DO 10 I = 1,250
 10   KOUNT ( I ) = 0
      CLOCK = 0.0
      N = 0
      KOV = 0
      KSUM = 0
      READ ( 5,1001 ) B, DEAD, TLIM
 1001 FORMAT ( 10X, 3( 4X, E8.2 ) )
      RDEAD = 0.0
      GO TO 105
 104  RDEAD = DEAD
 105  ND = 0
 102  CALL TIME
      CLOCK = CLOCK + SECS
      IF ( CLOCK.GT.TLIM ) GO TO 100
      IF ( SECS.GT.RDEAD ) GO TO 101
      ND = ND + 1
      GO TO 102
 101  N = N + 1
      IF ( ND.GE.250 ) GO TO 103
      KOUNT (ND + 1) = KOUNT (ND + 1) + 1
      GO TO 104
 103  KOV = KOV + 1
```

```
      KSUM = KSUM + ND
      GO TO 104
100   KSUM = KSUM + N
      DO 15 I = 1,250
15    KSUM = KSUM + KOUNT (I)*(I-1)
      SUM = KSUM
      TOT = N
      EFIC = (TOT/SUM)*100.0
      WRITE (6,1300) B,DEAD,TLIM,KSUM,N,KOV
1300  FORMAT (1X,10X, 3(4X,E8.2),10X,I10,I0X,I10,10X,I4
      WRITE (6,1900) EFIC
1900  FORMAT (4X,F7.2)
      I = 0
      WRITE (6,1100) I, KOUNT(1)
1100  FORMAT ( 1X,I4,1X,I7 )
      DO 12 I = 1,241,10
      IJK = I + 9
      WRITE (6,1200) (K,KOUNT(K + 1), K = I,IJK)
1200  FORMAT (1X, 10(I4,1X,I7,1X) )
12    CONTINUE
11    CONTINUE
      STOP
      END
      SUBROUTINE TIME
      COMMON B,A,SECS
      RANGE = 0.0
109   R = RNIST (RANGE)
      IF  (R.EQ.0.0) GO TO 109
      SECS = -ALOG(R)*B
      RETURN
      END
```

APPENDIX II

Program to solve a Convolution Integral - CONVOLU.

Data Name List.

NK - number of segments in the RESPO(K) array.

JK - number of segments in the EXCIT(I) array.

R - value of the load resistance R_L.

C - value of the stray capacitance C_s.

SIG - standard deviation of the PMT transit time spread.

DT - the segment width t.

Q - the total mean charge in a single photo-electron pulse (=Ge).

IFLAG - stop index.

Program.

```
      PROGRAM CONVOLU(INPUT,OUTPUT,TAPE5=INPUT,TAPE6=OUTPUT)
      DIMENSION RESPO(1500),EXCIT(400),CONVO(1500),CURVE(1500)
 80   READ(5,1000) NK,JK
 1000 FORMAT (I4,4X,I4)
      READ (5,1001) R,C,SIG,DT,Q
 1001 FORMAT ( 5(F8.3,2X) )
      READ (5,1002) IFLAG
 1002 FORMAT (I1)
C CALCULATION OF INPUT ARRAY
      PI = 6.284
      CON = 0.0
      TOW = 0.0
      FAC = SQRT(PI)
      CON = Q / (SIG * FAC)
      SIG2 = SIG ** 2.0
      T = 0.0
      JOT = ( (JK - 1) / 2 ) + 1
      EXCIT(JOT) = CON
      KOT = JOT + 1
      DO 100 I = KOT,JK
      T = T + DT
      TOW = (T**2.0) / (2.0*SIG2)
      EXCIT (I) = CON * ( 1.0 / EXP(TOW) )
 100  CONTINUE
      LOT = JOT - 1
```

```
      MOT = JK + 1
      DO 120 I = 1,LOT
      MOT = MOT - 1
      EXCIT(I) = EXCIT(MOT)
  120 CONTINUE
C CALCULATION OF RESPONSE FUNCTION
      POW = 0.0
      T = 0.0
      RESPO(1) = 1.0/C
      DO 101 K = 2,NK
      T = T + DT
      POW = T/(B*C)
      RESPO(K) = (1.0/C) * ( 1.0/EXP(POW) )
  101 CONTINUE
C CONVOLUTION OF ARRAYS
      DO 111 JIK = 1,1500
      CONVO (JIK) = 0.0
  111 CONTINUE
      IF (NK.GE.JK) GO TO 20
      JOK = NK
      KOK = JK
      GO TO 30
   20 JOK = JK
      KOK = NK
   30 DO 102 N = 1,JOK
      K = 0
      I = N + 1
      DO 103 KK = 1,N
      K = K + 1
      I = I - 1
      CURVE(KK) = RESPO(K) * EXCIT(I)
  103 CONTINUE
      DO 104 KDUM = 1,N
      CONVO(N) = CONVO(N) + DT * (CURVE(KDUM) )
  104 CONTINUE
  102 CONTINUE
      NJ = KOK - JOK
      DO 105 M = 1,NJ
```

```
      I = JOK + 1
      K = M
      DO 106 KK = 1,JOK
      K = K + 1
      I = I - 1
      IF (NK.GE.JK) GO TO 40
      KIK = I
      IKI = K
      GO TO 50
40    KIK = K
      IKI = I
50    CURVE(KK) = RESPO(KIK) * EXCIT(IKI)
106   CONTINUE
      J = N + M
      DO 107 KNUM = 1,JOK
      CONVO(J) = CONVO(J) + DT * ( CURVE(KNUM) )
107   CONTINUE
105   CONTINUE
      JAK = JOK - 1
      DO 108 L = 1,JAK
      I = JOK + 1
      K = KOK - JOK + L
      KAK = JOK - L
      DO 109 KK = 1,KAK
      K = K + 1
      I = I - 1
      IF (NK.GE.JK) GO TO 60
      KIK = I
      IKI = K
      GO TO 70
60    KIK = K
      IKI = I
70    CURVE(KK) = RESPO(KJK) * EXCIT(IKI)
109   CONTINUE
      J = J + 1
      DO 110 KGUM = 1,KAK
      CONVO(J) = CONVO(J) + DT * ( CURVE(KGUM) )
110   CONTINUE
```

```
 108  CONTINUE
C OUTPUT ROUTINE
C RESULTS OF THE CONVOLUTION
      WRITE (6,1010) (EXCIT(I),I = 1,JK)
 1010 FORMAT ( 1X,5(10H EXCIT(I) ,2X,F8.4) )
C OUTPUT OF RESPONSE ARRAY
      WRITE (6,1020) (RESPO(K),K = 1,NK)
 1020 FORMAT (1X,5(10H RESPO(K) ,2X,F8.4) )
C OUTPUT OF CONVOLUTED ARRAY
      WRITE (6,1030) (CONVO(J0), J0 = 1,J)
 1030 FORMAT (1X,5(10H CONVO(J) ,2X,F8.4) )
      IF (IFLAG.NE.1) GO TO 80
      STOP
      END
```

REFERENCES.

1. G. Kirchhoff, Pogg. Ann., 109, 275 (1860).
2. G. Kirchhoff and R. Bunsen, Pogg. Ann., 110, 161 (1860).
3. H. Lundegardh, 'Die quantitative Spektralanalyse der Elemente', Fischer, Jena; Part 1 (1929); Part 2 (1934).
4. A.C.G. Mitchell and M.W. Zemansky, Resonance Radiation and Excited Atoms, University Press, Cambridge (1961).
5. A. Walsh, Australian Patent No. 23041/53 (1953); Spectrochim. Acta., 7, 108 (1955).
6. C.Th.J. Alkemade and J.M.W. Milatz, J. Opt. Soc. Am., 45, 583 (1955).
7. R.W. Wood, Phil. Mag., 10, 513 (1905).
8. E.L. Nichols and H.L. Howes, Phys. Rev., 22, 425 (1923).
9. R.M. Badger, Z. f. Phys., 55, 56 (1929).
10. R. Mankopff, Verhandl. d. Deutsch Phys. Ges., 14, 16 (1933).
11. J.D. Winefordner and T.J. Vickers, Anal. Chem., 36, 161 (1964).
12. J.D. Winefordner and R.A. Staab, Anal. Chem., 36, 161 (1964).
13. J.D. Winefordner, J.M. Mansfield and C. Veillon, Anal. Chem., 37, 1049 (1965).
14. J.D. Winefordner and R.A. Staab, Anal. Chem., 36, 165 (1964).
15. K.E. Zacha, M.P. Bratzel, J.D. Winefordner and J.M. Mansfield, Anal. Chem., 40, 1733 (1968).
16. T.S. West, Analyst, 91, 69 (1966).
17. R.M. Dagnall, T.S. West and P. Young, Talanta, 13, 803 (1966).
18. R.M. Dagnall, K.C. Thompson and T.S. West, Talanta, 14, 557 (1967).
19. R.M. Dagnall, K.C. Thompson and T.S. West, Talanta, 14, 1151 (1967).
20. R.M. Dagnall, K.C. Thompson and T.S. West, Talanta, 14, 1467 (1967).
21. R.M. Dagnall, K.C. Thompson and T.S. West, Talanta, 15, 667 (1968).
22. R.M. Dagnall, K.C. Thompson and T.S. West, Anal. Chim. Acta, 40 (1968).
23. B. L'Vov, Atomic Absorption Spectrochemical Analysis, Adam Hilger, London (1970).

24. G.A. Morton, Appl. Opt., 7, 1 (1968).

25. E.H. Piepmeier, D.E. Braun and R.R. Rhodes, Anal. Chem., 40, 1667 (1968).

26. J.B. Willis, Nature, 207, 715 (1965).

27. M.D. Amos and J.B. Willis, Spectrochim. Acta., 22, 1325, 2128 (1966).

28. J.E. Chester, R.M. Dagnall and M.R.G. Taylor, Anal. Chim. Acta., 51, 95 (1970).

29. G.F. Kirkbright, A. Semb and T.S. West, Talanta, 14, 1011 (1967).

30. D.N. Hingle, G.F. Kirkbright and T.S. West, Talanta, 15, 199 (1968).

31. G.F. Kirkbright, A. Semb and T.S. West, Talanta, 15, 441 (1968).

32. H. Maecker, Z. Physik, 141, 198 (1955).

33. H.N. Olsen, Phys. Fluids, 2, 614 (1959).

34. G. Rossi and N. Omenetto, Talanta, 16, 265 (1969).

35. W. Hittorf, Wiedermann's Annalen XXI, 138 (1884).

36. A.J. McCormack, S.C. Tang and W.D. Cooke, Anal. Chem., 37, 1470 (1965).

37. J.J. Thompson, Phil. Mag., 32, 321 (1891).

38. D.A. Jackson, Proc. Roy. Soc., A121, 432 (1928).

39. W.F. Meggers, J. Opt. Soc. Am., 38, 7 (1948).

40. W.F. Meggers and F.O. Westfall, J. Res. Nat. Bur. Std., 44, 447 (1950).

41. W.F. Meggers and K.G. Kessler, J. Opt. Soc. Am., 40, 737 (1950).

42. E. Jackobson and G.R. Harrison, J. Opt. Soc. Am., 39, 1054 (1949).

43. A.T. Forrester, R.A. Gudurumdsen and P.O. Johnson, J. Opt. Soc. Am., 46, 339 (1956).

44. F.C. Fehsenfeld, K.M. Evenson and H.P. Broida, Rev. Sci. Inst., 36, 294 (1965).

45. M.D. Silvester and W.J. McCarthy, Spectrochim. Acta., 25B, 229 (1970).

46. R.M. Dagnall, R. Pribil jnr. and T.S. West, Analyst, 93, 281 (1968).

47. R.F. Browner, R.M. Dagnall and T.S. West, Anal. Chem. Acta., 45, 163 (1969).

48. K.M. Aldous, Thesis, University of London (1970).

49. J.H. Runnels and J.H. Gibson, Anal. Chem., 39, 1398 (1967).

50. R. Mavrodineanu and H. Boiteaux, Flame Spectroscopy, Wiley N.Y. (1965).

51. H.R. Griem, Plasma Spectroscopy, McGraw Hill Inc., 129 (1964).

52. R. Smith, P.J.T. Zeegers and J.D. Winefordner, Anal. Chem., 40, 13, 26A (1968).

53. H. Massmann, Spectrochim. Acta., 23B, 215 (1968).

54. B.V. L'Vov, Spectrochim. Acta., 17B, 761 (1961).

55. J.F. Alder and T.S. West, Anal. Chim. Acta., 51, 363 (1970).

56. M.P. Bratzel jnr., R.M. Dagnall and J.D. Winefordner, Anal. Chim. Acta., 48, 197 (1969).

57. M. Marinkovic and T.J. Vickers, Appl. Spectrosc., 25, 319 (1971).

58. J. Mansfield, Private communication (Imperial College) (1972).

59. J.M. Mansfield, H.L. Parsons, C. Veillon and J.D. Winefordner, Anal. Chem., 38, 204 (1966).

60. J.M. Mansfield, M.P. Bratzel jnr., H.O. Norgordon, D.O. Knapp, K.E. Zacha and J.D. Winefordner, Spectrochim. Acta., 23B, 389 (1968).

61. W. Voigt, Munch. Ber., 603 (1912).

62. H.P. Hooymayers, Spectrochim. Acta., 23B, 567 (1968).

63. C.Th.J. Alkemade, Proc. Xth Colloquium Spectroscopium Internationale, Spartan Books, Washington D.C. (1963).

64. G.F. Kirkbright, M. Sargent and S. Vetter, Spectrochim. Acta., 25B, 465 (1970).

65. G.V. Marr, Plasma Spectroscopy, Elselvier (1968).

66. H. Harmann, Z. Physik., 97, 539 (1935).

67. C.H. Corliss and J.B. Schumaker, N.B.S. J. Res., 71A, 575 (1967).

68. D.R. Inglis and E. Teller, Astrophys. J., 90, 439 (1939).

69. H. N. Olsen, Phys. Rev., 124, 6 (1961).

70. P.D. Johnston, Thesis, University of London (1969).

71. B.D. Adcock and W.E.G. Plumtree, J. Quant. Spectrosc. Rad. Transfer, 4, 29 (1964).

72. J.A. Hornbeck and J.P. Molnar, Phys. Rev., 84, 621 (1951).

73. E.O. Johnson and L. Malter, Phys. Rev., 76, 1411 (1949).

74. E.O. Johnson and L. Malter, Phys. Rev., 80, 58 (1950).

75. Y.M. Kagan, K.S. Mustafin, V.I. Popel and V.M. Zakharova, Zh. Tekh. Fiz., 30, 442 (1960).

76. L.E. Brewer and W.K. McGregor, Phys. Fluids, 5, 1485 (1962).

77. K. Fallgatter, V. Svobada and J.D. Winefordner, Appl. Spectrosc., 25, 347 (1971).

78. K.W. Busch and T.J. Vickers, Submitted to Anal. Chem.

79. H. Schlueter, Z. Naturforsch., 18a, 439 (1963).

80. H. Drawin, Ann. Physik, 17, 374 (1966).

81. A.D. MacDonald, Microwave Breakdown in Gases, John Wiley, N.Y. (1966).

82. C. Kenty, Phys. Rev., 32, 624 (1928).

83. W.P. Jesse and J. Sadauskis, Phys. Rev., 100, 1755 (1955).

84. M. Biondi, Phys. Rev., 82, 453 (1951).

85. S. Greenfield, I.L. Jones and C.T. Berry, Analyst, 89, 713 (1964).

86. R.M. Dagnall, D.J. Smith, T.S. West and S. Greenfield, Anal. Chim. Acta., 54, 397 (1971).

87. C.A. Bache and D.J. Lisk, Anal. Chem., 37, 1477 (1965).

88. Ibid, 38, 783 (1966).

89. Ibid, 39, 786 (1967).

90. M.P. Bratzel Jnr., R.M. Dagnall and J.D. Winefordner, Anal. Chim. Acta., 48, 197 (1969).

91. D. Clark, Private communication, Imperial College (1971).

92. D. Johnson, Private communication, Imperial College (1971).

93. Dept. of Geochemistry, Private communication, Imperial College (1970).

94. Dept. of Metallurgy, Private communication, Imperial College (1971).

95. W.J. Kirsten and G.O.B. Bertilson, Anal. Chem., 38, 648 (1966).

96. N.R. Lindblad and J.M. Schneider, J. Sci. Instrum., 42, 635 (1965).

97. P.Penfield Jnr. and D.E. Sawyer, Proc. IEEE, 53, 340 (1965).

98. M.E. Hines, IEEE Trans. ED-13, 158 (1966).

99. R.J. McIntyre, IEEE Trans. ED-13, 164 (1966).

100. J.I. Morrow, International Laboratory, Nov/Dec (1971).

101. EMI Photomultiplier Tube Catalogue.

102. RCA Photomultiplier Tube Manual.

103. A.D. Lewis and F.H. Wells, Millimicrosecond Pulse Techniques, Pergamon, London (1959).

104. G.A. Morton, Appl. Optics, 7, 1 (1968).

105. E.H. Piepmeier, D.E. Braun and R.R. Rhodes, Anal. Chem., 40, 1667 (1968).

106. M.L. Franklin, G. Horlick and H.V. Malmstadt, Anal. Chem., 41, 2 (1969).

107. K.C. Ash and E.H. Piepmeier, Anal. Chem., 43, 26 (1971).

108. Ortec Ltd., Application Note, AN35 (1971).

109. S. Seymour and J.J. Jones, Modern Communication Principles, McGraw-Hill (1967).

110. M.R. Gavin and J.E. Houldin, Principles of Electronics, The English Universities Press (1959).

111. S.R. Crouch and J.D. Ingle, Anal. Chem., submitted for publication.

112. J.J. Cetorelli, W.J. McCarthy and J.D. Winefordner, J. Chem. Ed., 45, 98 (1968).

113. W.J. McCarthy and J.D. Winefordner, J. Chem. Ed., 44, 136 (1967).

114. W.J. McCarthy, M.L. Parsons and J.D. Winefordner, J. Chem. Ed., 44, 214 (1967).

115. L.J. Cline, V. Svoboda and J.D. Winefordner, Crit. Rev. Anal. Chem., Aug (1970).

116. J.J. Cetorelli and J.D. Winefordner, Talanta, 14, 705 (1967).

117. P.A. St.John, W.J. McCarthy and J.D. Winefordner, Anal. Chem., 38, 1828 (1966).

118. F.T. Arecchi, E. Gatti and A. Sona, Rev. Sci. Instr., 37, 942 (1966).

119. Elscint, Nuclear Instruments Catalogue (1972).